UNIVERSITY OF SÃO PAULO
POLYTECHNICAL SCHOOL

Marcelo Rubens Galdiano Duarte

UN crash safe vehicle design using human body models

São Paulo

2021

Marcelo Rubens Galdiano Duarte

UN crash safe vehicle design using human body models

Revised version

Dissertation presented to the Polytechnical School, University of São Paulo to obtain the the title of Master of Science - Post Graduate Program of Mechanical Engineering.

Concentration Area: Project and Manufacturing

Advisor: Prof. Dr. Marcilio Alves

São Paulo
2021

This copy has been revised and changed in relation to the original version under the sole responsibility of the author and with the consent of his advisor.

São Paulo, July 15, 2021.

Author: Marcelo Duarte

Advisor:

Duarte, Marcelo Rubens Galdiano
UN crash safe vehicle design using human body models / M. R. G. Duarte – revised version – São Paulo, 2021.
127 p.

Dissertation (Master's Degree) – Polytechnical School of the University of São Paulo. Mechanical Engineering Post Graduate Program.

1.Pedestrian safety 2.Crashworthiness 3.Electric vehicle 4.Numerical models 5.Human body model I.University of São Paulo. Polytechnical School. Mechanical Engineering Post Graduate Program.

To my parents, Newton and Carmen.

ACKNOWLEDGEMENTS

To Professor Marcilio for providing so many practical advices during the elaboration of this dissertation and for all the productive discussions we have had during the past years. Thank you Professor.

To Professors Fabian Duddeck (Technical University of Munich) and Rogerio Marczak (Federal University of Rio Grande do Sul) for watching my presentation and for all the constructive comments made about my Master Thesis.

To CAPES for the financial support.

To GHBMC for providing the human body model to be used in the pedestrian simulations.

To GMSIE group researchers, in special to Diego Dias de Lima Santos and Decio de Moura Rinaldi, for the long chats we had about which software I could use to develop the dissertation and for all the tips provided on how to construct the suspension system.

To my parents Newton and Carmen, my brother Murilo and my sister Marília. Your support was really important and knowing that I could count on you made this work much easier.

To my wife Fernanda. Your support was fundamental. Your affection in the sad moments and your smile in the happy ones motivated me to continue this journey and to accomplish this task.

“Nothing is too wonderful to be true,
if it be consistent with the laws of nature.”
Michael Faraday

ABSTRACT

DUARTE, M. R. G. **UN crash safe vehicle design using human body models**. 2021. 126f. Dissertation (Masters Degree) - Polytechnical School, University of São Paulo, São Paulo, 2021.

This dissertation presents the design of a Safe Urban Vehicle capable of meeting the vehicle safety requirements established by the United Nations Economic Commission for Europe, UNECE. The electric vehicle was developed to be used on urban environments, having two seats and space for shopping and small luggage transportation. The design evaluation was performed through the explicit Finite Element Method. First it was analyzed the frontal impact crash test, based on ECE R94, where the model crashes a deformable barrier with 40% width offset. This simulation was realized using the traditional models of Anthropomorphic Test Devices (ATD), usually called “dummies”. It was analyzed the model’s body and head responses and the results were compared to the values required by the regulation. After that it was analyzed the car to pedestrian crash test based on regulation ECE R127. In this analysis the usual dummies were replaced by complex anthropomorphic devices based on human body containing tendons, bones and organs. Model’s obtained results were analyzed and the values were compared to the ones required by the regulation. Numerical tests were also executed to evaluate the performance of the vehicle in a lateral collision against a rigid pole based on ECE R135. In this simulation it was used the “50% World Side Impact dummy” and it was evaluated model’s responses of the head, thorax and shoulders. The dissertation also presents a discussion about the difficulties found in the simulations and how they could be overcome.

Keywords: Pedestrian safety, crashworthiness, electric vehicle, finite element method, human body model.

RESUMO

DUARTE, M. R. G. **Projeto de um veículo seguro contra impactos da ONU utilizando modelos do corpo humano**. 2021. 126f. Dissertation (Masters Degree) - Polytechnical School, University of São Paulo, São Paulo, 2021.

Esta dissertação apresenta o projeto de um Automóvel Urbano Seguro capaz de atender aos requisitos de segurança automotiva estabelecidos pela Comissão Econômica das Nações Unidas para a Europa. O veículo elétrico foi desenvolvido para ser utilizado no ambiente urbano, tendo espaço para dois assentos e para carregar pequenas compras ou bagagens. A avaliação do projeto foi realizada utilizando a formulação explícita do Método dos Elementos Finitos. Primeiramente foi analisado o teste de impacto frontal baseado na ECE R94, em que o modelo colide contra uma barreira deformável sobrepondo 40% de sua largura. Esta simulação foi realizada utilizando os tradicionais Dispositivos de Teste Antropomórficos (ATD), comumente chamados *"dummies"*. Foram analisadas as respostas do corpo e da cabeça do modelo e os resultados comparados aos valores especificados pela regulamentação. Em seguida foi analisado o impacto do carro contra pedestre utilizando a regulamentação ECE R127 e modificações à estrutura do veículo foram propostas. Na análise, os tradicionais *"dummies"* foram substituídos por complexos dispositivos antropomórficos baseados no corpo humano contando com tendões, ossos e órgãos. As respostas foram analisadas e os valores obtidos foram comparados aos exigidos pela regulamentação. Testes numéricos também foram realizados para avaliar o desempenho em uma colisão lateral contra um poste rígido baseado na ECE R135. Nesta simulação foi utilizado o *"50% World Side Impact dummy"* e foi avaliada a resposta do modelo para cabeça, tórax e ombros. A dissertação ainda apresenta uma discussão sobre as dificuldades encontradas durante as simulações e como foi possível superá-las.

Palavras-chave: Segurança de pedestres. Teste de impacto. Veículo elétrico. Segurança. Método dos elementos finitos. Modelo do corpo humano.

LIST OF FIGURES

LIST OF TABLES

LIST OF ABBREVIATIONS AND ACRONYMS

ACEA	European Automobile Manufacturers Association
ACL	Anterior collateral ligament
AUS	Safe Urban Vehicle (from Portuguese *Automóvel Urbano Seguro*)
CPC	Car to pedestrian collision
EU	European Union
EVs	Electric vehicles
FE	Finite element
FEM	Finite element method
GHBMC	Global Human Body Model Consortium
ICEVs	Internal combustion engine vehicles
LCL	Lateral collateral ligament
LSTC	Livermore Software Technology Corporation
M50-O	50th percentile male vehicular occupant model
M50-PS	50th percentile male pedestrian simplified model
MCL	Medial collateral ligament
NURBS	Non uniform rational basis spline
OFD	40% offset deformable barrier
PMHS	Post mortem human surrogate
UN	United Nations
UNECE	United Nations Economic Commission for Europe
WHO	World Health Organization

CONTENTS

1 INTRODUCTION

The way cars are being manufactured has suffered tremendous changes in the last decades. Vehicles appeared in the nineteenth century and were seen as substitutes of carriages pulled by horses. They were heavy, slow and not designed with safety concerns in mind however, with its popularization and increase of speed, accidents became a major problem.

Deaths related to road traffic are epidemic and continue to grow. In 2010 the global death rate per 100,000 population was 18.8 and although this rate was reduced to 18.2 in 2016, this was not sufficient to compensate for the growth in population and quantity of cars. As a consequence, the absolute number of deaths continues to grow, going from 1.15 million in 2010 to 1.35 in 2016, Figure 1. In addition to that, vehicle related deaths are today the main cause of fatalities in children and young adults with ages between 5-24 years in USA, Table 1[1], and it is an important cause of death in all other age ranges. These are alarming data since more people die from car crashes than from HIV/AIDS or tuberculosis. (WHO, 2020).

Figure 1 – Number and rate of road traffic death per 100,000 population: 2000-2016

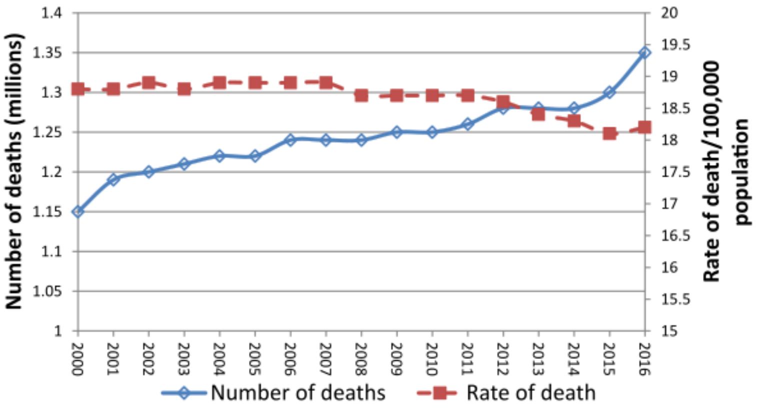

Source: Adapted from WORLD HEALTH ORGANIZATION (2018)

---

[1] Table 1 presents 8 month aggregate COVID 19 mortality rates during the period March - October 2020 and mortality rates for other causes during the period March - October 2018 in USA, the most recent year for which detailed deaths causes are available.

Table 1 – Age specific mortality rates (per Million) for COVID 19 (March - October 2020) and other leading causes of death (March-October 2018) in USA

	Cause of death							
Age, y	Transport Accidents	COVID 19	Heart Disease	Malignant neoplasms	Chronic lower respiratory disease	Accidental drug overdoses	Suicide	Homicide
<1	15.5	7.4	51.6	8.6	2.9	1.6	0.0	46.7
1-4	17.5	1.0	4.8	13.1	2.0	0.3	0.0	15.6
5-14	14.6	1.0	2.7	13.5	2.0	0.4	9.4	4.7
15-24	108.3	9.9	13.8	20.9	2.8	66.1	97.0	72.1
25-34	113.2	38.6	52.1	53.7	4.2	220.7	120.9	78.8
35-44	93.8	109.9	169.1	172.0	10.1	234.0	128.1	54.7
45-54	100.7	294.8	509.7	597.5	56.1	208.2	140.3	33.9
55-64	105.0	683.3	1239.8	1802.4	285.8	161.2	139.8	23.7
65-74	99.2	1574.6	2516.9	3702.0	809.9	50.8	114.1	15.7
75-84	129.9	3832.4	6845.7	6845.7	2117.3	16.0	129.6	13.2
>=85	139.1	10 699.7	24 530.2	10 442.4	4278.4	14.7	133.4	13.3
Total	89.2	698	1287.7	1219.8	307.5	122.3	102.3	39.0

Source: Adapted from Woolf, Chapman and Lee (2020).

The International Traffic Safety Data and Analysis Group (IRTAD), a group working in more than 40 countries to evaluate the tendency in road traffic deaths presented its statistics to check how the casualties have behaved between 2010 and 2018, Figure 2. Although it is possible to observe a decrease in the number of deaths of the signatory countries, the UN target of 50% reduction in 10 years, starting in 2010, was not reached. Unfortunately Brazil is not part of the group and Brazilian statistics are not included in the presented data.

Figure 2 – Number of casualties of road traffic from IRTAD member countries.

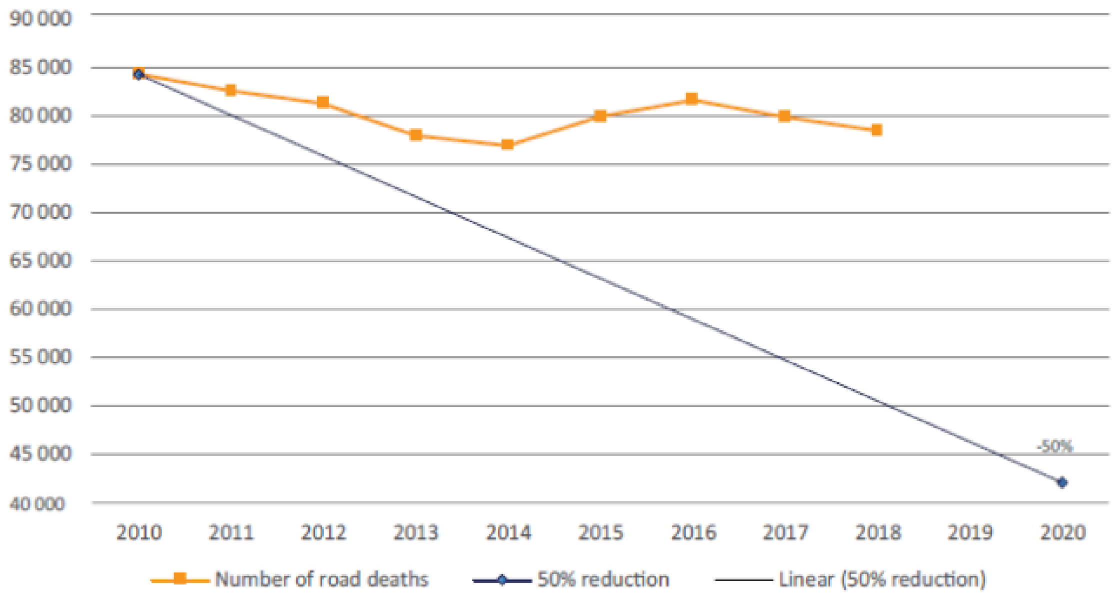

Source: IRTAD (2020)

Crash safety regulations play an important role to reduce the number of road traffic deaths. The first set of international standards was presented in 1958 by the United Nations Economic Commission for Europe, (UNECE, 1958). In the agreement, a series of requirements should be taken in vehicle production of the signatory countries, Figure 3 . UNECE published another agreement in 1998 getting support of more countries. Unfortunately Brazil was not signatory of any of these agreements. Even so, Brazil is making improvements in its regulations which, unfortunately, are not as rigid and mature as European Union (EU) or United States ones. Frontal crash test, for example, was considered mandatory only in 2007 and pedestrian car crash regulation is foreseen to take effect only in 2025, (CONSELHO NACIONAL DE TRÂNSITO, 2018). This part explains why death rates in Brazil are higher than European rates. WHO estimates that 41,007 people died in Brazil in 2016 directly due to road traffic, i.e. 18.3 people per 100,000 population. In high income countries this rate is 8.3 deaths per 100,000 people (WORLD HEALTH ORGANIZATION, 2018).

In 2020, the profile of people involved in traffic accidents suffered a change. With

Figure 3 – Signatory countries of the UNECE 1956 and 1998 agreements.

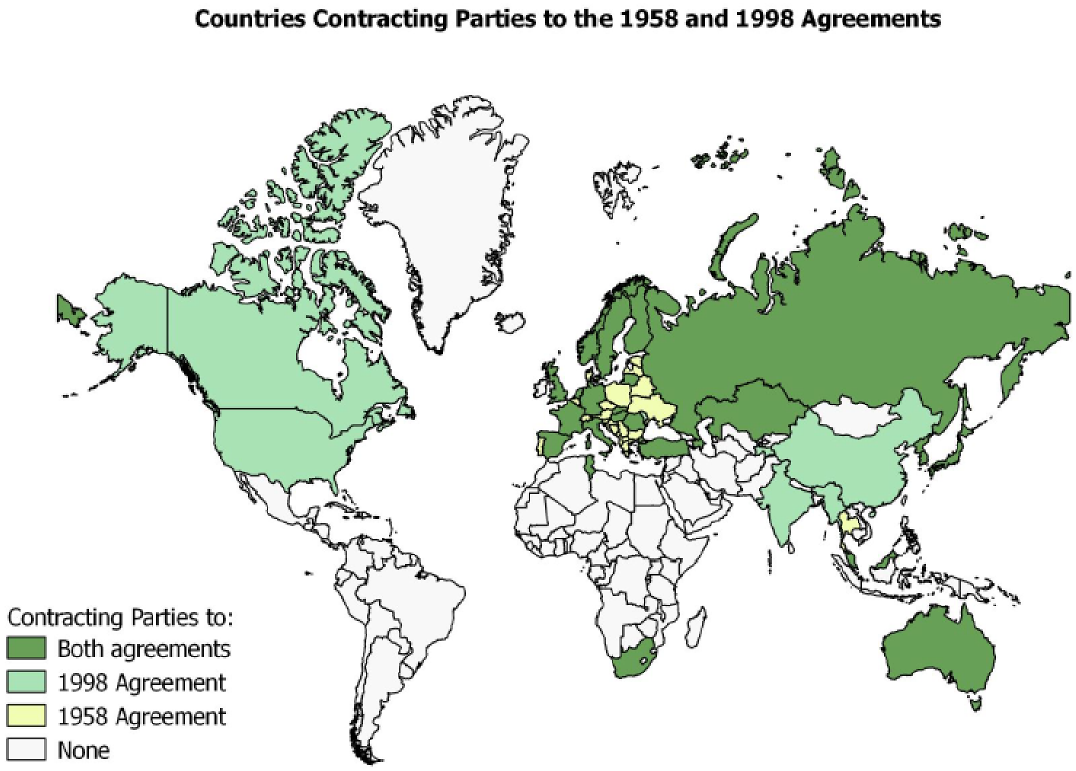

Source: Adapted from UNECE (1958).

the corona virus crisis, elderly and young people, which were the most affected in car to pedestrian collisions, stayed more at home. As consequence, it was observed an increase in the share of accidents suffered by people aged from 25 to 64. Barnes et al. (2020) presents a study using data from Louisiana (USA) to show how the lock down altered traffic injuries. In the study they state that in this period a reduction of 47% in total traffic accidents was observed, suggesting that reducing the traffic on roads would have a considerable impact in accidents and consequently a large reduction in car crash externalities. It also suggests that improving the home office would save millions of dollars in public health.

1.1 Vulnerable road users

Vulnerable road users suffer disproportionately from car accidents. Pedestrians, cyclists and motorcyclists are responsible for more than half of vehicle related deaths but they are largely ignored in countries' regulations, (WORLD HEALTH ORGANIZATION, 2018). In the case of pedestrians, due to the their vulnerability, the accidents tend to have more serious consequences, representing an important cause of morbidity and mortality.

From November, 2019 to October, 2020, 1145 pedestrians died only in the state of São Paulo, Brazil, an average of 3.13 pedestrians per day in a year, (INFOSIGA, 2020).

In the same period, 1912 motorcyclists and 1241 vehicle users died, making pedestrians the third group that suffer most traffic related obits in the state. This is already alarming but we have to take into consideration that 2020 was marked by the COVID 19 crisis, that affected tremendously the way people use the streets. To make a comparison, the same data collected from November 2018 to October 2019 showed that 1408 pedestrian, 1891 motorcyclists and 1400 vehicle occupants died, making pedestrian the second group with more deaths. Pedestrians are extremely affected by road traffic, their accidents are much more harmful than those involving other kinds of transportation, but they are yet extremely disregarded in Brazilian regulations and vehicle design.

Some improvements should be made in Brazilian road traffic accidents data tracking. For example, no follow up of the victims is done. This information is important to check which are the most affected parts of the victims, how many of them had irreversible damage, which proportion came to obit days after the accident, etc. The Brazilian Federal Highway Police (PRF) presents some data in its website (PRF, 2020) but in the spreadsheet only a total of 270 pedestrian deaths in 2020 was recorded in all Brazilian territory.

Martin, Lardy and Laumon (2011) performed a study based on data from the Rhône Départment Road Trauma Registry to analyze which parts of the pedestrians´ body were most impacted in crashes as well as its severity in the Rhône Department. It is stated that pedestrians are the fourth group most involved in accidents (9.3%), after car occupants, motorized two-wheeler users and cyclists. Even so the lethality is higher for them. According to Figure 4, two regions are the most affected in car crashes. The first is the one containing lower extremities and the second is the one containing head, face and neck. Using the Abbreviated Injury scale (AIS), a scale that goes from 1 (minor damage) to 6 (not survivable), the severity damage per region was categorized. Although the lower extremities are the most affected parts, rates of AIS4+[2] occurred more frequently when the head was involved in the accidents. Table 2 shows that the injury damage increase with age and is very critical for people older than 60 years old, where almost 60% of the car to pedestrian collision resulted in MAIS2+ and the lethality reached 5.7% of the cases.

Table 3 also shows that the most affected regions were lower extremities (50%), head, face or neck (38%) and the upper extremities (26%). Still according to the data the most frequently injured part of the lower extremity are legs and the most common symptom of head injury is loss of consciousness. Martin, Lardy and Laumon (2011) affirm that most of the MAIS2+ injuries to head involved the brain and cranium. The probability of sustaining a pelvic injury increased sharply with age after 40 years old. The most

---

[2] When the damage is categorized as a certain scale or superior, the symbol "+" is added to indicate this. E.g. AIS3+ means AIS3, AIS4, AIS5 or AIS6. It is frequent in a casualty more than one AIS scale occur, in this case letter "M" is added prior to the AIS to indicate the most severe injury (maximum). E.g. MAIS3+ indicates that the studied cases will have the maximum AIS between AIS3 and AIS6 (HAPPIAN-SMITH, 2002).

Figure 4 – Pedestrian injury pattern in Rhône Department, 1996-2007.

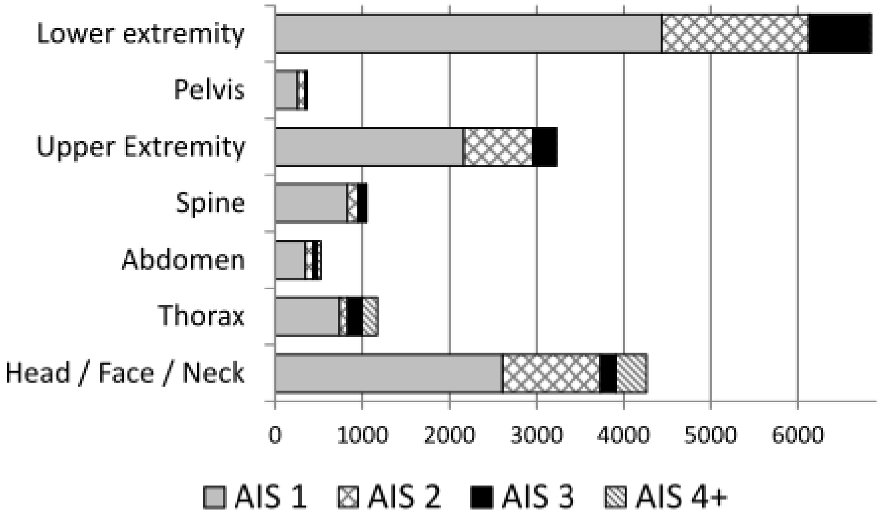

Source: Martin, Lardy and Laumon (2011).

Table 2 – Age distribution of the number of pedestrians involved in collisions with a car in Rhône Department, 1996-2007.

Age	Absolute number	Percentage (%)	Lethalities (%)	MAIS2+ (%)
0-1	47	0.5	2.1	23.4
2-4	419	4.9	1.2	28.2
5-10	1062	12.4	0.4	33.9
11-16	1195	14.0	0.4	34.1
17-39	2740	32.0	0.6	30.3
40-64	1751	20.4	2.2	44.3
>64	1352	15.8	5.7	59.1
Total	8566	100	1.7	38.5

Source: Martin, Lardy and Laumon (2011).

common were thigh injury (open/displaced/multifragmentary fracture). With regard to the leg, most common injuries were fibula fracture.

Clearly, Brazilian regulation for pedestrian safety should be implemented as soon as possible to reduce the obits and the severity of accidents involving this vulnerable group. UNECE (2012) foresees car to pedestrian collision (CPC) tests considering injuries related to head, pelvis and lower limb, which are the human body parts most impacted in this kind of accident. For this reason, the existing regulatory tests seam to be appropriate. Fildes et al. (2004) however show that thorax sustains most of the severe fatal injuries, indicating that it should also be analyzed in the demanded regulatory tests.

Table 3 – The nature of the injury, the injured body region part among pedestrian casualties of over 2 years of age (both survivors or fatalities) with at least one AIS2+ injury,Rhône Department, 1996-2007 (N=3289).

Injured body region		Number of casualties with at least one AIS2+ injury	% victims
Head, face or neck		1252	38.07
	Loss of consciousness	839	25.51
	Cranium	171	5.20
	Intracranial injury	267	8.12
	Neck	6	0.18
	Scalp, face, eyes	178	5.41
Thorax		281	8.54
	Rib cage	196	5.96
	Sternum	19	0.58
	Diaphragm	2	0.06
	Respiratory tract	99	3.01
	Circulatory system	8	0.24
	Esophagus	2	0.06
Abdomen		98	2.98
	Genitourinary system	30	0.91
	Digestive system	39	1.19
	Spleen	36	1.09
Spine		139	4.23
	Cervical spine	50	1.52
	Thoracical Spine	47	1.43
	Lumbar spine	55	1.67
Upper extremities		870	26.45
	Shoulder or arm	512	15.57
	Elbow or forearm	275	8.36
	Wrist or hand	121	3.68
Pelvis		289	8.79
Lower extremities		1630	49.56
	Hip	84	2.55
	Thigh	117	3.56
	Hip/thigh other	36	1.09
	Knee	463	14.08
	Leg	657	19.98
	Ankle	282	8.57
	Foot	159	4.83

Source: Martin, Lardy and Laumon (2011).

1.2 Electric vehicles

Industry has evolved and new technologies have been developed to reach sustainable and safe automobiles. The first electric vehicles (EVs) were produced in the end of the nineteenth century, and their use became fairly wide. Between 1856 and 1881, electric motor and direct current (DC) had a lot of improvements (YONG et al., 2015). In this period, electric motors with high efficiency were developed due to efforts of Werner Siemens, Antonio Pacinotti and Zénobe Gramme (GUARNIERI, 2011a) and the first practical rechargeable lead-acid battery was invented by Gaston Planté in 1859 being improved by Camille Alphonse Faure around 1881 (GUARNIERI, 2011b). The first EV introduced to the public was a cab in 1897. It made such success that in only three years 28% of the road fleet was electric, reaching a peak of 30,000 units in 1912 (GLOBAL. . . , 2014). As an example, Figure 5 presents *"La Jamais Contente"*, an EV that held the world land speed record in 1899.

Figure 5 – “La Jamais Contente”, electric vehicle that held the world record of land velocity in 1899.

Source: Larminie and Lowry (2012).

After a decade of success, EVs faced a great challenge. In 1908 internal combustion engine vehicles (ICEVs) were brought to the market and once the cheap oil became available, technology trailed its way in other direction. At that time the most popular type of battery was the lead acid, and comparing the specific energy of a battery and gasoline, it is quite obvious the reason of the choice. Specific energy for internal combustion engines, considering the efficiency of the motor, is around 1800 $\mathrm{W\ h\ kg^{-1}}$, whereas the useful specific energy of a lead acid battery is around 27 $\mathrm{W\ h\ kg^{-1}}$. To illustrate the difference, a typical contemporary car would have an autonomy of 50 km with 4.5 l of oil, which is equivalent to approximately 4 kg. To obtain the same autonomy, a set of lead acid batteries would have a mass of about 270 kg (LARMINIE; LOWRY, 2012). Besides that, in 1912 Charles Kettering invented the electric starter, removing the need of hand crack to start the gasoline powered vehicles. As result, EV faded out of popularity and in 1935 there was none EV being commercialized or running on the roads.

A few decades later, due to the raise of oil price and the emission of gasoline powered-vehicle, the interest in EVs was renewed. Governments implemented regulatory actions to promote electric vehicles to reduce air pollution. An example of these regulations is the California´s Zero Emission Vehicle Mandate, from 1990, which required two percent of the total fleet in California to be zero emission between 1998 and 2003 (BELLIS, 2019). Since then, the automobile industry has put many efforts producing hybrid / electric vehicles. In 1996 General Motors released EV1, Figure 6, the first mass production EV ever made. In the next year Toyota released in Japan its first commercial hybrid electric vehicle (HEV), Toyota Prius, and in the first year of production 18,000 units where sold (BELLIS, 2019). From the year of 2010 ahead, electric vehicles have started to gain market and other companies began to produce their own models such as Nissan Leaf, Mitsubishi i-MiEV, Chevrolet Volt and Tesla Model S.

Figure 6 – EV1, the first mass produced EV.

Source: https://www.flickr.com/photos/rightbrainphotography/2223283465/in/photostream/.

Figure 7 presents the number of electrical cars around the world from 2013 to 2018. From the data it is possible to realize that in 6 years the quantity of electrical cars increased from 230 thousand to 3,3 million, i.e. a factor of more than thirteen times. China almost doubled the quantity of EVs year after year and comparing 2017 and 2018 there is an increase of 70% in the quantity of electric vehicles. This quick expansion indicates that EVs are working to continue increasing in number, becoming an important transportation mean in the next years.

Figure 7 – Quantity of full electric cars (from 2013 to 2018).

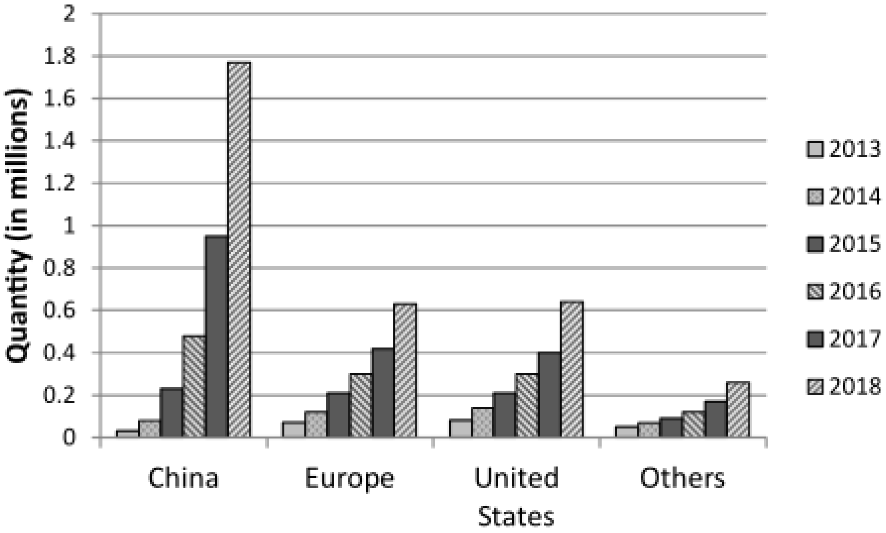

Source:Adapted from IEA (2019).

Although in more developed countries EV is already a reality, it is almost nonexistent in Brazil. According to SINDIPEÇAS (2019) Brazil had a fleet of 58 million vehicles in 2018. Of this fleet, 67.1% were ethanol/gasoline propelled, 22.2% where only gasoline propelled and 10% used diesel as fuel. Only 11,038 units where completely electric or hybrid, 0.025% of total.

To change this scenario, Brazil published the Law 13,755/18, popularly known as *"Rota 2030"* (BRASIL, 2018), which provides many incentives to the national industry to improve the automobile production and investments in Research and Development. *Rota 2030* intends to:

- Establish mandatory requirements for the vehicle commercialization;
- Improve the energetic efficiency and the availability of new technologies;
- Improve the investments in R&D;
- Initiate the production of new technologies and innovation; and
- Guarantee technical improvement of professionals in mobility and logistics sector.

EVs are also facing new issues that were not a huge problem when compared to the conventional internal combustion engine vehicles (RAMONI; ZHANG, 2013). While in ICEVs the major components have an average of 15 year life, the battery of an EV can last much less (MARANO et al., 2009). What to do with these components when they are discarded is not yet a consensus.

1.3 The future of EV after COVID 19

Corona virus disease crisis has altered the international market and one of the most affected sectors is vehicle manufacturing (HOMM et al., 2020). To compensate this, many companies are lobbying to maintain their profits. One of the demands is reduction of CO_2 emission limits. These limits are very strict in EU, China and USA, which are the three regions that are pushing the technology advances in EVs. With the sales drop due to the period of quarantine, when people are restricted at their homes, it has been observed an increase in the companies' attempts for a relaxation of those limits.

On march 25, 2020, the European Automobile Manufacturers Association (ACEA) wrote a letter to the president of the European Commission asking for a relaxation of cars CO_2 targets. These targets were set in 2008 demanding that in 2020 95% of the new passenger cars should release less than 95gCO2 per km. This demand should be applied to 100% of the new passenger car sales in 2021.

Ex-president Donald Trump has already relaxed rules in USA. Previous regulation demanded that automakers had to reach the consumption of 4.3 l/100 km (101 gCO2 per km) in 2026 for the new sales. With the new regulation presented by the National Highway Traffic Safety Administration and the Environmental Protection Agency on April 2020 the consumption target for the new sales in 2026 in the USA is now 5.9 l/100 km (136 gCO2 per km) (DAVENPORT, 2020). This is a huge obstacle in the development of new technologies for the EVs since these emission values are easily attained with a mild hybridization of part of the fleet, without the necessity of investments in battery electric vehicles.

Besides, it is likely that the sales in vehicles be reduced drastically for next years, which would also affect the investments in developing the electric mobility. During the crisis lots of people had their payments reduced, generating a cascade effect affecting directly the gross domestic product all around the world. Great part of the population will prefer to save money due to uncertainties and even people who would like to switch cars may not be able to do that.

Due to these facts automakers should be rescued by governments and depending on the choices made, EVs could return after the pandemic stronger than they were before. According to Homm et al. (2020) among the developed countries with a relevant automotive industry only Germany and China have low national debt and can help their companies with large rescue packages. These two countries already rely on electric mobility as future technology and will, probably, focus on this. The result may be an increase in market share of the companies of these countries and consequently an increase in market share of electric vehicles.

Figure 8 – AUS, the Safe Urban Vehicle. (a) Finite element model and (b) CAD rendered model.

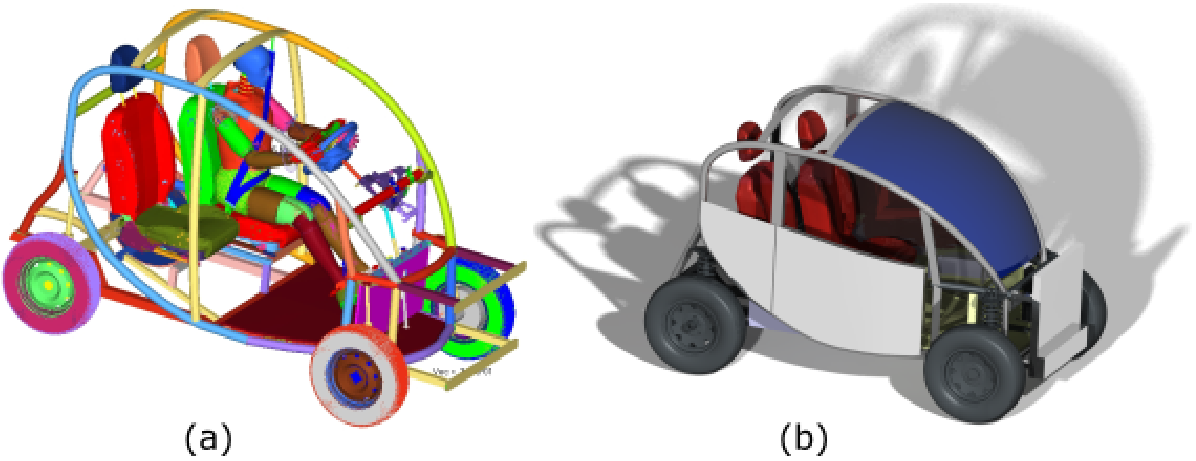

Source: from author.

1.4 AUS - A safe, electric and compact vehicle

Bearing in mind what has been presented so far, and considering the lack of electric cars in Brazil, there is a need of a national vehicle capable to comply with international safety regulations. Hence the conception of a small urban car for two occupants suitable to use in the urban spaces of big cities was idealized, Figure 8.

Targeting design requirements were:

- Autonomy of 100km;
- Cruise velocity of 90km/h;
- Space for small luggage or daily shopping;
- Passengers and pedestrian safety.

These requirements were adopted thinking in the daily use of an average person in a big city. With this autonomy it would be possible to perform any commuting home-job-home in a work day without the need of recharging. Also, in São Paulo, with the defined speed, such a car is capable of performing well in any urban area.

Since deaths related to the road traffic are a major problem nowadays, it is fundamental that a conceptual vehicle be in accordance with the most recent regulations used in countries where death rate is low. European countries that obey United Nations Economic Commission for Europe (UNECE) vehicle regulations are good examples. For this reason AUS, from *Automóvel Urbano Seguro*, shall comply with these regulations.

Figure 9 – The original 50th percentile male Hybrid III's family expanded to include a 95th percentile male, 50th percentile female, and ten, six, and three-year-old child dummies.

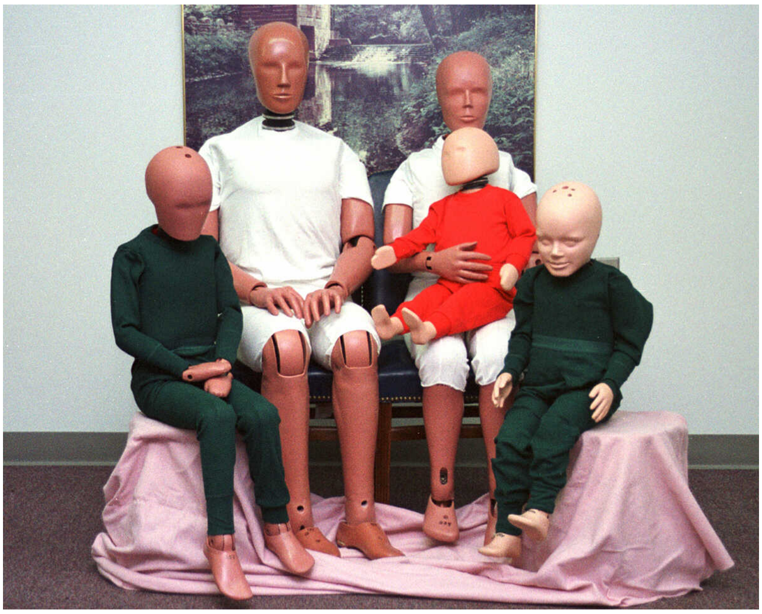

Source: United States Department of Transportation.

AUS design is primarily based on a tubular structure. Some of the impact energy can be absorbed by energy absorbers placed on its front and rear. Frontal and lateral air bags will ensure safety of the occupants and batteries were positioned below the users, reducing the vehicle center of gravity, allowing it to be more stable.

Vehicle suspension was designed trying to utilize existing shock absorbers and springs. The main idea was to use independent suspensions to let the car firm and to simplify the assembly. Here a MacPherson type was adopted to be used in the four vehicle wheels.

The main idea of the presented study was to perform numerical simulations to evaluate the viability of the vehicle to comply with car crash test regulations, specially the one concerning pedestrian safety. Usually a dummy model represents the human body in real crash tests, Figure 9, and a finite element model of the dummy is used in the numerical simulations. Nowadays, a new class of human body models (HBM), made directly from scans of human bodies, as presented in Figure 10, is starting to be developed with the objective to represent human body responses more accurately. Its use in the present context is one of the objectives of this dissertation.

Figure 10 – Anthropomorphic test device models of an adult and a child. On the left the usual finite element dummy models and on the right the human body models.

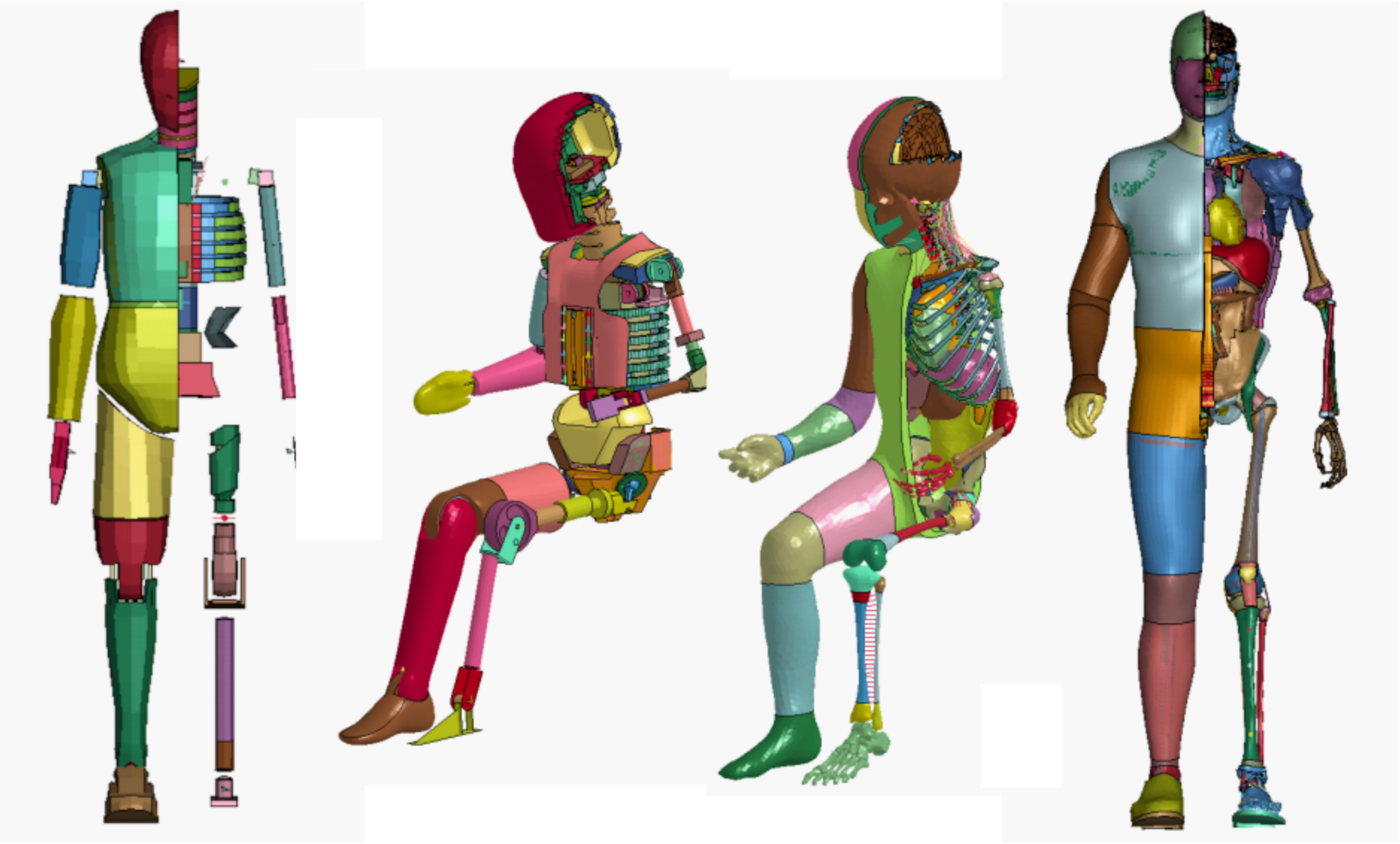

Source: from author.

2 OBJECTIVE

The aim of this project is to develop a vehicle able to comply with United Nations Economic Commission for Europe safety regulations for ECE R94 (protection of the occupants in the event of frontal collision), ECE R135 (pole side impact performance) and ECE R127 (car to pedestrian collision). Use was made of finite element models based on the human body and on traditional dummies, so a comparative study of these models is performed.

The study is organized in a way that Chapter 3 presents the methodology. The chapter covers CAD and mesh models, finite element pre processing parameters and the regulations used to evaluate the vehicle. It also defines the vehicle materials and the model main dimensions.

On Chapter 4, a review of the Human Body model, used on the car to pedestrian collision, is presented.

Chapter 5 presents the results obtained on the simulations for frontal crash test, car to pedestrian collision and lateral impact, with chapter 6 presenting a discussion on the modifications performed in the model and difficulties encountered during the study.

Chapter 7 presents the conclusions and suggests further studies related to the EV development.

3 METHODOLOGY

The geometry of the vehicle was generated in CATIA from actual measurements of a body-in-white built in the GMSIE-USP (Solid Mechanics and Impact Group - University of São Paulo). From the geometry, the vehicle was meshed in a mesh generator (HYPERWORKS, 2017). With the mesh it was possible to assign mechanical properties, material, contacts, boundary conditions and other simulation parameters in a pre-processor (LSTC, 2017) and finally it was processed in finite elements (LSTC, 2020b). In the end, numerical results were compared with UNECE regulations to check if the requirements were met. If in a simulation the results are not satisfactory, modifications were proposed until the requirements were met. This is an iterative process in which geometry, thicknesses and materials were, within the ones available on the market, as off the shelf modified.

The project of a urban car at GMSIE-USP was initiated by de Lima (2016). In the study it was designed the first AUS model in finite elements. Lima's aim was to design a vehicle structure able to comply with UNECE regulations for frontal and rear crash impact. But this first attempt to create the vehicle considered its construction in a consolidated manufacturing plant. Some tubes had to be molded in three dimensions and many vehicle shapes and profiles would only be constructed through stamping processes (e.g B pillar). This would be very difficult to be achieved in this project step.

These manufacturing restrictions were observed when the first prototype was built, Figure 11. The contracted manufacturer was not able to construct the vehicle structure as designed. Modifications that allowed its construction were made (e.g. 3D molding was built as planar, big curvatures were made by welding two straight tubes and other modifications) and resulted in a prototype considerably different from that proposed by Lima.

In this study the built prototype, Figure 11, was used as the project basis. All the main dimensions and curvatures were collected from the prototype and not from Lima's model. From the constructed structure it was drawn a 3D CAD model and a new finite element model. After that, the FE model was simulated and modifications in its shape, material and thicknesses were performed to ensure that the vehicle could obey UN car crash safety regulations. It was also performed a car to pedestrian collision (CPC) evaluation, which was not checked on Lima's work. In this CPC a human body model was used, which is an improved representation of a human body and is discussed in details in chapter 4.

Figure 11 – AUS, the Safe Urban Vehicle.

Source: from author.

3.1 CAD and CAE modeling

3.1.1 CATIA model

The first step in the work was to model the vehicle structure in Computer Aided Design (CAD) software, Figure 12. CATIA (Computer-aided three-dimensional interactive application) version 5.21 was chosen to perform the task. CATIA is a high-end CAD tool, being widely used in automobile industry with many tools to perform different designs (CATIA, 2020).

Although it was possible to design the whole vehicle in FE meshing software, e.g. Hypermesh, it was decided to use a CAD software and export the components to the pre processor. CAD has a considerable amount of tools to draw plates, profiles, lines and to work with the interaction among the components. FE pre-processors are generally focused for meshing or for simulation parameters assignment.

Other advantage of using CAD software is that commercial drawings with measures and construction specifications can be made very fast.

The final vehicle dimensions are presented in Figure 13. In the figure it is possible to observe that the final main dimensions of the vehicle are 2.53m length, 1.49m width and 1.70m height. Detailed component drawings are presented in Appendix F.

Figure 12 – AUS prototype.

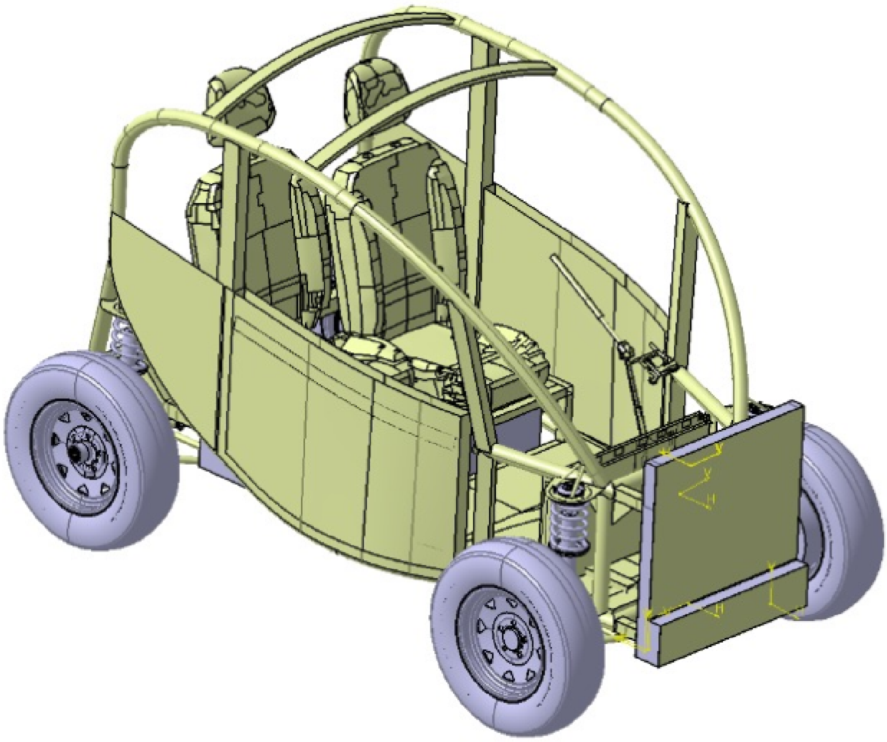

Source: from author.

3.1.2 Mesh modeling

Mesh modeling was performed using Hypermesh, (HYPERWORKS, 2017). This software is capable of meshing complex geometries and has interface with most of the commercial finite element solvers (Abaqus, LS-Dyna, PamCrash, Nastran and others).

In Hypermesh it was possible to use some finite element models (tires, wheels, steering wheel) from CCSA (2021), LSTC (2020c) and implement them into AUS. On LSTC (2020c) it is also possible to download dummy models for crash simulation. They can be used free of charges by LS-Dyna users. In this study it was used, from LSTC site, Dummy Hybrid III 50th percentile, (UNECE, 2017b) and the Side impact dummy (SID) for the ECE R135 lateral impact evaluation. It was also possible to use a human body model, a finite element model that represents the human body with tendons, tissues and organs (GHBMC, 2020).

The final version of the mesh models information can be seen in Table 4. According to the table it is possible to see that AUS model with the human body model has almost two million elements. This made the 150ms simulation last approximately 3 days on a Intel i7-8700 with 8GB RAM installed.

Figure 13 – AUS main dimensions (in millimeters).

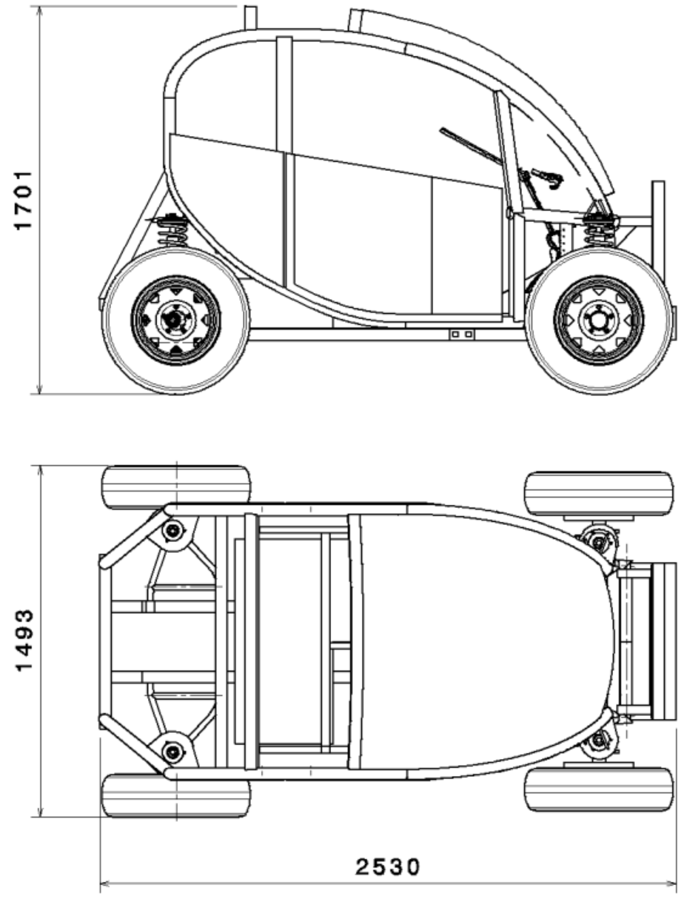

Source: from author.

3.2 Pre processing

With the mesh generated in Hypermesh it was possible to perform the pre processing. This step was performed on LS-PrePost, LSTC (2017). LS-PrePost can be obtained free of charge and it is compatible with LS-Dyna solver.

In this phase it is defined all the physical properties that will allow the calculation of the structural dynamic problem. More details on the explicit finite element method can be found in Appendix B and the model shapes are presented in Appendix F. The other properties used are presented in the following sections.

3.2.1 Materials

The material chosen to be used in AUS tubes was DP1000. This material is an Advanced High Strength Steel (AHSS) that due to its high impact energy absorption and its high yield strength has been widely used in the automobile industry. In LS-Dyna it was used Johnson Cook (JC) model to simulate the material constitutive relations (JOHNSON;

Table 4 – Quantity of nodes and elements of the used FE model.

	AUS	Human body model	Frontal dummy model	Lateral dummy model
Nodes	655 751	542 909	279 203	450 615
Beam elements	37 469	2 548	256	84
Shell elements	626 130	184 847	238 052	25 392
Solid elements	284 960	646 785	227 632	405 063
Discrete elements	2	44	1	14
Total elements	948 561	834 224	465 941	430 553

COOK, 1983). In JC constitutive model the effective stress may be calculated by

$$\sigma = (A + B\varepsilon^n)\left(1 - C\ln\left(\frac{\dot{\varepsilon}}{\dot{\varepsilon_0}}\right)\right) \tag{3.2.1}$$

where σ is the equivalent stress (von Mises), ε is the equivalent strain, $\dot{\varepsilon}$ is the equivalent strain rate, A, B, C and n are material constants and $\dot{\varepsilon_0}$ is the reference strain rate.

Johnson Cook's uses an isotropic hardening model. This is valid in a crash scenario since it is not generally observed stretch cycles. An element which suffers a compression (tension) would not be subjected to a plastic tension (compression) in a posterior moment. Johnson Cook's model is also interesting to be used because its parameters are widely found on internet for a large amount of materials, besides, it considers the strain rate effects, which should be considered in an event with large and quick deformations, e.g. a crash event (NOH; LEE, 2020).

In LS-Dyna JC constitutive model can be entered through the keyword *MAT_SIMPLIFIED_JOHNSON_COOK (MAT098) and the material constants used where obtained from (SONG; DAI, 2013). From the study, the constants are $A = 673.6$ MPa, $B = 1303$ MPa, $n = 0.4217$, $C = 0.0168$ and $\dot{\varepsilon_0} = 10^{-4}\text{s}^{-1}$. Besides that it was used $E = 210$ GPa, $\nu = 0.28$ and $\rho = 7.8$ ton*m^{-3}.

On the honeycomb and vehicle door plates it was used Aluminium Grade 3003. This material is widely used in Aluminium honeycomb and by the automotive industry. For the LS-Dyna it was also modeled using JC constitutive model and the values of the constants are $A = 21.131$ MPa, $B = 133.8$ MPa, $C = 0.998$, $n = 0.169$ and $\dot{\varepsilon_0} = 10^{-4}\text{s}^{-1}$ (LEEM et al., 2015). Besides that it was used $E = 70$ GPa, $\nu = 0.3$ and $\rho = 2.7$ ton*m^{-3}.

The windscreen of the vehicle was modeled with the material polymethyl methacrylate, known commercially as plexiglass. It was modeled as a single stress strain curve in LS-Dyna using MAT24, *MAT_PIECEWISE_LINEAR_PLASTICITY. The curve can be obtained from (WANG; XU; ZHANG, 2014). The used values are $E = 3$ GPa, $\nu = 0.3$ and $\rho = 1.2$ ton*m^{-3}. The material was considered to have a perfectly plastic behavior, so when its equivalent stress reached $\sigma_0 = 70$ MPa, its tangent modulus assumed the value $E_T = 0$ GPa. It was considered perfectly plastic because plexiglass is a brittle material and when its maximum allowed stress is reached, it does not present additional resistance. Other models of windscreen could also be used. Peng et al. (2013) suggests the use of a three layer windscreen: two of glass and one in the middle of polyvinyl butyral (PVB) that are usually used in vehicles. In this work the windscreen is modeled using MAT_LAMINATED_GLASS and MAT_PIECEWISE_LINEAR_PLASTICITY.

The air bags and seat belts materials are the same used in the internet available model of the Toyota Yaris, see the LSTC and CCSA websites (LSTC, 2020c; CCSA, 2021).

The summary of the used materials and keywords is presented in Appendix E.

3.2.2 Contacts

In the simulation three contact types were used.

The first one was the contact to guarantee that none AUS structure would penetrate each other. This was made through the keyword *CONTACT_SINGLE_SURFACE. With this keyword, a set of components including all AUS structures is defined and the solver evaluate the interaction between them, included the self contact of the components.

The second contact used was the *CONTACT_SPOTWELD. This contact was used in all welds applied to the vehicle. In this contact a beam is modeled between the welded parts and prevent them from disconnecting. Since the contact is used to join the parts, the beams do not need to be attached to any node. The beam ends will maintain the distance to the the connected parts. Although the weld beam and the shell connected to it may stretch, the lowest distance between the weld ends and the shells will remain unchanged. This type of connections allows the transmission of moments, shear and normal forces (HANSSEN et al., 2006).

The third contact used was the *CONTACT_SURFACE_TO_SURFACE. This contact was used when two surfaces impacted each other, e.g. barrier - bumper, pedestrian - vehicle or pole - vehicle. This contact type evaluates the position of the two bodies and prevents them to penetrate each other. In the calculation it may be added a Coulomb friction coefficient. In all the cases it was applied a 0.1 value. This contact was also used on the dummy - seat belts and on the dummy - air bag interaction.

3.3 Solver

LS-Dyna was chosen to be the solver used in the dissertation. LS-Dyna is a general purpose finite element code able to analyze large structure deformation. Its main solution procedure is based on explicit time integration. Besides, it has more than one hundred constitutive implemented models and has specialized capabilities to work with air bags, seat belts and sensors.

LS-Dyna is widely used in the automotive industry and many of the studies of crash tests were made using LS-Dyna as a solver. Other advantage is that to customers are provided models of dummies, barriers, wheels and others. Other reason to use this solver is that the human body model supplied by Elemance[1] was available only for LS-Dyna solvers. So if crash test analyses are going to be performed and if an interface with other automotive communities will be made, it is strongly recommended the use of the LSTC processor.

3.4 UN Regulations

The main goal of this project was to design a vehicle capable of complying with international car crash safety regulations. It was decided to use the United Nations 1958 Agreement (UNECE, 1958). In this convention a series of rules were defined to be used for vehicles commercialized in European Union. These regulations were chosen because they are being used in many countries and by the fact that EU has an enormous commercial relevance.

3.4.1 Frontal impact test - ECE R94

The first analyzed item was the frontal crash test (UNECE, 2017b). This regulation may be applied to vehicles of category M1[2] with a total mass not exceeding 2.5 tonnes, which is the case of AUS.

This regulation demands that two dummies corresponding to Hybrid III be seated in the front seats (UNECE, 2017b). This regulation also determines that the car impacts a deformable barrier with 40%±20mm overlap with a speed of 56km/h. Figure 14 presents the CAD drawing of the vehicle and barrier. The dummies were included on FE model.

The requirements of the regulation are presented on Table 5:

3.4.2 Car to pedestrian collision - ECE R127

Pedestrian safety was evaluated based on ECE R127 (UNECE, 2012). The regulation requires that an aluminium sphere (representing pedestrian head) and a foam cylinder (representing the pedestrian leg) be thrown against a fixed vehicle. In the impact, accelerations and displacements should be measured and analyzed. This is a huge simplification

---

[1] https://www.elemance.com/

[2] According to UNECE (2017a) vehicles category M1 are power driven vehicles having at least four wheels and used for carrying passengers. The vehicles in this category shall not have more than eight seats in addition to the driver´s seat.

Figure 14 – ECE R94 vehicle crash test condition (dimension in millimeter).

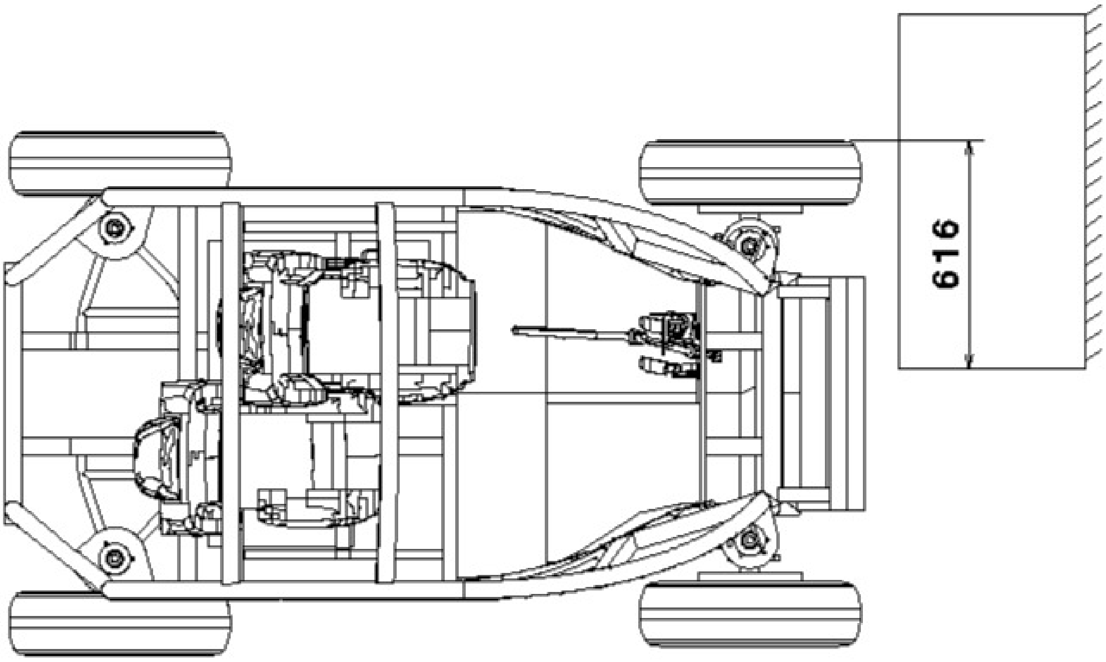

Source: from author.

Table 5 – Specifications of the frontal crash test.

Body part	Criteria	Specification
Head	Head injury criterion (HIC_{36})	Not to exceed 1000
	Acceleration	Not to exceed 80g for 3 ms
Neck	Injury criterion for the neck (NIC)	Below the values of Figure 15 and Figure 16
	Neck bending moment	Not to exceed 57 Nm
Thorax	Thorax compression criterion (ThCC)	Not to exceed 42mm
Leg	Femur force criterion	Below the values of Figure 17
	Tibia compression force criterion	Not to exceed 8 kN

Source: UNECE (2017b)

since in real life the vehicle (with speed) hits the pedestrian. In a real car to pedestrian collision the vehicle is never parked and its linear momentum is not negligible. Certainly the measured accelerations would have larger values.

Unfortunately it is difficult to make a realistic physical car to pedestrian test. The dummy would have to be hold in position until the impact moment and then be suddenly released. It is not easy to be accomplished since we are talking of a gap of 5 ms or less. Fortunately this is not an issue in FEM.

In this study it was simulated a more realistic car to pedestrian collision. The vehicle, with an initial velocity, impacted a pedestrian human body model and then the

Figure 15 – Neck tension criterion.

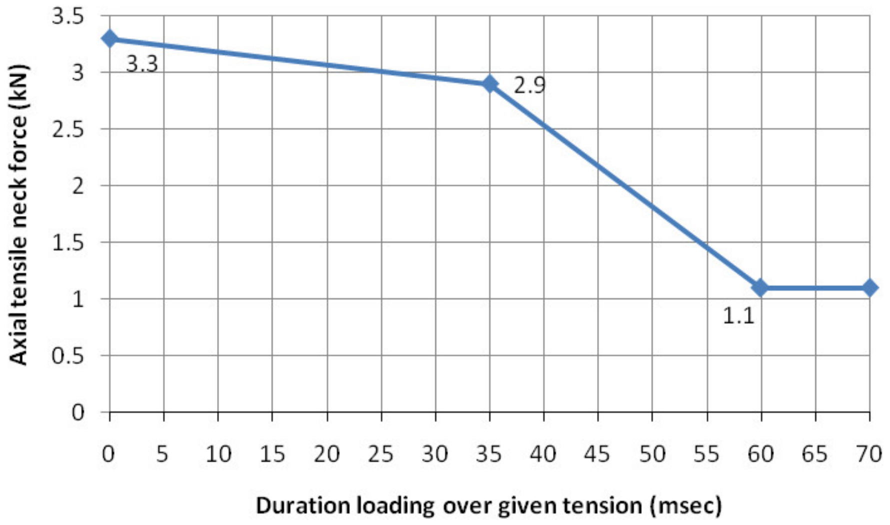

Source: UNECE (2017b).

Figure 16 – Neck shear criterion.

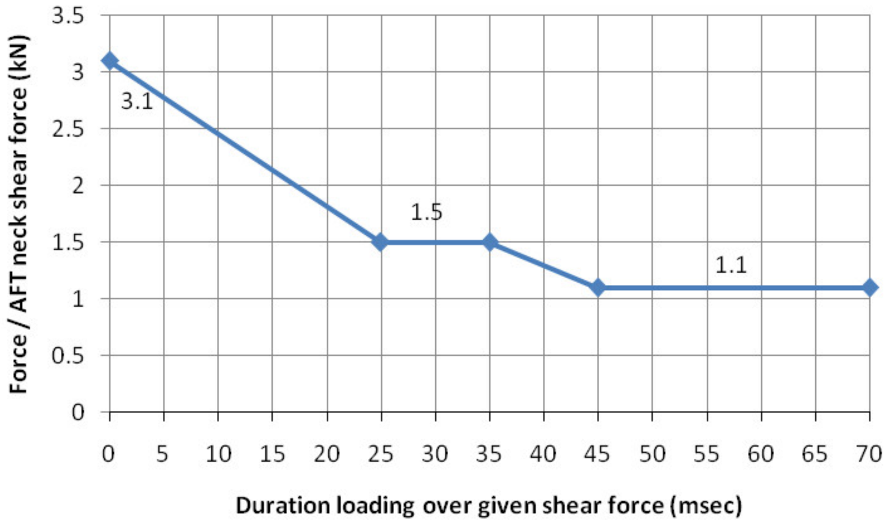

Source: UNECE (2017b).

accelerations and displacements were collected. This analysis is considerably more harmful since now the vehicle inertia is being considered and the involved impact energy is higher.

Besides that it will be used in this study a human body model to represent the pedestrian, chapter 4. Using an aluminium sphere and a foam cylinder to represent a whole human body, Figure 18, is a huge simplification. Using a human body model would result in a more realistic simulation and would allow collecting data that would not be possible to be obtained from traditional dummies.

Figure 17 – Femur force criterion.

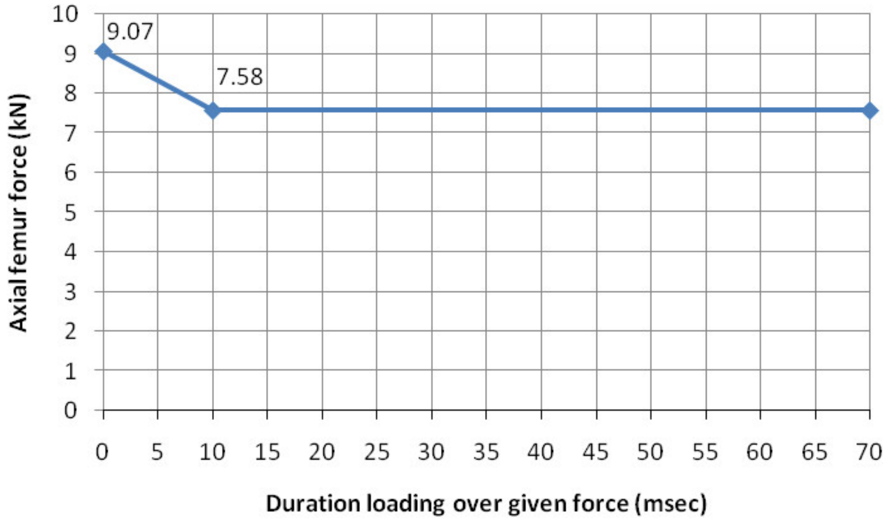

Source: UNECE (2017b).

Figure 18 – Traditional pedestrian anthropomorphic test devices.

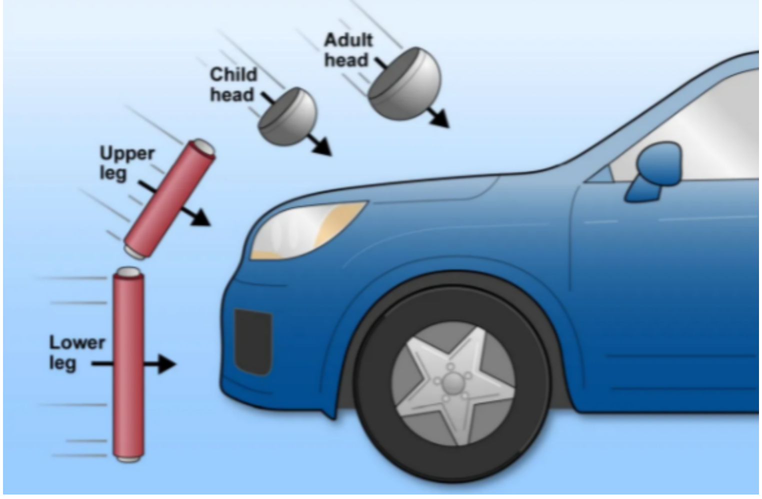

Source: US Government Accountability Office (2020).

On ECE R127 requirements, the dummy should crash the vehicle with a horizontal velocity of 11.1 ± 0.2m/s. In present simulation the same speed was used but applied in the vehicle that impacts a standing still pedestrian.

In the regulation there are two possibilities to evaluate the pedestrian results. If the lower bumper height[3] of the vehicle is inferior to 425mm, the requirements are presented in Table 6 and if the bumper is superior to 500mm, the requirements are presented in

---

[3] According to UNECE (2012) the lower bumper height means "... the vertical distance between the ground reference plane and the lower bumper reference line, with the vehicle positioned in its normal ride attitude".

Table 7. If the height is between 425 and 500mm any of the requirements may be applied.

AUS bumper height is 183mm, so Table 6 was used.

Table 6 – Specifications of the CPC. Vehicle bumper height inferior to 425mm.

Leg evaluation	Maximum dynamic knee angle	not to exceed 19°
	Maximum dynamic shearing displacement	not to exceed 6.0mm
	Acceleration at upper end of tibia	not to exceed 170g
Head evaluation	Head injury criteria	not to exceed 1000

Source: Adapted from UNECE (2012)

Table 7 – Specifications of the CPC. Vehicle bumper height inferior to 500mm but superior to 425mm.

Leg evaluation	Instantaneous sum of impact forces	not to exceed 7.5 kN
	Bending moment	not to exceed 510 Nm
Head evaluation	Head injury criteria	not to exceed 1000

Source: Adapted from UNECE (2012)

3.5 ECE R135 - Pole side impact performance

It was also performed a pole side impact crash test. In this test the vehicle should impact a pole with a speed of 32 km/h. The velocity vector should be in a 75 degrees angle with the longitudinal direction, as presented in Figure 19. In this test, the dummy, positioned on the driver side of the vehicle should have its head center of gravity aligned with the pole center.

In this test it should be evaluated the HIC, the peak shoulder force and the thorax ribs deflection. The threshold values are presented in Table 8.

Table 8 – ECE R135 crash test requirements.

Criteria	Requirement
HIC	not to exceed 1000
Peak shoulder force	not to exceed 3 kN
Thorax rib deflection	not to exceed 55 mm

Source: Adapted from UNECE (2016)

The dummy used for the test should be the World Harmonized Size Impact dummy (WorldSID), Figure 20. The WorldSID 50th percentile male dummy has a standing height of 1.75 m, seating height of 0.91 m, and a mass of 77.3 kg. It has symmetrical response (left/right) and is able to be used in side impacts up to ±30° from the pure lateral impact direction (YOUN; LEE; KIM, 2000).

Figure 19 – ECE R135 crash test configuration.

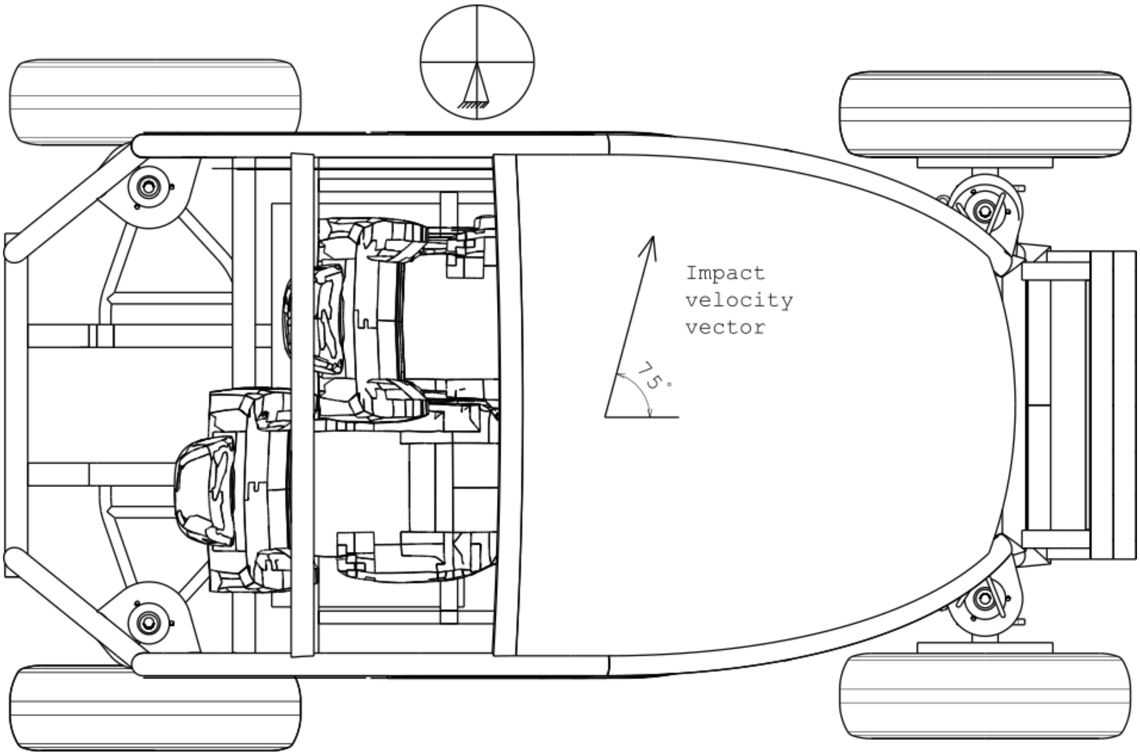

Source: from author.

Figure 20 – World SID anthropomorphic test device. On the left the physical dummy and on the right, the finite element model.

Source: HUMANETICS (2021).

4 M50-PS GHBMC MODEL

In this dissertation use was made of Global Human Body Model Consortium finite element model. This human body model (HBM) was developed through a consortium of the seven automakers presented in Table 9 specifically for car crash simulations.

Table 9 – Automakers members of the consortium.

Fiat Chrysler Automobiles (FCA)
General Motors Holdings LLC (GM)
Honda Co. Ltd. (HONDA)
Hyundai Motor Co. (Hyundai)
Nissan Motor Co., Ltd. (Nissan)
PSA Groupe (PSA)
Renault s.a.s. (Renault)

Source: GHBMC (2020)

The model was based on a 50th percentile male characteristics (UNTAROIU et al., 2017). To choose a person that fitted the dimensions specified on car crash safety regulations, 15 measurements of person's body were collected and if a standard deviation superior to 3% of the norm was found the subject was disregarded (GAYZIK et al., 2011). In the end a 26 year old, 175 cm and 78.6 kg person was chosen to be the basis of geometric data. A multimodality protocol was used to acquire the data in a pedestrian posture, Figure 21 (GAYZIK et al., 2011). External anthropometry was collected via a three-dimensional scanner. The scans and external anthropometry were joined together to the creation of non uniform rational basis splines (NURBS). With this information it was possible to model the subject in CAD format with 140 components. Model mesh, Figure 22, was obtained with the CAD model and with the already existent mesh of a vehicle occupant (seated - M50-O) .

Two models were generated: one complete (M50-P) with finite elements more discretized and with internal organs modeled and one simplified (M50-PS) with larger elements and internal organs represented by two "blocks" (one below the diaphragm and one above). In this dissertation the simplified model was utilized in the simulations.

The simplified model is intended to be used on the study of gross force, deflection response and kinematics of a Car to Pedestrian Collision (CPC). To build the model the bones were taken from M50-O and oriented to match CAD data. The head of M50-PS utilizes the same skull, face, scalp meshes and brain as M50-O. The cervical spine of M50-PS was modeled based the vertebral body geometry from M50-O. Abdominal organs were replaced by homogenized cavity filling structures. The other external organs were modeled

Figure 21 – Data sources for the development of the model: (a) acquisition of upright MRI scans and (b) surface topography and bony landmark acquisition.

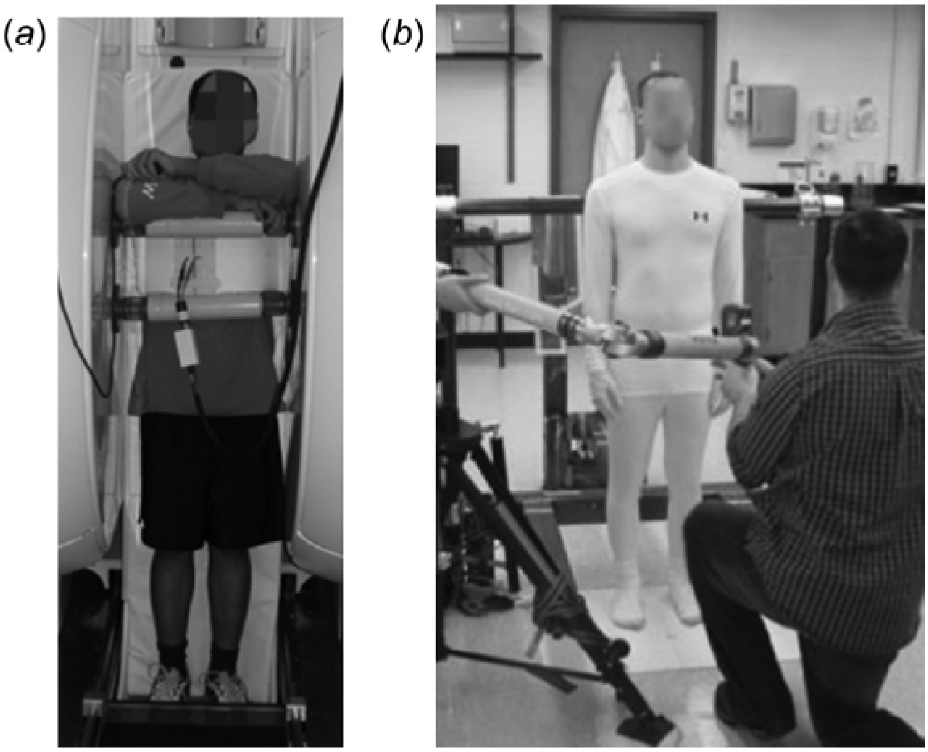

Source: Untaroiu et al. (2017).

primarily using hexahedral elements and tetrahedral elements on the parts containing an articulation.

4.1 Calibration and Validation of M50-PS finite element model

This section is based on Untaroiu et al. (2017).

4.1.1 Knee model under lateral bending impact loading

Knee joint is the most injured part of human body in a CPC, specially in lateral impact (TERESIŃSKI; MADRO, 2001). To calibrate biomechanical and injury of knee joint, a simulation was realized and the results were confronted with postmortem human surrogate[1] results already published (BOSE et al., 2008). In these numerical tests, the knees were kept intact and their ends were fixed in cylindrical cups. The cups were attached to two extension bars, which were mounted on supports through revolute joints. The distal support was fixed and the proximal support was allowed to slide in the longitudinal direction. The extension bars were loaded by an impact force at approximately 1 deg/ms knee angle, which corresponded to a 40 km/h CPC impact (UNTAROIU et al., 2004).

---

[1] From now on post mortem human surrogate will be called surrogate for simplicity.

Figure 22 – Final M50 simplified FEM model.

Source: from author.

4.1.2 Calibration of Lumbar Spine Under Bending Loading

The lumbar spine is very important in the responses of the model upper body in a CPC event. So the initial idea of modeling the bones as rigid body parts connected by joints could not be used and had to be improved with the inclusion of ligaments modeled as bars and the results obtained in the simulations were calibrated through surrogate available data from literature (ROHLMANN et al., 2002). In the testing, all degrees of freedom of lumbar spine L5 were constrained and on L1 a 7.5 Nm load relative to L5 was applied in extension, flexion and lateral bending.

4.1.3 Validation of the Pedestrian Model Under Pelvic, Abdomen, Thoracic and Shoulder Lateral Impact Loading.

The whole body model was calibrated for lateral impact at the pelvis, abdomen, and thorax regions. Simulation results were compared to existing surrogate data available on Viano (1989). In the tests, a 23.4 kg pendulum was released to strike fourteen cadavers with velocities of approximately 4.5, 6.7 and 9.4 m/s. In the surrogate tests, the force was

Figure 23 – Knee bending moment test setup.

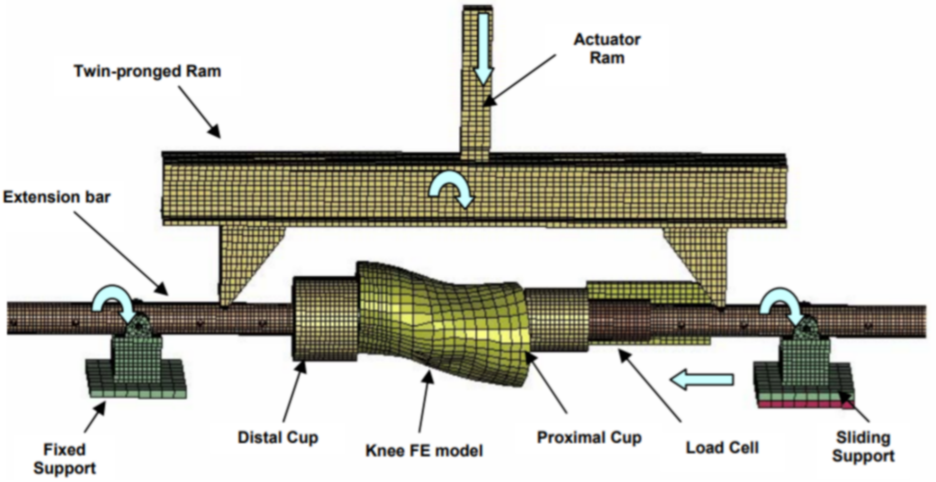

Source: Untaroiu et al. (2004).

Figure 24 – FE setup of the spine calibration. (a) Undeformed (b) extension (c) flexion (d) lateral bending.

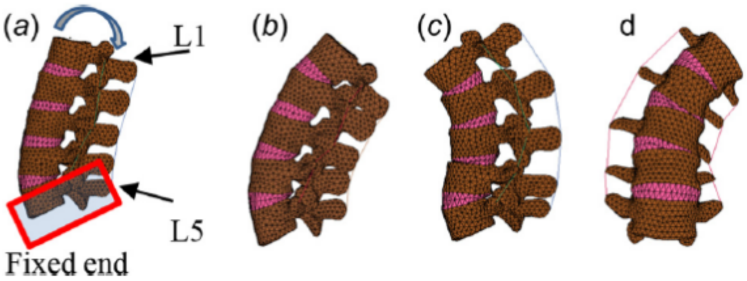

Source: Untaroiu et al. (2017).

calculated based on the time history deceleration of a pendulum mass. In the human body model calibration simulation via rigid impactor was used to perform the same tests as those performed in the surrogate, Figure 25.

4.1.4 Calibration of the model in a car to pedestrian collision

This study was based on tests performed with a surrogate presented in Kerrigan, Crandall and Deng (2007). In the study, 7 cadavers were positioned laterally in relation to the car and lifted to remain in standing position. About 20-30 ms before the impact the surrogate was released from the lift and the accelerations during the impact were measured. In the simulation, gravity was considered to be applied on the model and a 800N load was applied from the soil in the model feet, Figure 26.

Figure 25 – The FE setup of (a) pelvic, (b) thoracic, (c) abdomen, and (d) shoulder lateral loading.

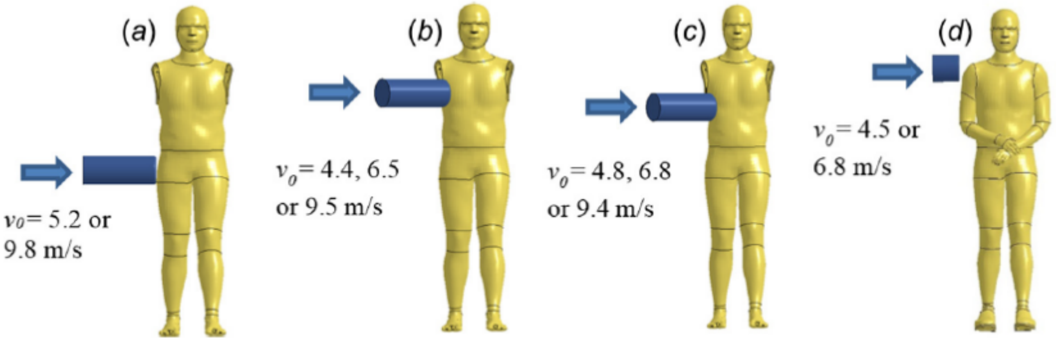

Source: Untaroiu et al. (2017).

Figure 26 – Calibration of model in a CPC.

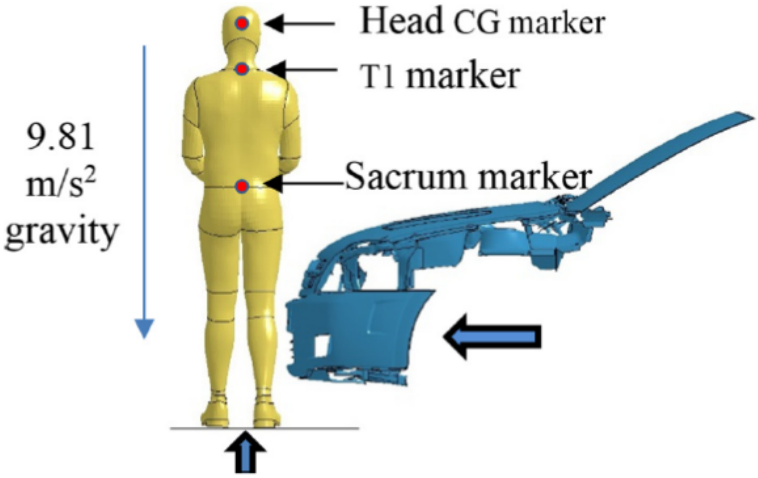

Source: Untaroiu et al. (2017).

4.2 Results of calibration

4.2.1 Component level

Knee bending moment results of the simulation were similar to the responses observed on surrogate, Figure 27. Lower values in the simulation may be observed in the results but this may be due to the differences in the inertia in the beginning of the simulation.

In the lumbar spine, calibrated tests extension and lateral bending were within surrogate ranges with flexion resulting in slightly lower values, Figure 28.

In both thorax and abdomen, Figures 29 and 30, the results were within the error margins, reaching the upper margin in the beginning of the simulation and reaching its lower margin in the end.

Figure 27 – Knee bending moment results.

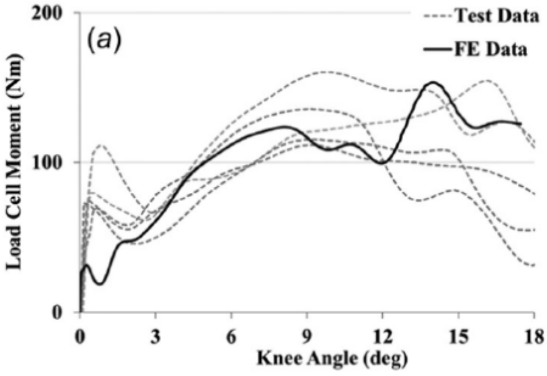

Source: Untaroiu et al. (2017).

Figure 28 – Lumbar spine calibration results.

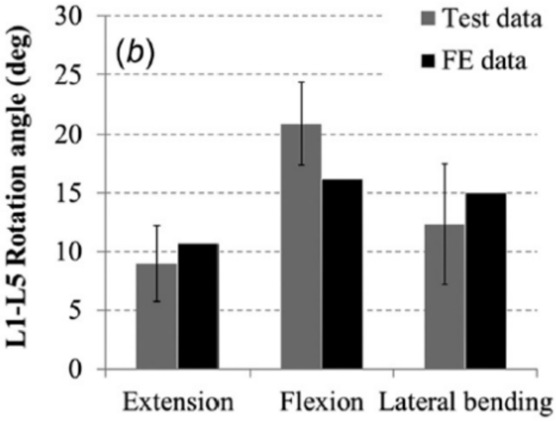

Source: Untaroiu et al. (2017).

4.2.2 Validation of the model in a Car to Pedestrian Collision

A visual comparison was made between the simulated model and results from the surrogate, Figure 31 (KERRIGAN; CRANDALL; DENG, 2007). When comparing the injury prediction, medial collateral ligament (MCL) and anterior collateral ligament (ACL) ruptures were observed in the first impacted model knee (the right one) and on the left knee it was observed rupture of Lateral collateral ligament (LCL) and ACL and the same pattern was observed in the surrogate tests.

4.2.3 Final considerations about the model

The model presented good results when compared to the surrogate results available in literature, demonstrating that it is a good replacement to the dummy impactors used today on the crash test regulations. Some differences were observed but surrogate have different mass distribution and the exact test conditions are difficult to be represented in a simulation. This model is a great advance and will help in the design of safer vehicles.

Figure 29 – Abdomen calibration results.

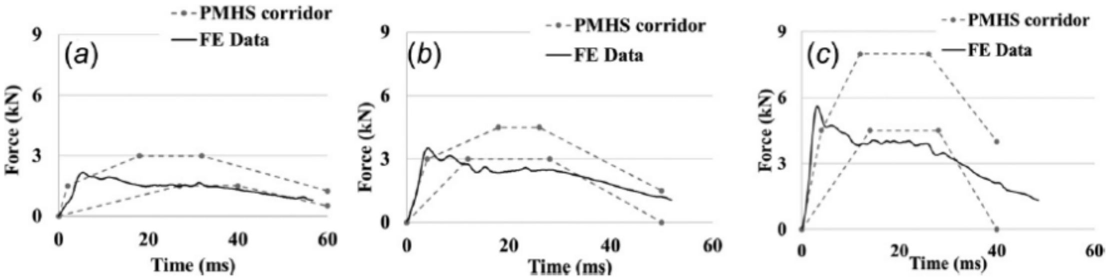

Source: Untaroiu et al. (2017).

Figure 30 – Thorax calibration results.

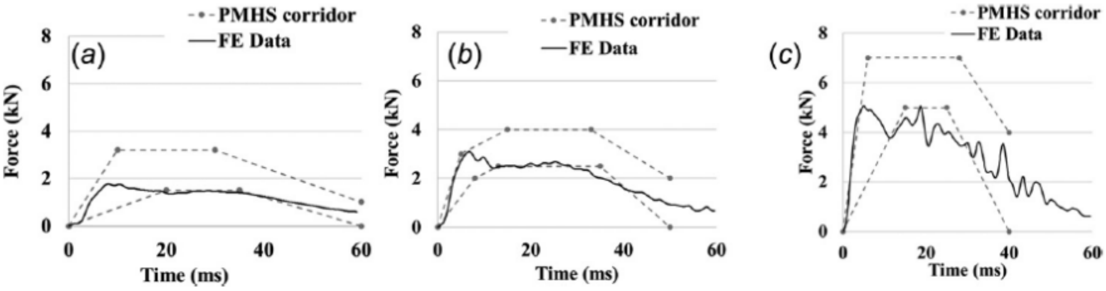

Source: Untaroiu et al. (2017).

Figure 31 – Comparison of a surrogate running over and a CPC FE simulation.

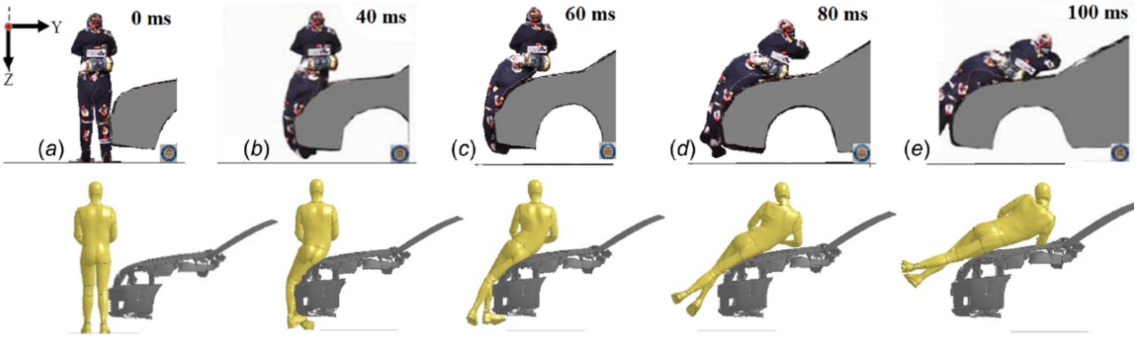

Source: Untaroiu et al. (2017).

5 RESULTS

5.1 Protection of the occupants in the event of frontal collision - ECE R94

The first performed simulation was frontal crash test of the vehicle against a deformable barrier with 40% offset. In this simulation a dummy was positioned on driver seat and a 70 kg mass representing the passenger was positioned on the other seat. Figure 32 presents the screenshots of the simulation for various time steps.

Figure 32 – AUS first crash simulation against 40% offset deformable barrier.

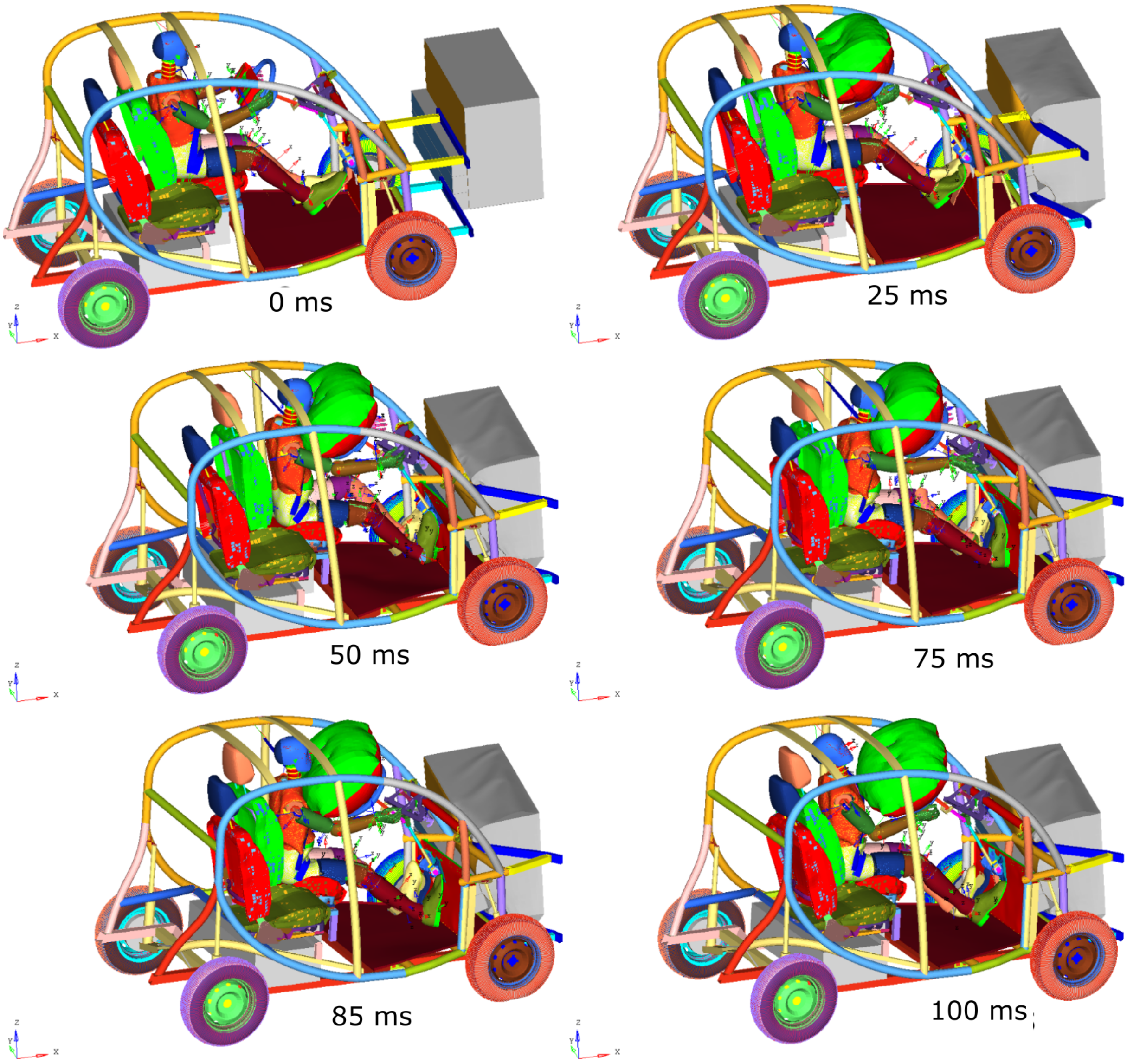

Source: from author.

In the first in all steel components were 1 mm thick. These thickness were changed based on the expected behavior of the vehicle and on the observed stress field. For example: with 1.0 mm the superior crash box presented a global bending behavior and not a progressive crushing. If on the other hand thickness was excessively reduced folding happened very quickly reducing the absorbed energy. So that thickness was reduced or increased based on simulation results. With the 1.0 mm it was possible to observe that the structure supporting the seats and the passengers were super sized, it presented very low tensions, so it could be reduced. This kind of analysis was performed for the whole vehicle during all the design phase.

The air bag had to suffer a few modifications in its dimensions during analysis. Some tests were performed based on dummy's head acceleration. The first air bag used was quite big and the dummy deceleration was too high. With the size reduction an acceptable deceleration was obtained and that size was used during the other simulations.

Other structures that suffered many design changes during the process were the crash boxes, both in size and shape. Many crash boxes were tested with different length sizes. Another thing that improved a lot the crushing behavior was little "imperfections" put on tubes to initiate the local bending process. Two imperfections were added on the tubes: one put on the beam end, where the crash would happen. This imperfection would start the crush. The other imperfection was placed in the beam middle. This would allow the crush to go all along the beam length, increasing the energy absorbed by the structure. These imperfections could be obtained on construction with a press. An example of the imperfection is presented on Figure 33 and an energy absorption evaluation is presented on section 6.2.

Figure 33 – Crash box folding initiators.

Source: From author.

Yamaguchi, Kato and Okazaki (1985) conducted empirical studies on the size, shape and pitch of the dent-type crush initiator in the front frame, which induced a bending collapse in the original design, to find ways to maximize the mean crushing load lead by an axial collapse. Kitagawa, Hagiwara and Tsuda (1991) et al. conducted numerical buckling analyses on how to increase the mean crushing load of an asymmetrically shaped front frame, by making the crush initiator on the concave and convex parts of the buckling wave to induce an axial collapse. Reid (1996b) and Reid (1996a) studied the trends of crash energy absorption according to material properties and thickness of the front rails. He was able to obtain an approximate formula that could predict the amount of crash energy absorbed for a given front rail based on the material's properties and thickness.

Cho et al. (2006) made several studies to evaluate the energy absorption of circular and rectangular dent-type imperfections to initiate crush behavior. The study concluded that rectangular dent type is the most effective and is commonly used in commercial vehicles. Because of this reason, the rectangular type was used on the model.

After these discussed vehicle modifications, the results were in accordance with the required by ECE R94. For instance, Figure 34 presents the acceleration of the center of gravity of the dummy's head. ECE R94 requires that this acceleration does not exceed 80 g for more than 3ms and the obtained values did not reach this limit at any time, making the vehicle ECE R94 compliant. Head acceleration is also used for the HIC calculation[1] (more details on section A.1).

Figure 34 – Head center of gravity acceleration.

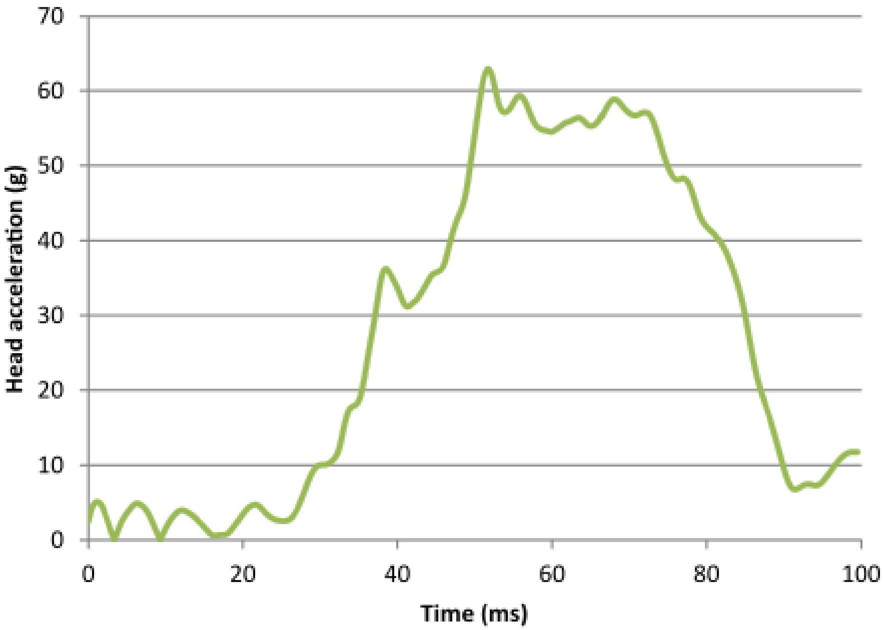

Source: From author.

---

[1] Head injury criteria has dimension of $[length]^{2.5}[time]^{-4}$ but is referenced generally without units, e.g. "HIC should be lower than 1000". The same representation is used in this dissertation.

Figures 35 and 36 present the obtained neck values of shear and axial forces and the criteria required by the regulation. In the figures it is possible to observe that the vehicle comply with the requirements.

Figure 35 – Axial tensile neck force.

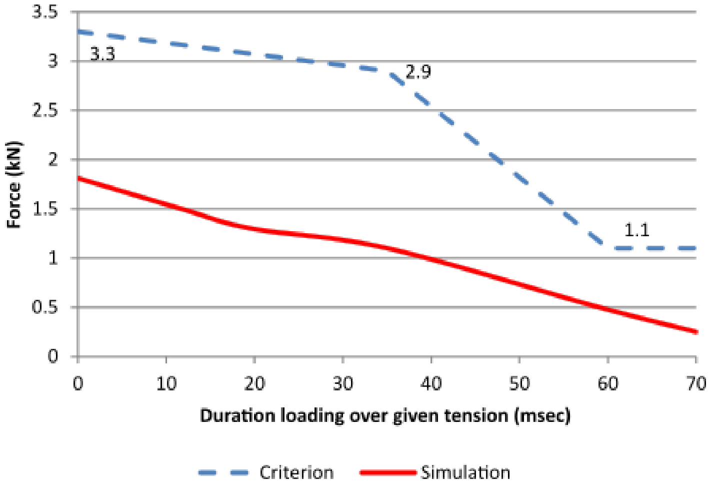

Source: from author.

Figure 36 – Neck shear force.

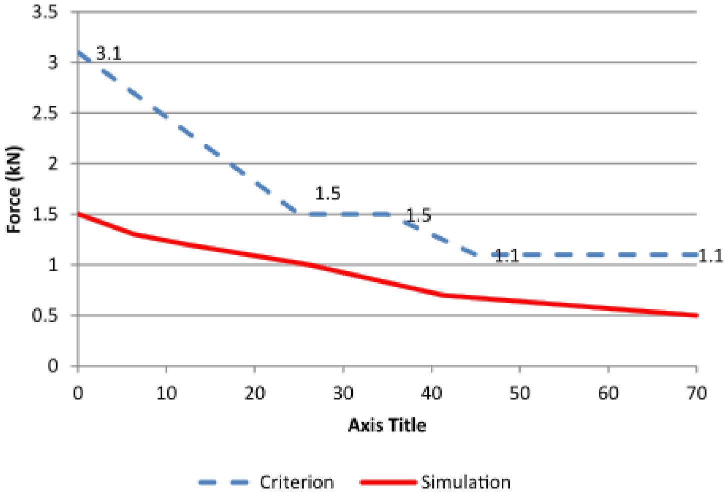

Source: from author.

Besides that, were all analyzed maximum femur force, maximum tibia force and the maximum thorax compression. The obtained values and the criteria required by the regulation are presented on Table 10.

The obtained results guarantee that the vehicle is able to comply with ECER94 requirements. Future works should evaluate the vehicle on other kinds of frontal crash

Table 10 – Results of the first simulation.

Criterion	Obtained	Acceptable
Maximum femur force	6.69kN	7.58kN
Maximum tibia force	4.33kN	8kN
Maximum thorax compression	42mm	42mm

Source: from author

test to check if it is still able to comply with a crash against a rigid barrier, crash a pole frontally, etc.

With the vehicle able to comply with ECE R94 it was possible to analyze the vehicle when colliding a pedestrian.

5.2 Car to pedestrian collision - ECE R127

Simulations were performed so to verify whether AUS is compliant with ECE R127. This regulation requires that a legform and a headform dummy be thrown against the vehicle and values of acceleration, bending angle and shearing displacements should be obtained and compared to the regulation.

As in this work it was possible to have access to a model that represents the whole human body, this model was used in the numerical simulations and in addition to that the traditional dummy models were also used and their results compared.

The plots of the simulation using the human body model are presented in Figure 37 and the plots of traditional dummies are presented in Figure 38.

Figure 37 – Pedestrian plots - 150ms simulation

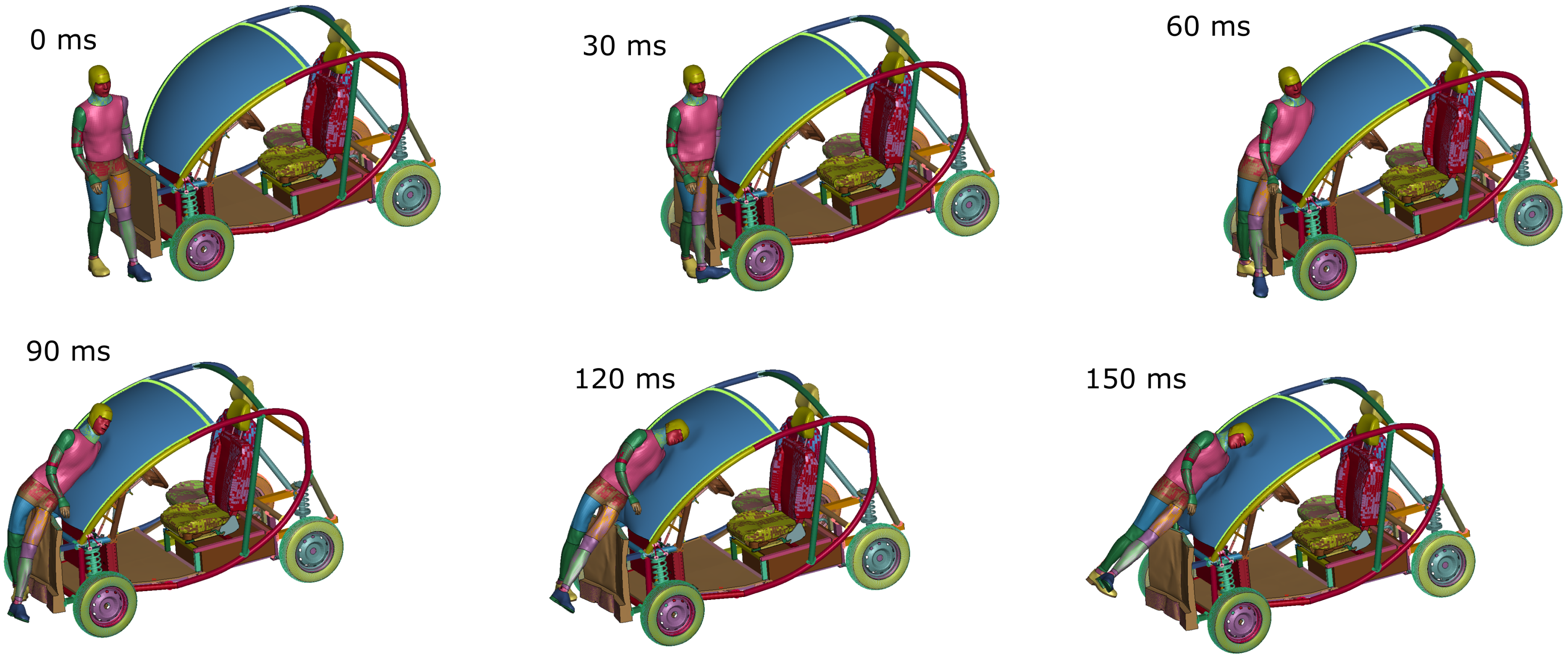

Source: from author.

Figure 38 – Legform impact simulation for 0, 20, 60 and 80ms.

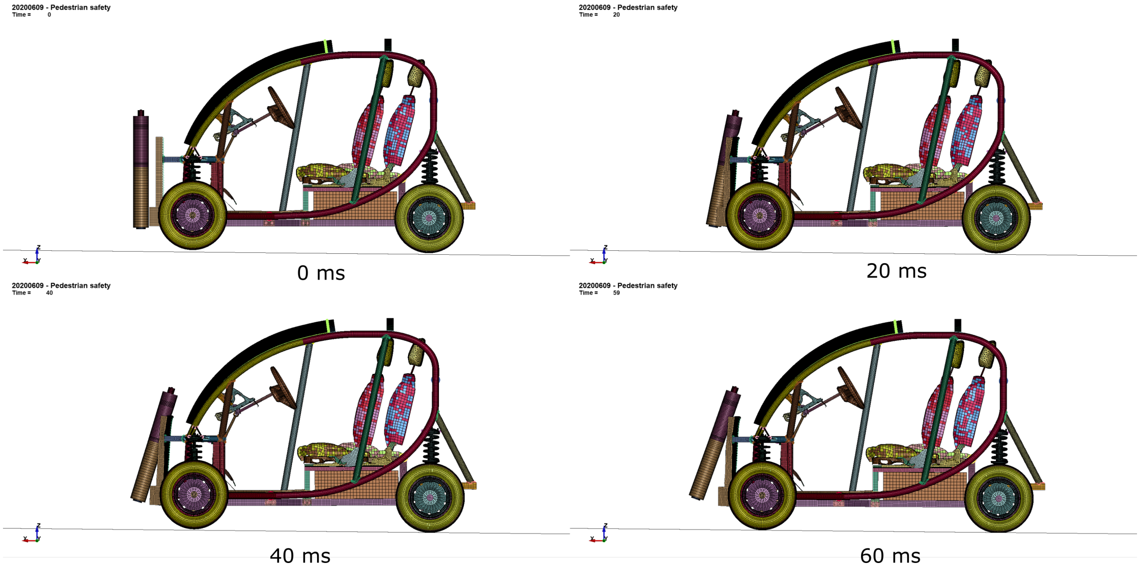

Source: From author.

The simulation of Figure 37 took approximately 50 hours to complete. The main modification made to the vehicle for the pedestrian regulation acceptance was the assembly of a honeycomb in the front of the vehicle. The honeycomb design is discussed in more detail in subsection 6.2.2.

The main focus of this regulation is on dummy's knees and head. The knees are evaluated considering the maximum bending angle, that should not exceed 19 degrees, maximum knee shearing displacement, that should not exceed 6.0 mm and maximum acceleration in the top of tibia, that should not exceed 170 g. The criteria adopted to the head in the regulation is the Head Injury Criteria for 15 ms (HIC_{15})[2].

The first result to be presented is the acceleration of top of tibia, Figure 39. It shows that the car design complies with the requirements of ECE R127, since the maximum tibia acceleration is inferior to 170 g. It is possible to observe that the accelerations of the human body model are considerably higher than the acceleration calculated in the dummy legform impactor.

This was the only result where the obtained dummy legform results curve can be shown together with the results obtained by the human body model. In the dynamic knee bending and in the maximum shearing displacement, the dummy results were almost zero during the entire simulation, so they will not be shown on next figures. With this observation it is possible to conclude that the regulation is much more restrictive if the human body model is used. Besides that, it is possible to access results that were not possible to be obtained using the legform impactor dummy. Since it is now possible to

---

[2] The HIC calculation is presented in the appendix, section A.1.

Figure 39 – Acceleration at the top of tibia.

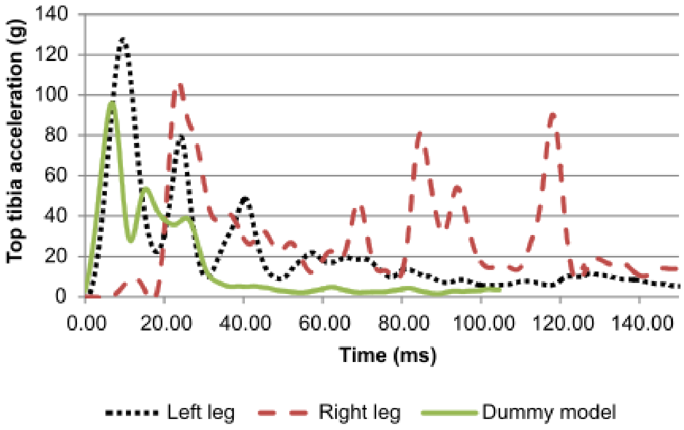

Source: from author.

use this kind of human model, regulations could be revised considering the use of more complete finite element models. These models are still under development stage due to their limited validation. However, with the increasing computational power, these models will soon be able to reproduce crash events with bio fidelity, reducing costs in the design of vehicles and allowing the discussion of different kinds of injuries (LALWALA et al., 2020).

Figure 40 presents the knee bending angle calculated in the simulation. As it can be seen in the figure, knee bending angle does not reach the maximum allowable value (19 degrees). The legform dynamic knee bending angle curve was not presented because the values were very close to zero in the whole simulation.

Figure 40 – Dynamic knee bending angle.

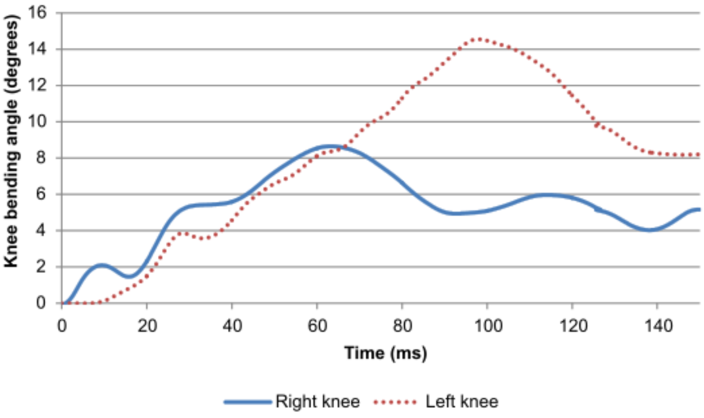

Source: from author.

Figure 41 presents the shearing displacement of the dummy's knee. Again, the values are inferior than the limit imposed by the regulation, which is 6 mm.

Figure 41 – Shearing displacement.

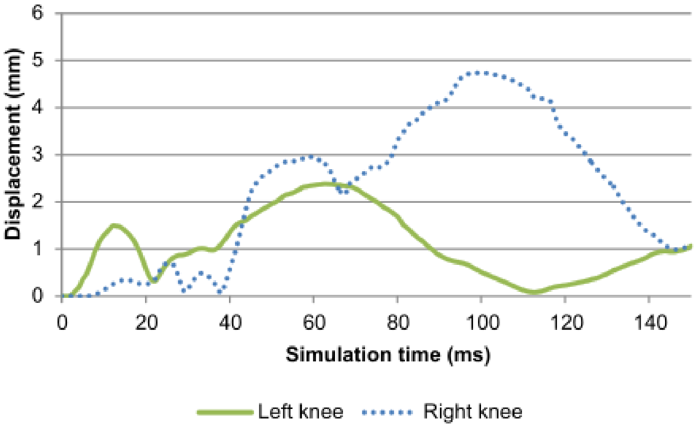

Source: from author.

Figure 42 presents the acceleration of the head center of gravity. The calculated HIC15 for the head accelerations was 509.1. The allowable value is 1000, so the model was approved in the HIC criteria.

Figure 42 – Pedestrian head acceleration and HIC15.

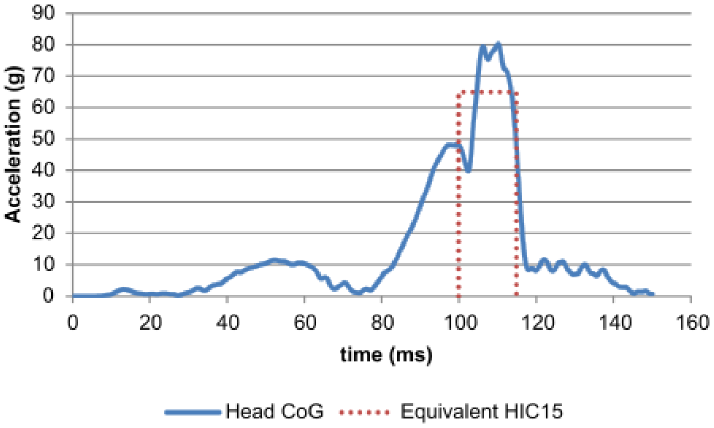

Source: from author.

With this analysis the model was able to be considered accepted in the pedestrian regulation. But as some modifications (as the inclusion of a honeycomb) were made in the model and the modifications may affect the frontal crash test, a new simulation was made to check if the model was still ECE R94 compliant.

5.3 CPC with masses simulating the vehicle occupants - ECE R127

To complement the previous analysis of the car to pedestrian collision, two masses of 75 kg were put in the vehicle seats. One goes at the driver and the other at the passenger center of gravities. With the inclusion of these concentrated masses the vehicle had its inertia increased and the motivation to do so was to evaluate if this would impact the pedestrian results.

The first criteria evaluated was the Tibia acceleration, Figure 43. As it could be observed the maximum calculated acceleration during the simulation was of 130g approximately, which is similar to the values calculated in the analysis without the masses representing the passengers.

Figure 43 – Tibia acceleration.

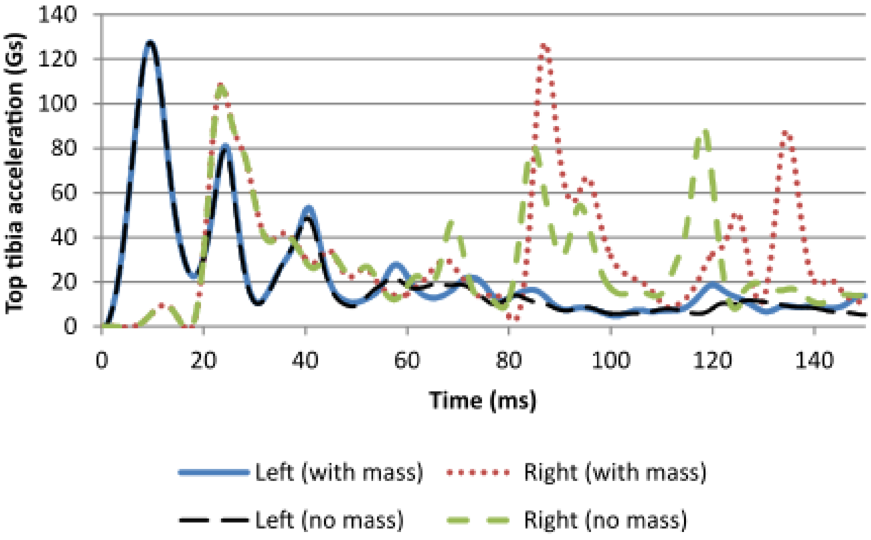

Source: from author.

The values are still in accordance to the regulation requirements, which is 170 g but the right knee present a peak superior to the peak observed previously at the simulation time of 90 ms. In the first half of the simulation the human body model behavior was similar the previous evaluation but in the second half of the simulation the calculated values are higher.

The anterior right knee acceleration value in 90 ms was about 80 g and in this analysis the acceleration was higher, reaching 120 g. This is probably because, with the two occupants, the vehicle inertia was considerably increased since its structure did not reach 500 kg and increasing its mass with additional 150 kg resulted in an inferior car deceleration. The result was a more harmful crash.

The next calculated criteria was the knee shearing, Figure 44. The maximum knee shearing occurred with the right knee and the calculated value was of approximately 5mm, witch is inferior to the value imposed by the regulation.

Then it was analyzed the dynamic knee bending angle. As it can be observed in Figure 45, the calculated value is still inferior to the limit of 19 degrees.

Figure 44 – Knee shearing displacement.

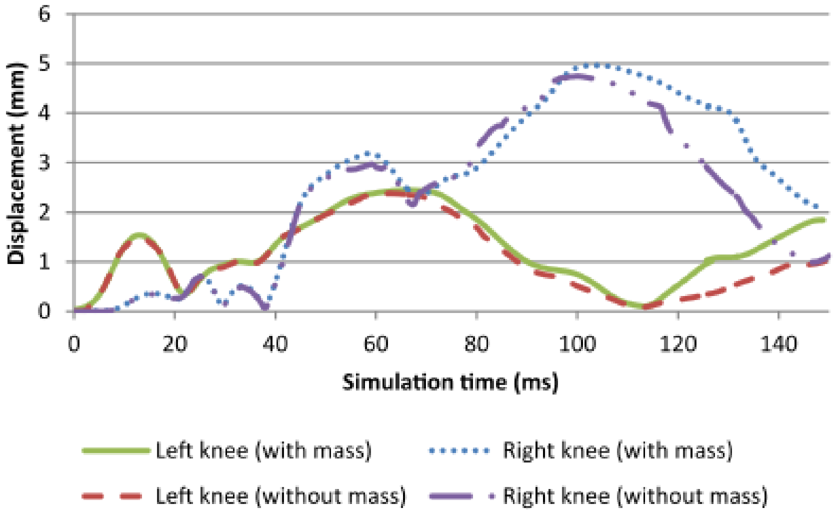

Source: from author.

Figure 45 – Dynamic bending.

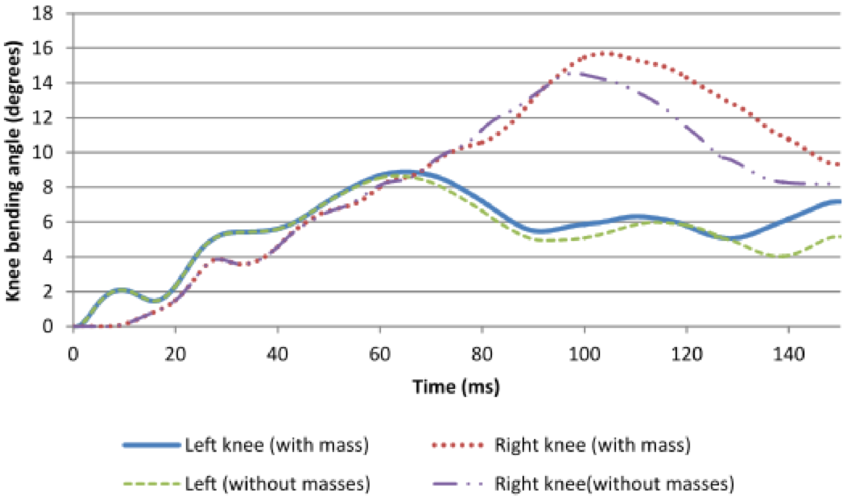

Source: from author.

The head injury criteria for 15 ms should not be superior to 1000. The head center of gravity acceleration is depicted in Figure 46. The maximum acceleration exceeded 80 g in instants of time close to 90 ms, and this didn't occurred in the previous simulation. This indicates that the head impact was more severe and this behavior had been observed previously, on Figure 43. But despite this increase in the head acceleration, the calculated HIC was 703, which is higher than the the 509 calculated previously but is still in accordance with the requirements of the regulation.

The vehicle was able to comply with the regulation in the simulation with point masses simulating the vehicle occupants. But with the increase in the vehicle inertial its

Figure 46 – Pedestrian head acceleration and equivalent HIC15.

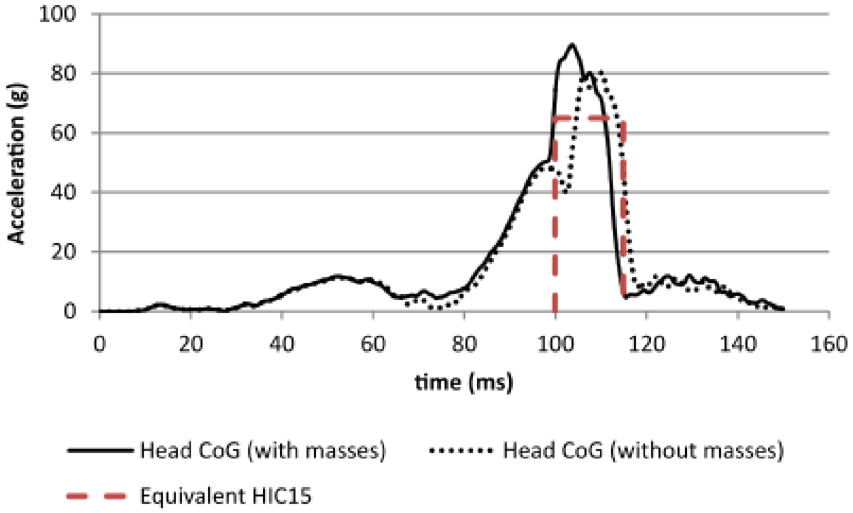

Source: from author.

deceleration happened slowly resulting in a more harmful impact in the period of time close to 90 ms.

5.4 Frontal crash test with the modifications proposed to comply with ECE R127: Crash beams and honeycomb support structure

The same test performed previously with AUS colliding against a 40% offset deformable barrier was now performed using the model defined in Section 5.2. The vehicle in perspective is presented in Figure 47.

Both driver and passenger were verified but only the driver results will be presented since its values were always superior to the values calculated to the passenger. This happens because the impact occurs at the driver side and its deceleration is more significant than the deceleration experienced by the passenger.

The first criterion evaluated was the HIC_{36} and head acceleration. HIC_{36} should not exceed 1000 and the head acceleration should not exceed 80g for more than 3ms. The calculated values for the acceleration are presented in Figure 48

The presented plot shows that the head acceleration was superior to 80 g from 49.7 to 51.5 ms. This difference is equal to 1.8ms. So the 3 ms criterion was accomplished. The HIC36 calculated was 981, which is inferior to the 1000 required by the regulation. Therefore, the model passes the ECE R94 requirements for the head criteria.

With the head criteria in accordance to the required by the regulation it was evaluated the neck criteria.

Figure 47 – AUS model colliding with ODB40% with two occupants.

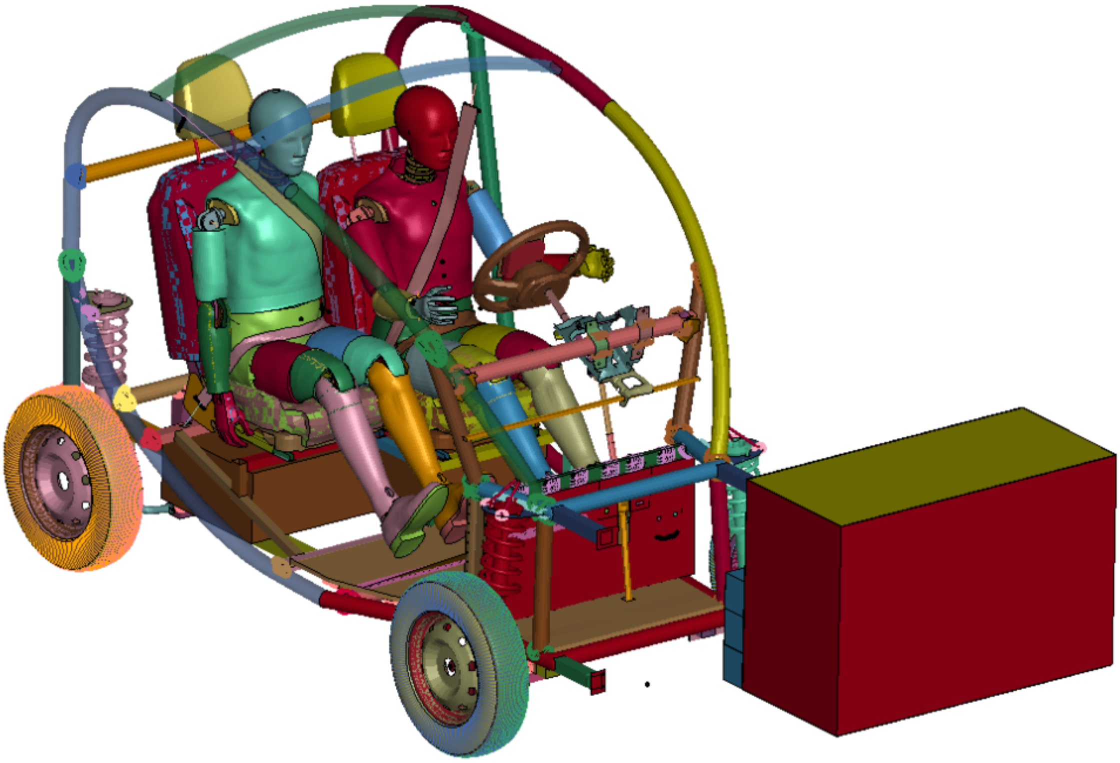

Source: from author.

Figure 48 – Driver head acceleration and equivalent HIC.

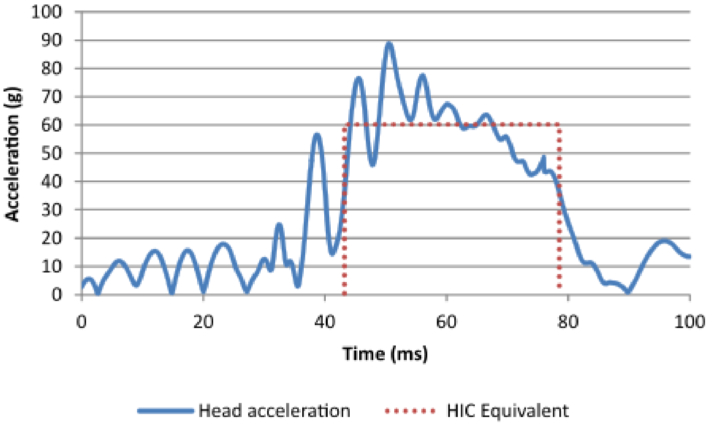

Source: from author.

Figure 49 – Neck shear forces.

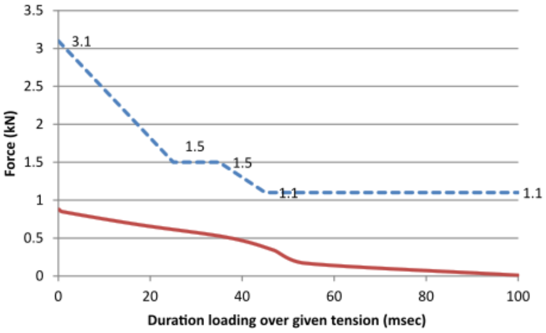

Figure 50 – Neck tensile forces.

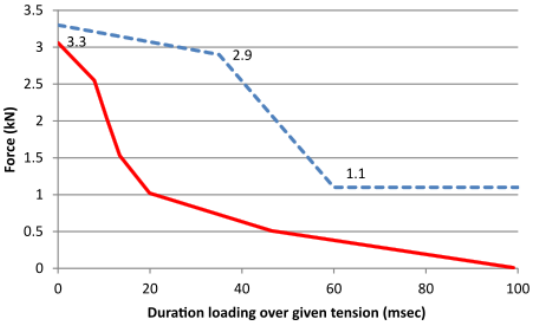

Figures 49 and 50 present the calculated forces in the driver neck in the continuous line. In the dashed one are presented the limits established by ECE R94. It is possible to observe that the forces always met the regulation limits.

The other evaluated criterion that are required by the ECE R94 are presented in Table 11.

Table 11 – Summary of results.

Criterion	Norm value	Calculated value	Compliance
Neck bending moment about y axis	Not to exceed 57Nm	51Nm	Ok
Thorax compression criteria	Not to exceed 42mm	41 mm	Ok
Femur force	Not to exceed 7.58 kN	2.1 kN	Ok
Tibia compression force	Not to exceed 8kN	5.6 kN	Ok
Tibia index	Not to exceed 1.3	0.891	Ok
Movement of sliding knee joints	Not to exceed 15mm	7.2 mm	Ok

Source: From author.

5.5 Pole Side Impact performance - ECE R135

To finish the main simulations required for a car crash test a the pole side impact was performed (UNECE, 2016). In this simulation, the vehicle should impact a rigid pole in a lateral collision and the pole should be alligned with the center of gravity of the dummy's head, as in Figure 19.

The dummy used for this simulation was the World Harmonized Side Impact Dummy (WorldSID), Figure 51 (UMALE et al., 2018). The speed that the vehicle should impact the pole for cars less than 1.5m wide should be 26km/h at 75 degrees (Figure 19). According to the regulation, the impact should occur at the driver side of the vehicle. This is the worst scenario for AUS because the B column is very close to driver, influencing directly the results.

To comply with the requirements imposed by the regulation, AUS had to have the doors implemented. At the driver side there is a main door to allow the driver to enter the vehicle and a second door to allow the user to accommodate small luggage and shopping. By the passenger side only one door exists to allow vehicle entrance. The rear plate was welded in the vehicle structure. Besides that, reinforcements had to be added to absorb energy on the lateral collision, Figure 52. It was also made a thickness analysis to obtain a door and a B column able to comply with the regulation constraints. Two examples of the structures with different plate thicknesses are presented in Figure 53.

Prior to the lateral crash test simulation only the tubular structure was designed. The doors and the B pillar were designed during this project step.

Figure 51 – WSID dummy. More details on Table 4.

Source: from author.

The graphic results of the simulation complying with the requirements are presented in Figure 54.

For this analysis it was evaluated the HIC_{36}. It should not be higher than 1000. In the simulation presented in Figure 54 the HIC was calculated to 659.9, which is below the threshold value of 1000.

It was also evaluated the peak force at the dummy's shoulder. This value should not be superior to 3kN. The calculated value was 2.3 kN, so, complying with the regulation requirements. The dummy's shoulder load cells are presented in Figure 55.

The third evaluated criteria was Thorax rib deflection. None of the thorax ribs should deflect more than 55 mm. The calculated values were 44 mm, 29 mm and 18 mm for the ribs. So, these values were in accordance with the regulation requirements.

The fourth criteria is related to the abdominal rib deflections. None of its ribs should deflect more than 65 mm. The calculated values were 16 mm and 25 mm, again in accordance with the regulation requirement.

The fifth criteria takes in account the lower spine acceleration, that should not exceed 75 g, except for intervals whose cumulative duration is no more than 3 ms. As this criteria involves time and the 75g threshold was trespassed the results were ploted and are presented in Figure 56.

As it can be seen in Figure 56, the acceleration of the lower spine was superior to

Figure 52 – Door details.

Source: from author.

75g during the interval [40.8 ms, 42.1 ms]. This interval corresponds to 1.34 ms which is inferior to the 3 ms tolerated by the the regulation. So the model complies with this criteria too.

The last criteria evaluated in the regulation is the pubic shymphysis peak force. This value is calculated through the dummy's element presented in Figure 57.

The limit defined by the regulation is 3.36 kN and the calculated value was 3.17 kN, which is complying with the requirement.

Although LSTC provides the dummies for free to users of LS-Dyna, this dummy was particularly outdated when compared to the current commercial version. The brand new model is in its 7.1 version, while the freely available one is on its 1.1 beta version. Updating the model would result in more trustworthy results and it would probably be easier to obtain the data from the simulation, since none of the results presented in this section were by default implemented in the dummy.

Figure 53 – AUS lateral collision plots at 46 ms. (a) presents the first analysis without thickness analysis nad (b) presents the simulation after thickness modifications.

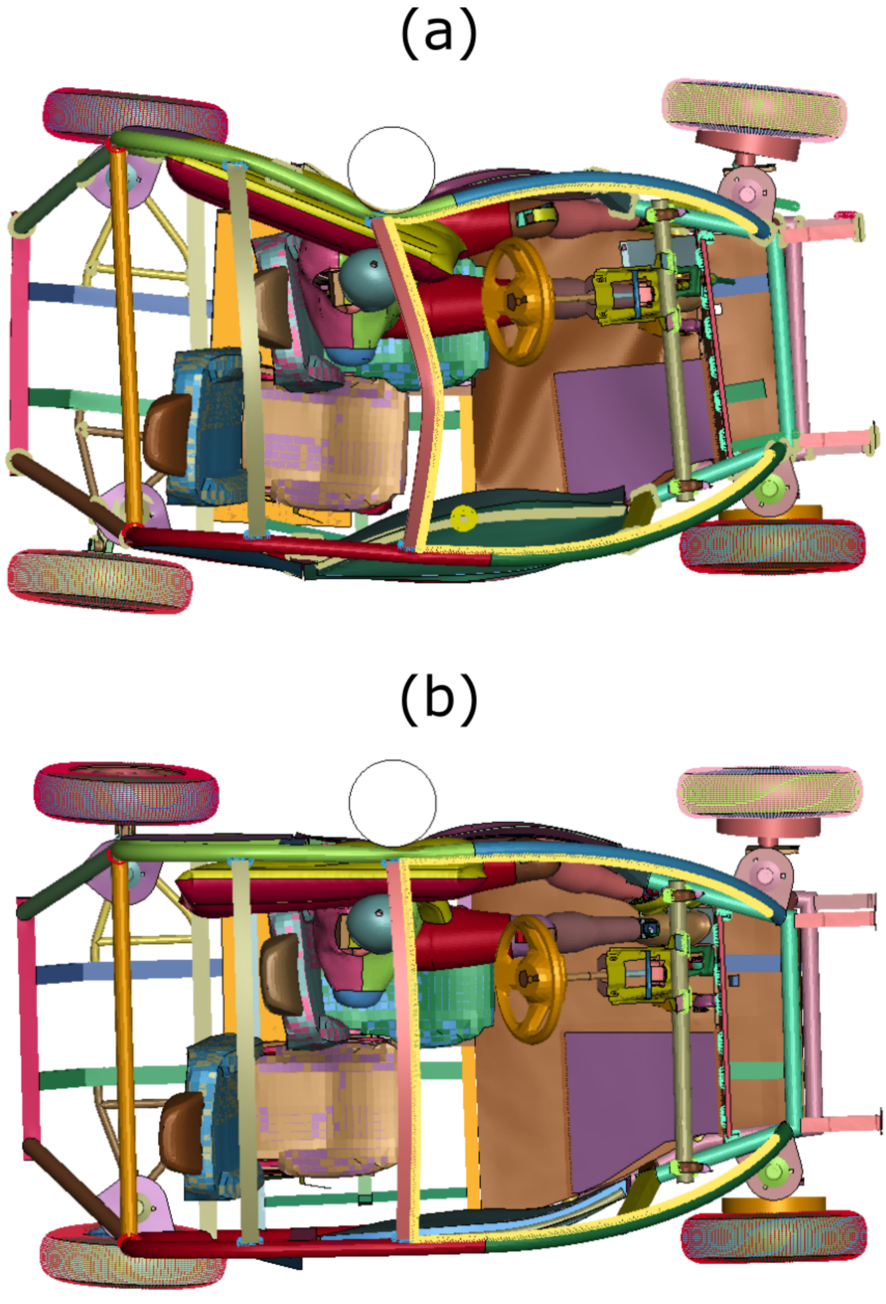

Source: from author.

Figure 54 – Pole side impact simulation from 0 to 75 ms.

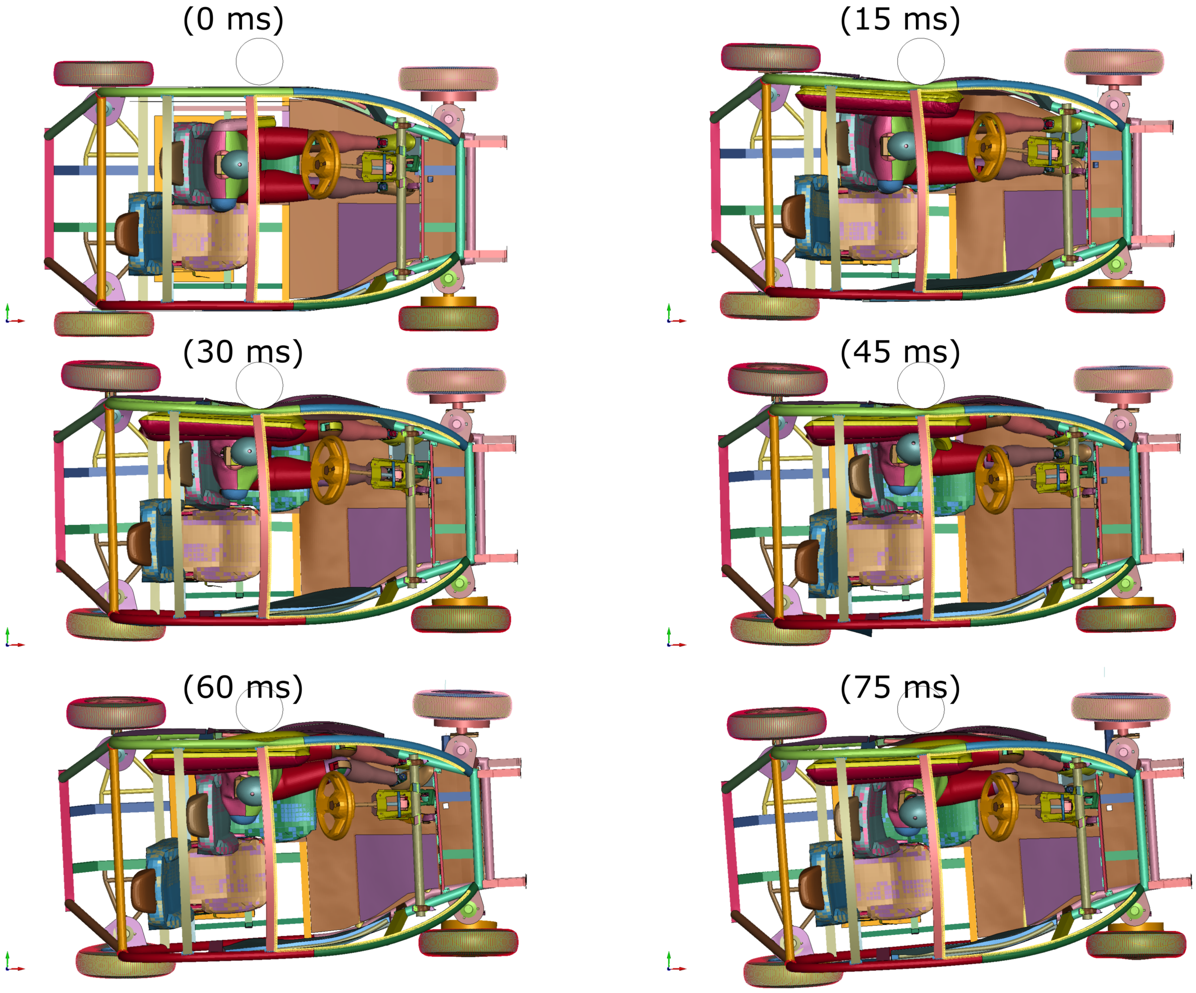

(0 ms)

(15 ms)

(30 ms)

(45 ms)

(60 ms)

(75 ms)

Source: from author.

Figure 55 – Dummy shoulder load cells.

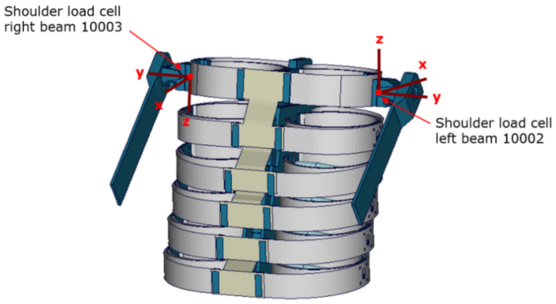

Source: Stahlschmidt, Huang and Schif (2020).

Figure 56 – Lower spine acceleration.

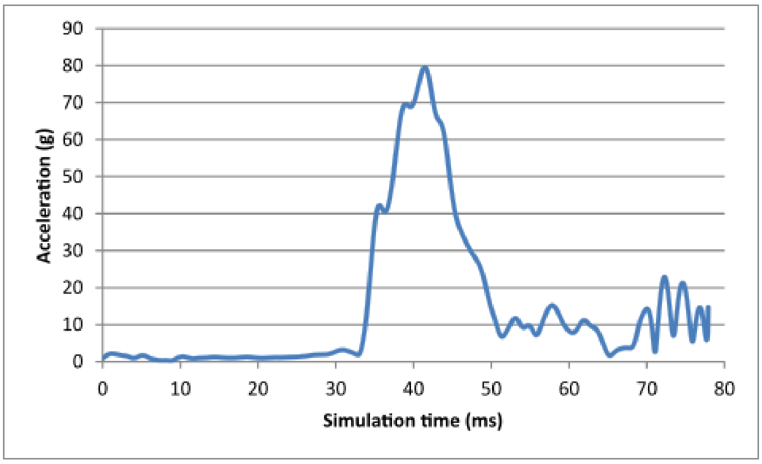

Source: from author.

Figure 57 – Pubic symphysis load cell.

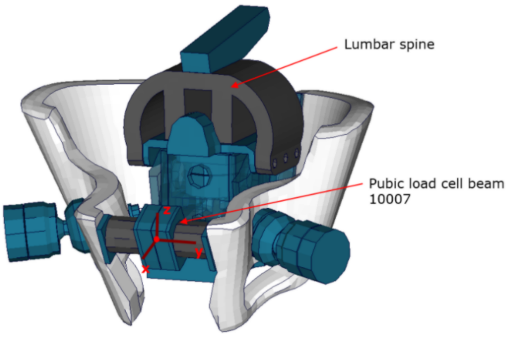

Source: Stahlschmidt, Huang and Schif (2020).

6 DISCUSSION

6.1 Dummy stability

During the initial phase of this car crash analysis LSTC version of dummy models for of LS-Dyna were used (LSTC, 2020a). The web site provides the 50th percentile Hybrid III, offset deformable barriers and other models commonly used in FE car crash simulations. Although they can be obtained without additional costs, they are known as not to be as stable as commercial dummies and models (LIN et al., 2014).

In the first simulations frontal crash tests were performed using a rigid barrier and 50th percentile Hybrid III dummy occupying driver seat. The simulation constantly was stopped due to negative volume in dummy´s foot. Lin et al. (2014) provides best practices to work with the dummy and to try to avoid those issues. They are presented below:

6.1.1 Null shell for contact

The shoe´s heel frequently stopped the simulation due to negative volume error. This occurs because the contact force between heel and floor may be too weak , which makes the foot nodes to penetrate the vehicle. Lin et al. (2014) suggests to increase the null shell thickness and Young´s modulus to correct that, as presented in Figure 58. The null shell is an element used in the boundaries of solid bodies in finite elements. These elements no not present mass nor interfere on the model rigidity. Their use is intended to improve the contact algorithms and reduce the simulation time.

Figure 58 – Increased null shell thickness and Young´s modulus.

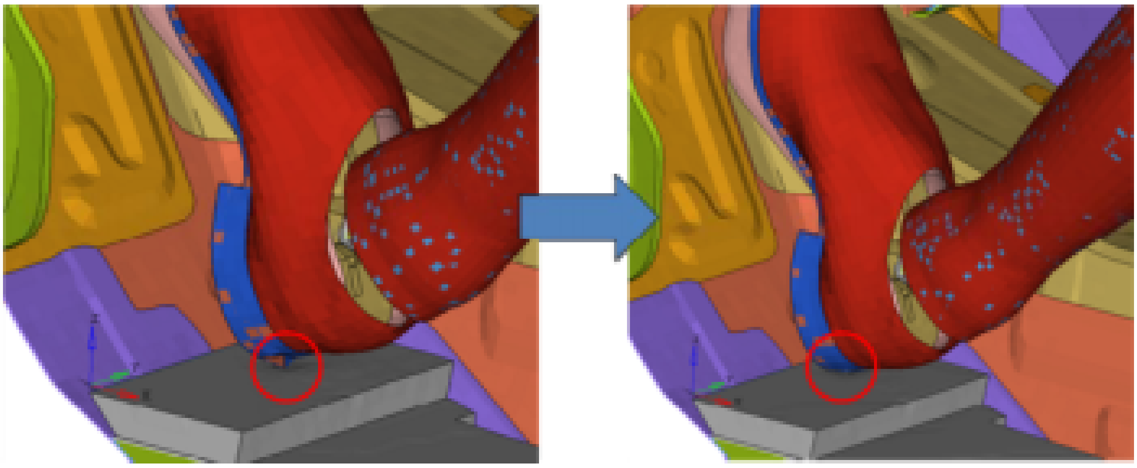

Source: Lin et al. (2014).

Although this did not solve completely the problem, in some simulations this problem did not occur and the analysis could be performed

6.2 Crash box

The first crash box designed to be used in the project was made thinking in the visual part of the project. For this reason its length did not advance beyond the length of the wheel, as in Figure 59.

Figure 59 – AUS with first crash box.

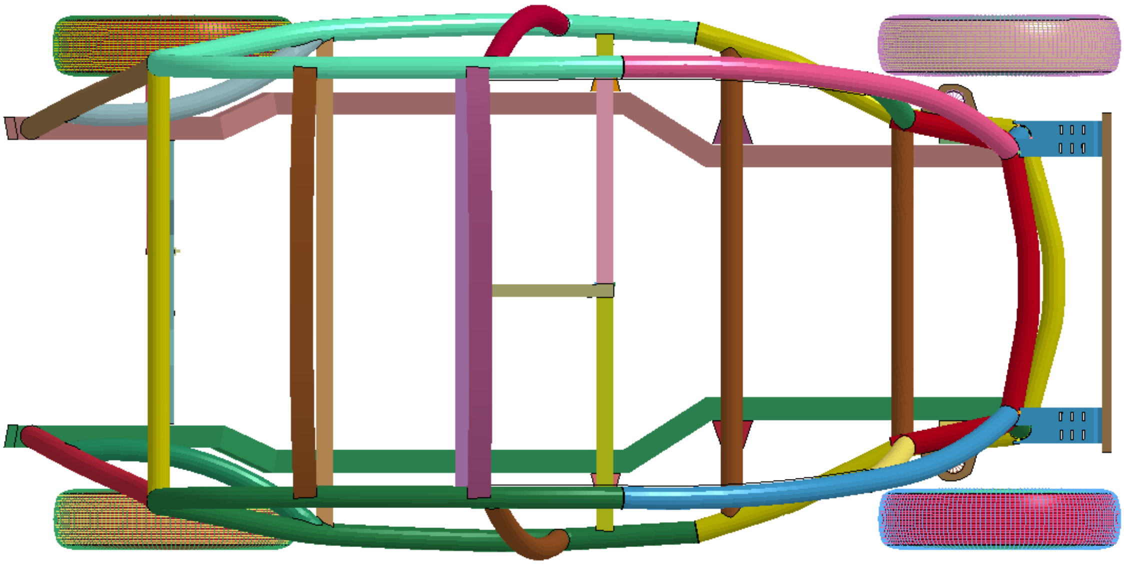

Source: from author.

It was observed that the energy absorption was not very effective in this first model, primarily because the wheels were impacting the barrier prior than the crash boxes and, by being elastic, were not absorbing energy permanently. Also, because of the small length of the tubes, little amount of energy was absorbed during the progressive buckling [1].

An alternate crash box was developed, Figure 60. This one passed the wheel limit, being the first part of the vehicle to have contact with the barrier, as it should be.

This frontal beam was about 130mm longer than the previous one and, to check its efficiency, a numerical analysis concerning the absorbed energy was performed, Figure 61. In the analysis a 1 ton weight was released against the tubes with an initial velocity of 2 m/s. The forces and displacements experienced by the body are plotted in Figure 62. An increase of 130mm in the crash box length increased the absorbed energy by 10kJ in a 40% width frontal impact.

---

[1] At this point of the analysis the vehicle was not completely designed and the B column and suspension system were not evaluated.

Figure 60 – AUS with second crash box.

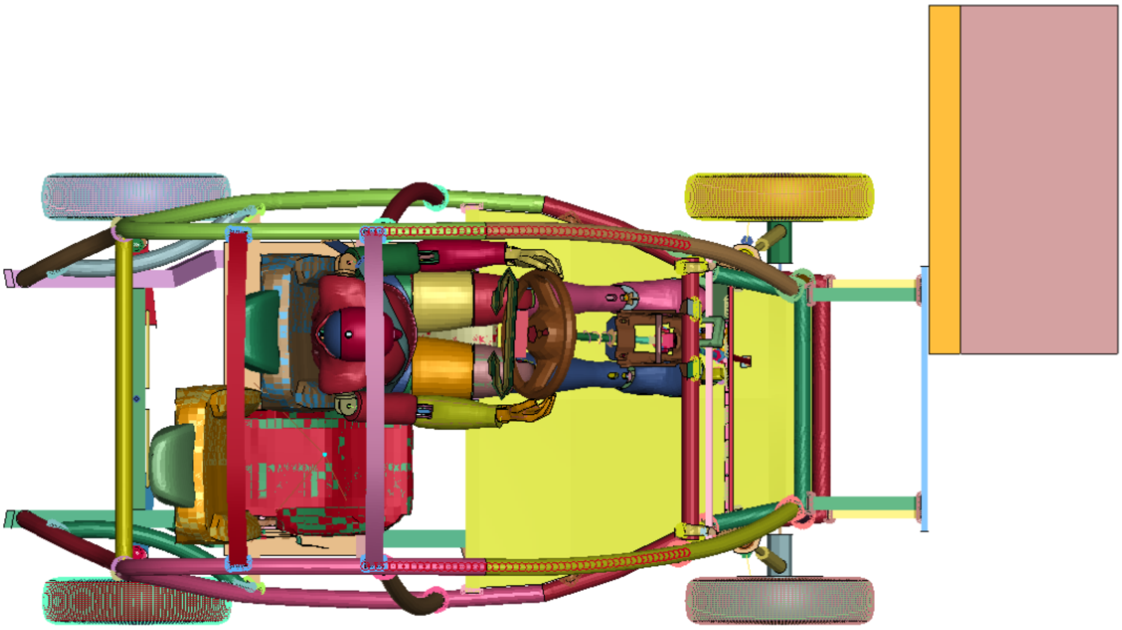

Source: from author.

6.2.1 Crashbox impact against pedestrian

The first trial in the car to pedestrian collision (CPC) was using the crash box approved in the first frontal crash test, Figure 63. Although this crash box presented good results in the frontal crash test, it was not appropriated to be used in a pedestrian friendly vehicle.

Since two beams were responsible to transfer all loads of the vehicle to the pedestrian, his legs were not capable to handle the impact and they would be injured in an unacceptable way. The two beams that impacted the pedestrian were too thin acting as a stress concentrator. Besides that the frontal crash test was modeled with steel DP1000, which is a advanced high strength steel. In the impact with the offset deformable barrier it performed well but in the impact with the human body model, its behavior was very stiff and had very low deformation. This is not good for energy absorption and the result was a broken leg, Figure 64.

Although the results were obviously not acceptable, it is worthy to analyze it. The impactor dummy, Figure 65, used in current regulations have a joint simulating the knee and foam above and below this articulation. It has quite a few sensors to measure forces and accelerations but it is not capable of predicting injuries, as bone breaking, as this human model predicted. Other injuries were found during the simulation that would not be obtained with current dummy models. It is possible to conclude that the advance in computational data processing and finite element human body models evolution may

Figure 61 – Simulation with the folding beam.

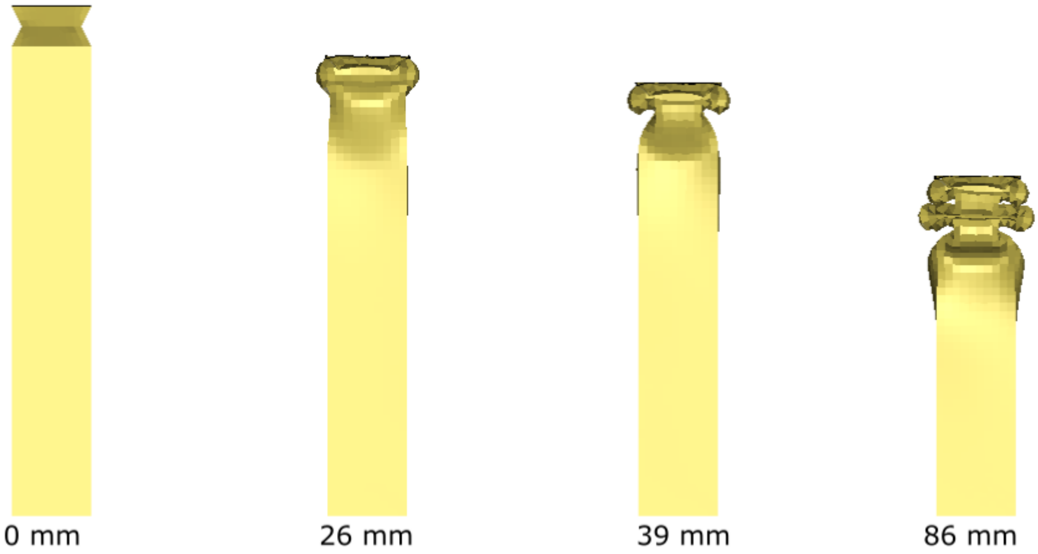

Source: from author.

Figure 62 – Force and absorbed energy during folding .

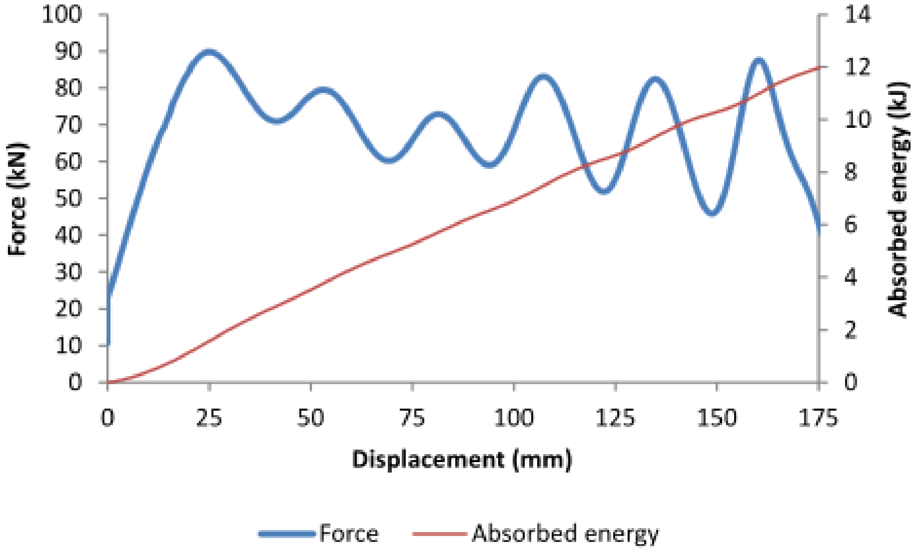

Source: from author.

increase safety in future vehicles with better predictions of injury and improvement in the capability of predict the kinematic interaction between a vehicle and a barrier or between a vehicle and a human being.

Figure 63 – Car to pedestrian collision with bar crashbox.

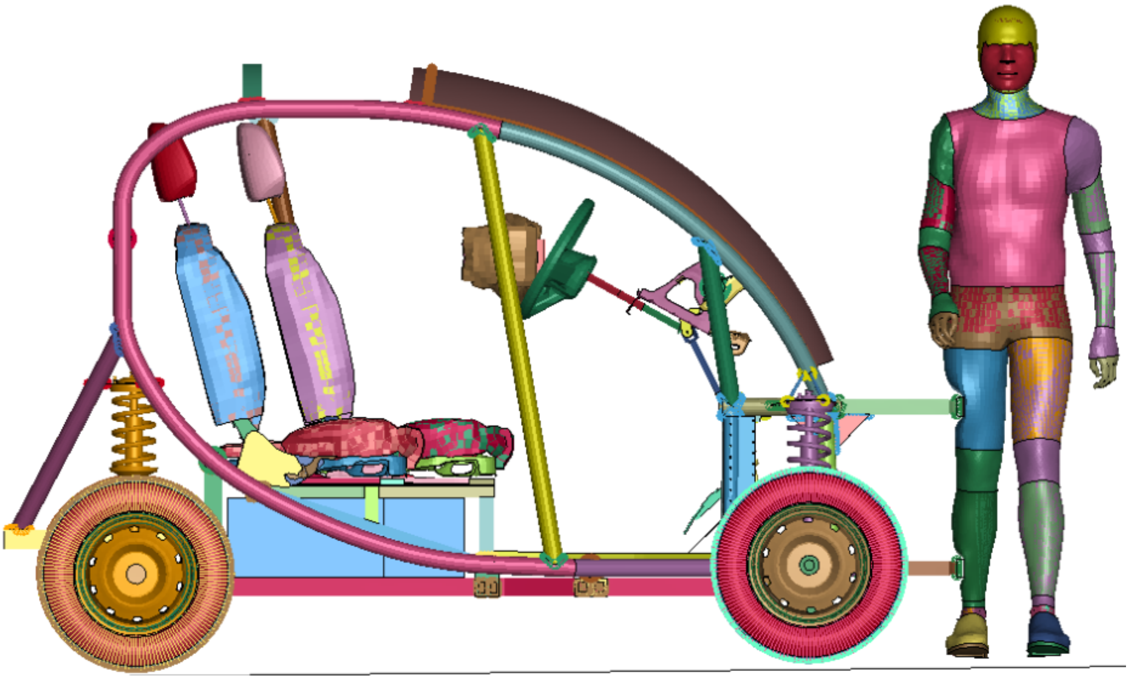

Source: from author.

6.2.2 Using a honeycomb model for crashbox

To solve the problem with the dummy broken leg a honeycomb crash box was developed in place of the beams. Honeycombs are very effective in absorbing energy and would not be as rigid as the steel beams.

The first trial was to fill the space between the two crash beams with an aluminium honeycomb. Honeycombs are commercially available and can be bought with different specifications of cell size, foil thicknesses and height. Substituting the steel beams for honeycomb resulted in better results. In the first test the leg bone did not break already.

But there are different honeycomb dimensions in the market and they were tested to check which one could cause less harm in the human model. The honeycomb with cell size 3/16” and foil thickness 0.00185” although did not break the model leg, caused a ligament rupture, Figure 66 (b). Other honeycombs were tested until this injury did not occur as presented in Figure 66 (a).

After different designs the following specification was used[2]:

- Cell size: 1/4´´

---

[2] Cell size, foil thickness and honeycomb thickness are given in inches, as announced by the supplier but were converted to millimeters in the simulation. Height and width are given in millimeters (ARGOSY, 2020), as the rest of AUS design .

Figure 64 – Pedestrian bone fracture.

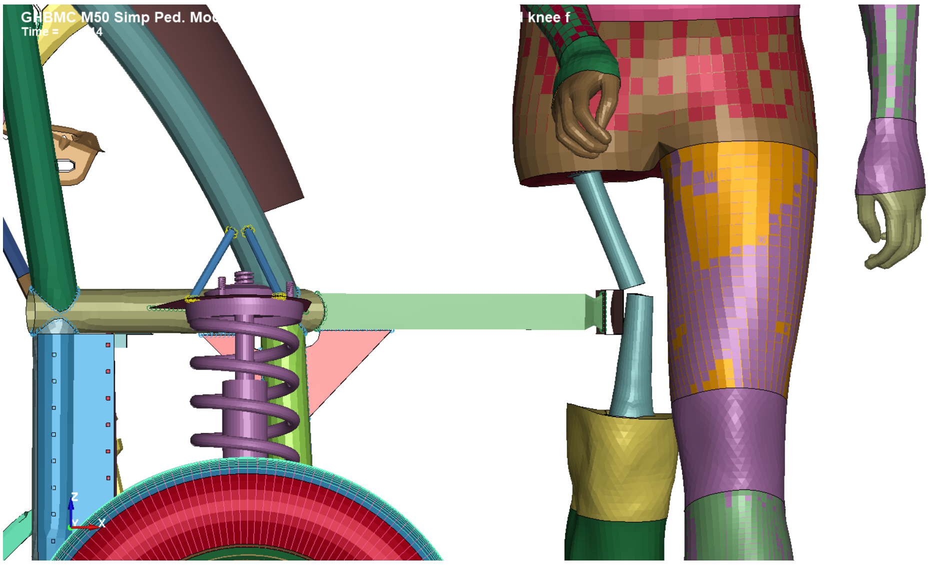

Source: from author.

- Foil thickness:0.00185´´
- Height: 427 mm

With this trial results were much better. Dummy bones did not break and ligaments were not ruptured, Figure 66.

6.2.3 Modeling crash box as surrogate elements

Modeling a honeycomb to be inserted ahead of the vehicle with shell elements presented a series of difficulties.

Since a honeycomb is made of many surfaces, a huge amount of finite elements were created, e.g., over 1 million elements, which impacts directly the simulation time. Another issue is the hourglass, a mesh instability (COOK; MALKUS; PLESHA, 2001). This happens due to approximation of the element strains in the Gauss integration points. As a first trial to solve this problem 6 and 8 node shells were used in the honeycomb but unfortunately hourglass insisted to be presented in the simulations.

Another trial was to reduce the length of the elements. This solved the hourglass problem but of course increased the quantity of finite elements and the computational time modeling the honeycomb as shell elements was impracticable.

To solve this problem it was decided to use the surrogate honeycombs instead of shell elements. One possibility is to use LS-Dyna's material *MAT_026, used for honeycombs (LSTC, 2002). But honeycomb mechanical properties cannot be easily found on literature. Its properties will depend on the foil thickness and cell size. Kiliçaslan et al.

Figure 65 – Pedestrian legform dummy and its LS-Dyna FE model.

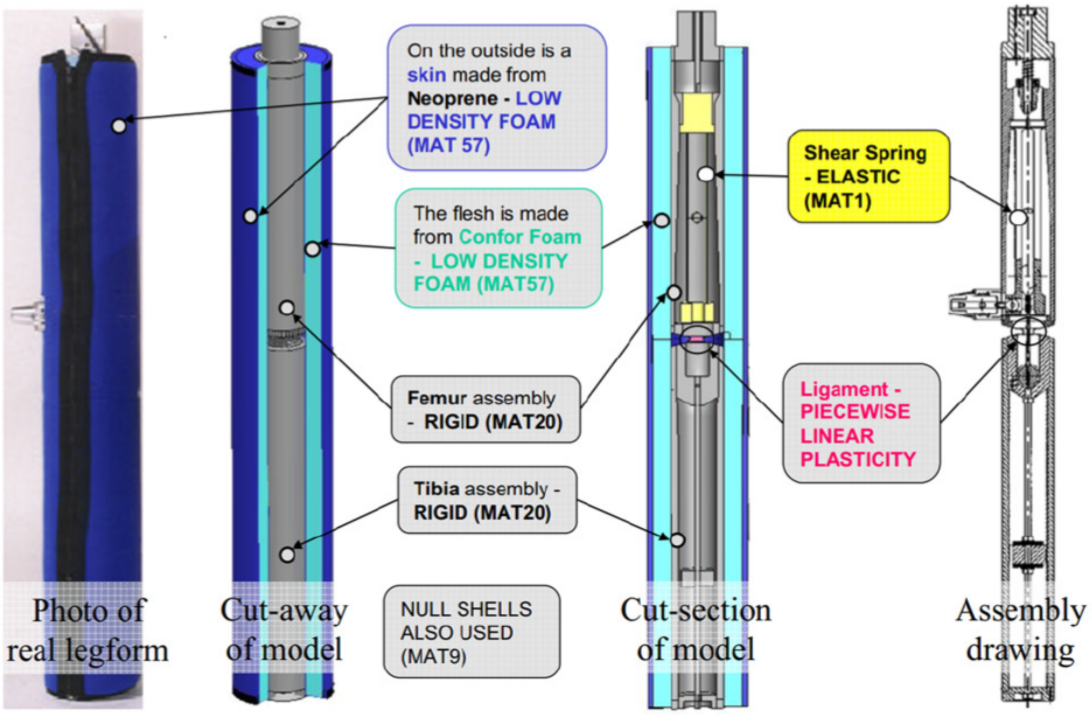

Source: Ptak et al. (2012).

(2014) suggests to simulate in FEM the mechanical properties of the honeycomb using a reduced portion of it.

With the honeycomb defined previously a numerical compression test in the axial direction with a 124mm height, width of 80mm and thickness 32mm (25 cells) was performed. This simple model contained 121 thousand deformable elements and the compression test with a velocity of 0.2 mm/s lasted approximately 100 hours. The results can be seen in Figure 67.

Figure 68 presents the stress strain results obtained in the simulation. The graphic presents consistent results with a peak stress in the beginning, a reduced value when buckling begins and a constant value through the buckling process. When the honeycomb reaches its compacted form, stress values increase rapidly, as expected.

To try to reduce computational time in other simulations the same test was performed in a reduced model, with only 8 cells and half of the initial thickness, to compare numerical results. The model is presented in Figure 69 and the numerical values comparison of stress and strain are presented in Figure 70.

Reduced model finished its simulation in a time of less than 24 hours and although the initial peak was a little higher than the peak obtained in the full model, Figure 70, the difference will not cause a huge variation in a global simulation. The rest of the graphic is

Figure 66 – Human body model medial collateral ligament (a) not broken and (b) broken.

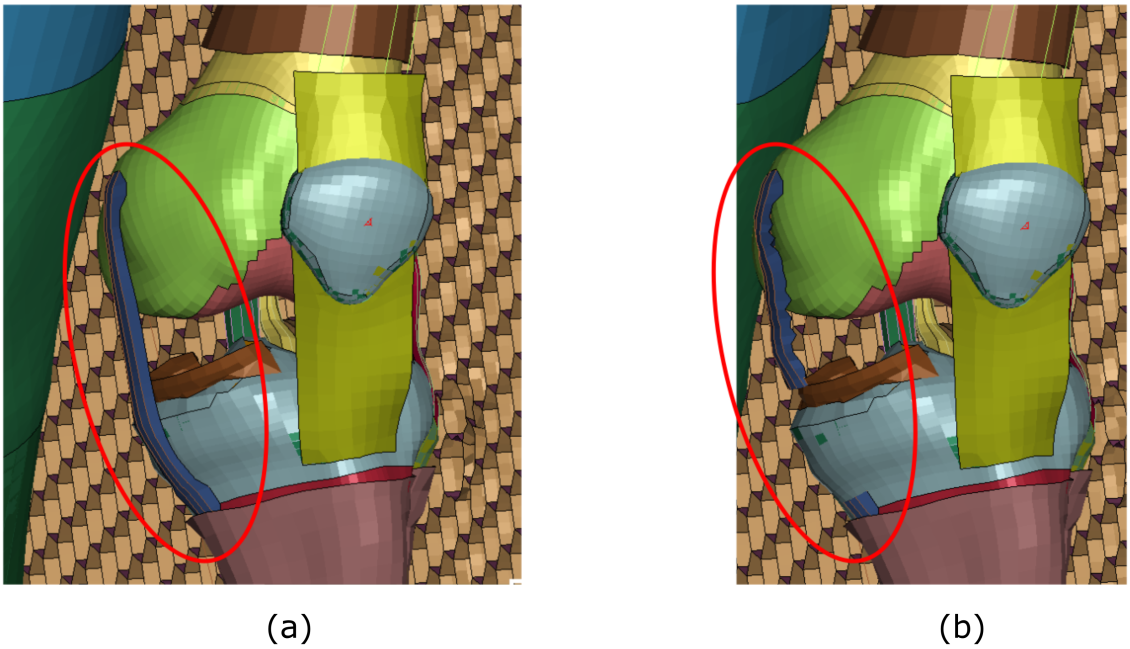
(a) (b)

Source: from author.

extremely similar showing that this specimen can be used in the curve calibrations.

Hence, the surrogate honeycomb was tested in its axial direction. The surrogate model is made of solid elements, Figure 71 and LS-Dyna *MAT_26 material considers its behavior as orthotropic with its load curves and directions being input of the program. The resulted curves for compression axial test is presented in Figure 72.

With the surrogate elements the initial peak happens with a delay when compared to the previous curves. Besides that, peak stress value is lower. But as this peak occurs is a small area, this could be tolerated for next simulations. The continuous range of the graph seems to have very similar values of over 70% volumetric compression.

This simulation lasted less than two hours and the model was much more stable than the model with shells.

Comparing the three curves of Figure 72 it is possible to conclude that the model may be used for the impact test.

6.3 Honeycomb surrogate model calibration

To continue the calibration of the surrogate honeycomb, lateral compression test was performed, as presented in Figure 73. The numerical results are presented in Figure 74.

Stress levels calculated in the lateral simulation are around 100 times lower than the values calculated in the axial direction. This was expected since this honeycomb was

Figure 67 – Compression test of the specimen in the axial direction. (a) 0% strain, (b) 20% strain, (c) 40% strain, (d) 60% strain.

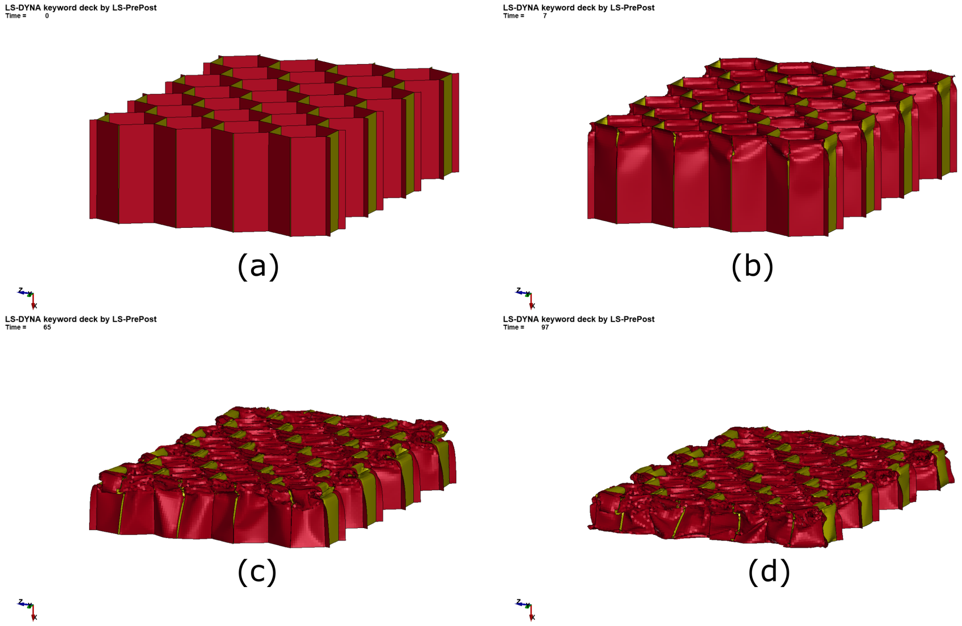

Source: from author.

Figure 68 – Compression axial test results

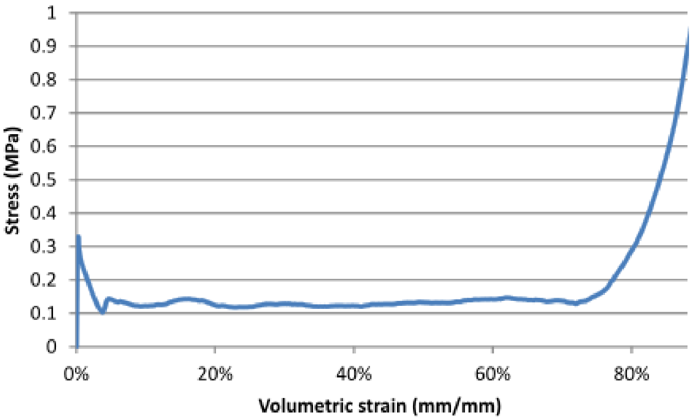

Source: from author.

intended to be used in its axial direction and values close to zero were expected in the lateral directions.

Only one direction was tested laterally, since the honeycomb is very similar in the two non axial directions and the values compared to the axial direction would be quite similar.

With the axial and lateral directions it is possible to model the material constitutive relations of LS-Dyna's MAT_026-Honeycomb (Appendix D). The knee dynamic rotation

Figure 69 – Compression axial test. (a) 0% volumetric strain and (b) 40% volumetric strain.

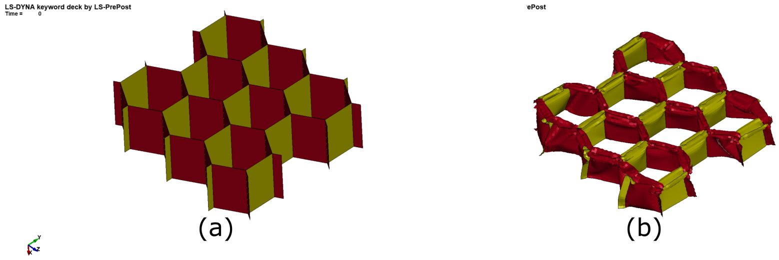

Source: from author.

Figure 70 – Compression test comparison.

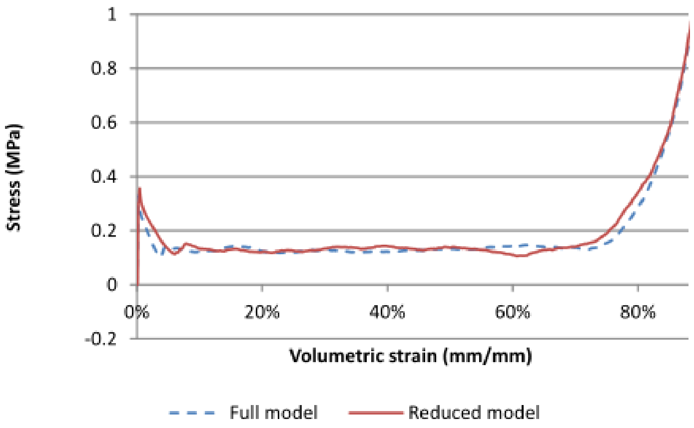

Source: from author.

calculated values are presented in Figure 75.

Figure 75 presents very good results demonstrating that the honeycomb modeled as surrogate elements can be used maintaining the accuracy of the simulation.

6.3.1 Other analysis to be performed in future works

The vehicle was not tested for rear crash collision. This could be done in a future work based on regulation UNECE R34. Rear collisions could lead to whiplash injuries resulting in neck pain, limited neck movement, visual disturbance and dizziness (HASSAN; SHI; MEGUID, 2019).

Other analysis could also be performed, as frontal collision against rigid pole, frontal collision against rigid wall, lateral collision with another car, etc.

It could also be evaluated crash tests specific for small and electric cars. Ko et al. (2015) makes an evaluation if physical tests are really necessary, proposing the use only of finite element simulations in this case. With this the costs involved on the crashs would be

Figure 71 – Compression axial test. (a) 0% volumetric strain and (b) 40% volumetric strain.

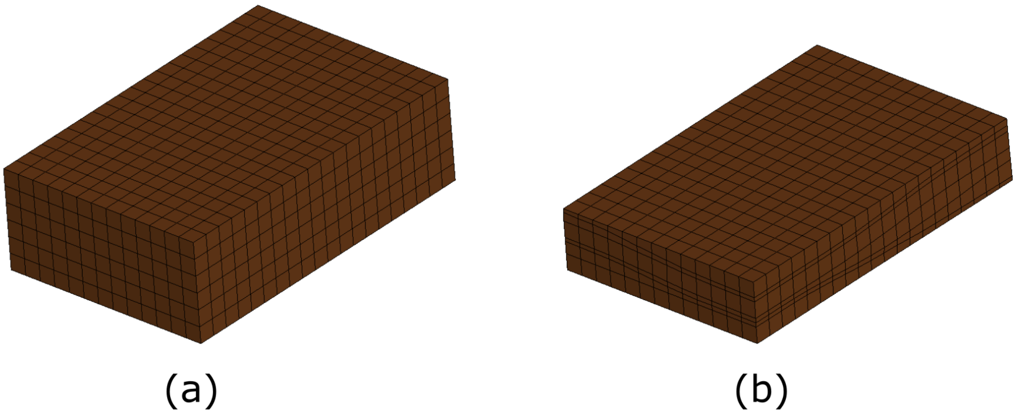

Source: from author.

Figure 72 – Compression axial test comparison.

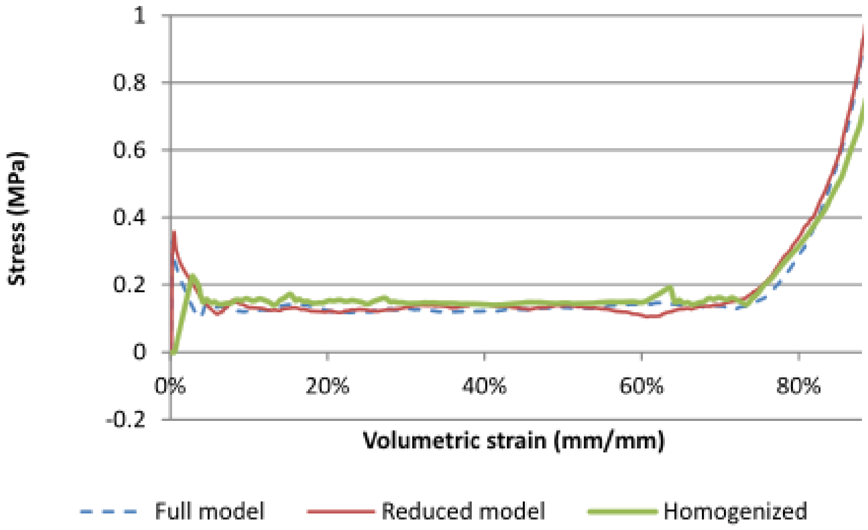

Source: from author.

substantially inferior. O'Malley et al. (2015) makes a summary of electric vehicles crash in the United States. Electric vehicles potential hazards are unique due to their electrical drive systems such as electrocution, fire, and electrolyte spillage.

Figure 73 – Lateral compression test. (a) 0% volumetric strain, (b) 20%, (c) 40% and (d) 60%.

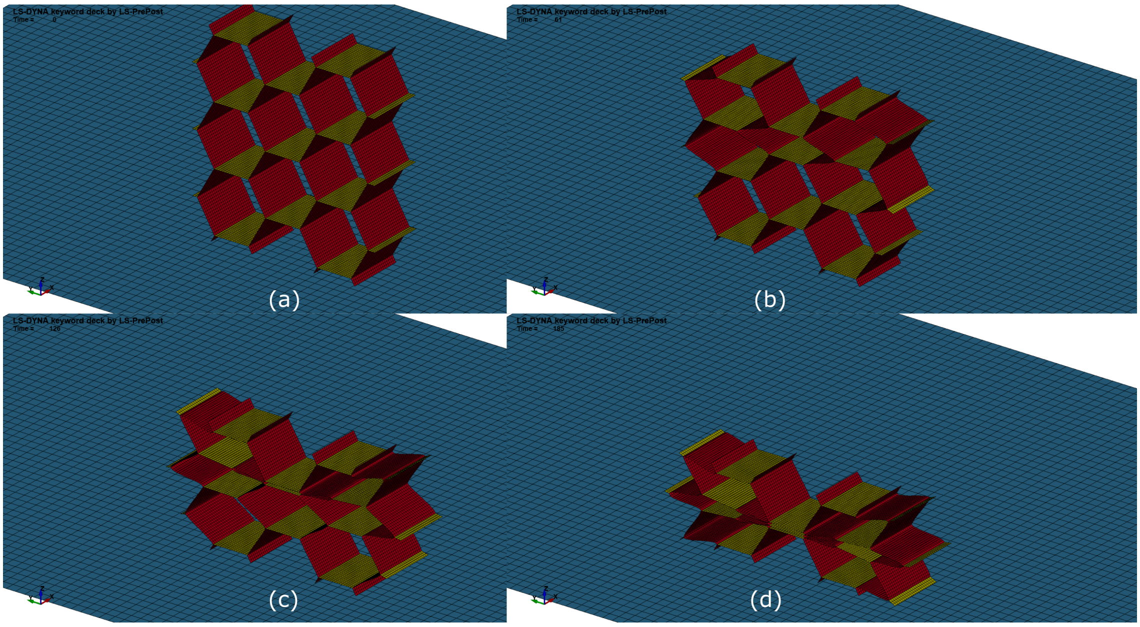

Source: from author.

Figure 74 – Comparison between axial and lateral compression simulation.

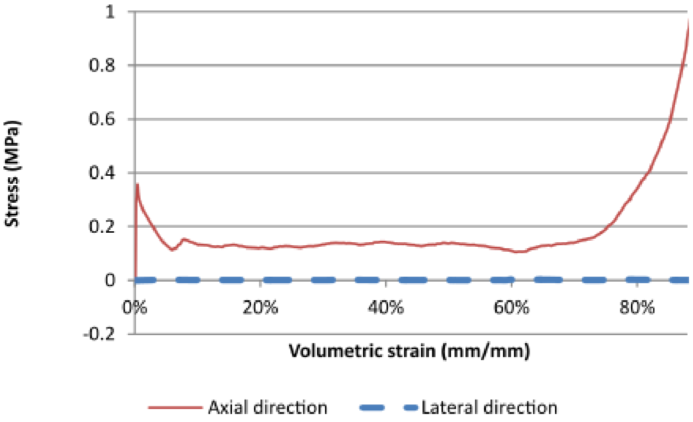

Source: from author.

Figure 75 – Right knee rotation comparison.

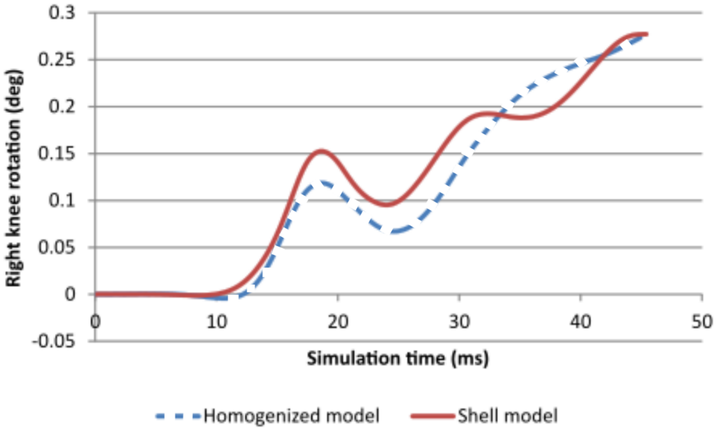

Source: from author.

7 CONCLUSION AND FUTURE WORKS

This dissertation presented the design of an electrical, compact and safe vehicle to be used in big urban environments. The vehicle is able to transport two passengers and has space for carrying small luggage or a few shopping.

To evaluate the vehicle safety it was performed simulations using the finite element method to check the car compliance with three UNECE regulations.

The first regulation deals with the vehicle crashing a deformable barrier with 40% width offset - ECE R94. In this regulation it was used two finite element models of the traditional anthropomorphic test devices (dummies). It was evaluated dummies responses of head acceleration, head injury criteria and forces on the dummy's body. This simulation was performed twice during the project. The first one was used to evaluate the initial vehicle design. The second one was performed after the vehicle was able to comply with ECE R127, which covers pedestrian safety.

As commented in the last paragraph, the second used regulation during the project was ECE R127 to evaluate pedestrian safety. In this simulation, the regulation was used as a reference but different criteria were employed to evaluate the vehicle crash against a human body model instead of traditional dummies. Human body models allow obtaining more information such as bone breaking, ligament rupture, among others.

The third regulation analyzed during this project was ECE R135, concerning the approval of vehicles with regard to their pole side performance. In this project step, the vehicle with one occupant (the World Side Impact Dummy) impacted a rigid pole laterally. It was evaluated on the simulations the dummies head and body forces besides the head injury criteria.

Most of the efforts spent on this project were to guarantee pedestrian safety. During this analysis it was studied the use of a honeycomb installed on the vehicle front to reduce pedestrian injuries and guarantee the regulation compliance. With the introduction of this structure bone fracture and ligament rupture did not occur during the simulations

The vehicle was able to perform well on the three regulation analysis. For this to be achieved, during the project vehicle shape, tube thicknesses and different concepts were tested. Besides that, changes were made on the finite element models to reduce the computational time and the simulation instabilities.

A wide range of studies can be performed for future works on this vehicle.

For crash safety, many regulations can still be evaluated. It still was not performed analysis concerning the frontal crash against rigid barrier, lateral collision with another car, rear collision, rollover analysis, etc. There are also a few regulations specifically made for electric vehicles (which covers the power train and structure interaction) and regulations made specifically for small cars (dealing with the different masses of vehicles during a collision).

Studies could be made on other car systems. For example, it was still not studied a suspension system developed specifically for this vehicle, the solution in this project was to adapt springs and shock absorbers of commercial vehicles, able to be bought on the market. Other systems that could also pass through a deep study are the driving system, brake system, etc. Besides that, the electrical propulsion system could also be analyzed, which is a huge subject by itself.

The material basis used for the structural components of the car was the advanced high strength steel dual phase 1000 (AHSS - DP1000). This material is expensive and not easy to find on the market. Other materials could be studied on the project and an evaluation of costs, weight increase and material availability could be performed.

BIBLIOGRAPHY

ARGOSY. **Argosy International | Honeycomb, Crash Test Barriers, Aerospace Coatings**. 2020. <https://www.argosyinternational.com/>.

BARNES, S. R.; BELAND, L.-P.; HUH, J.; KIM, D. The Effect of COVID-19 Lockdown on Mobility and Traffic Accidents: Evidence from Louisiana. **GLO Discussion Paper Series**, v. 616, 2020. Available on: <https://ideas.repec.org/p/zbw/glodps/616.html>.

BELLIS, M. **The History of Electric Vehicles Began in 1830**. 2019. <https://www.thoughtco.com/history-of-electric-vehicles-1991603>. Acessed: 08/07/2021.

BOSE, D.; BHALLA, K.; UNTAROIU, C.; IVARSSON, B.; CRANDALL, J.; HURWITZ, S. Injury Tolerance and Moment Response of the Knee Joint to Combined Valgus Bending and Shear Loading. **Journal of biomechanical engineering**, v. 130, p. 031008, jul. 2008.

BRASIL. **Lei Nº 13.755, de 10 de Dezembro de 2018**. 2018. <https://www.in.gov.br/web/dou/-/lei-n-13.755-de-10-de-dezembro-de-2018-167070058>. Acessed: 09/07/2021.

BRENNON, R. **Kinematics: The Mathematics of Deformation**. 2008. <https://scholar.googleusercontent.com/scholar?q=cache:_fAascZtbo8J:scholar.google.com/+kinematics+the+mathematics+of+deformation&hl=pt-BR&as_sdt=0,5&as_vis=1>. Acessed: 09/07/2021.

CATIA. **CATIA™ 3DEXPERIENCE® - Dassault Systèmes® 3D Software**. 2020. <https://www.3ds.com/products-services/catia/>. Acessed: 09/07/2021.

CCSA. **Center for Collision Safety and Analysis – Finite Element Models**. 2021. <https://www.ccsa.gmu.edu/models/>. Acessed: 08/07/2021.

CHO, Y.-B.; BAE, C.-H.; SUH, M.-W.; SIN, H.-C. A vehicle front frame crash design optimization using hole-type and dent-type crush initiator. **Thin-Walled Structures**, v. 44, p. 415–428, 2006. ISSN 0263-8231.

CHOU, C. C.; FILETA, B. B.; KHALIL, T. B.; KING, A. I.; MAHMOOD, H. F.; MERTZ, H. J.; WISMANS, J.; PRASAD, P.; BELWAFA, J. E. **Vehicle Crashworthiness and Occupant Protection**. [S.l.: s.n.], 2000.

CONSELHO NACIONAL DE TRÂNSITO. **Resolução Nº 756**. 2018. <https://www.in.gov.br/web/dou/-/resolucao-n-756-de-20-de-dezembro-de-2018-57495503?inheritRedirect=true#:~:text=Estabelece%20requisitos%20de%20prote%C3%A7%C3%A3o%20aos,decorrente%20de%20impacto%20nos%20ve%C3%ADculos.> Acessed: 09/07/2021.

COOK, R. D.; MALKUS, D. S.; PLESHA, M. E. **Concepts and Applications of Finite Element Analysis**. Fourth. New York, NY: John Wiley & Sons, 2001. ISBN 978-0-471-35605-9.

DAVENPORT, C. U.S. to Announce Rollback of Auto Pollution Rules, a Key Effort to Fight Climate Change. **The New York Times**, mar. 2020. ISSN 0362-4331.

de Lima, A. **Desenvolvimento de um veículo urbano seguro utilizando otimização baseada em metamodelos.** maio 2016. Tese (text) — Universidade de São Paulo, maio 2016.

FILDES, B.; GABLER, H. C.; OTTE, D.; LINDER, A. Pedestrian Impact Priorities Using Real-World Crash Data and Harm. **Proceedings of the IRCOBI - International Research Council on the Biomechanics of Impact**, 2004.

GAYZIK, F.; MORENO, D.; GEER, C.; WUERTZER, S.; MARTIN, R.; STITZEL, J. Development of a Full Body CAD Dataset for Computational Modeling: A Multi-Modality Approach. **Annals of biomedical engineering**, v. 39, p. 2568–83, jul. 2011.

GHBMC. **Home**. 2020. <http://www.ghbmc.com/>. Acessed: 09/07/2021.

GLOBAL EV Outlook: Understanding the Electric Vehicle. 2014. <https://www.iea.org/reports/global-ev-outlook-2021>. Acessed: 09/07/2021.

GUARNIERI, M. When cars went electric, part 1. **IEEE Industrial Electronics Magazine**, v. 5, p. 61–62, mar. 2011.

GUARNIERI, M. When Cars Went Electric, Part 2 [Historical]. **Industrial Electronics Magazine, IEEE**, v. 5, p. 46–53, jul. 2011.

HANSSEN, A. G.; STöBENER, K.; RAUSCH, G.; LANGSETH, M.; KELLER, H. Optimisation of energy absorption of an a-pillar by metal foam insert. **International Journal of Crashworthiness**, Taylor & Francis, v. 11, n. 3, p. 231–242, mar 2006. Available on: <https://doi.org/10.1533/ijcr.2005.0396>.

HAPPIAN-SMITH, J. **An Introduction to Modern Vehicle Design**. Second. [S.l.]: SAE International, 2002.

HASSAN, M. T. Z.; SHI, M. G.; MEGUID, S. A. Nonlinear multibody dynamics and finite element modeling of occupant response: Part I—rear vehicle collision. **International Journal of Mechanics and Materials in Design**, v. 15, n. 1, p. 3–21, mar. 2019. ISSN 1573-8841.

HOMM, F.; HESSEL, M.; WOLFF, S.; SCHMID, W.; LIENKAMP, M. **The state of electromobility 2020: Endgame after the Corona crisis**. Research Gate, 2020. Available on: <https://www.researchgate.net/profile/Markus_Lienkamp/publications?pubType=bookv=prf_pubs_book>.

HUMANETICS. **WorldSID-50M**. 2021. <https://humanetics.humaneticsgroup.com/products/anthropomorphic-test-devices/side-impact/worldsid-50m>. Acessed: 09/07/2021.

HYPERWORKS. **HyperMesh**. 2017. <https://www.altair.com/hyperworks/>. Acessed: 09/07/2021.

IEA. **Global EV Outlook 2019 - Scaling up the Transition to Electric Mobility**. 2019. <https://www.iea.org/reports/global-ev-outlook-2019>.

INFOSIGA. **Estatística / Relatórios INFOSIGA SP**. 2020. <http://www.infosiga.sp.gov.br/>. Acessed: 09/07/2021.

IRTAD. **Irtad Road Safety Annual Report 2020**. 2020. 64 p. <https://www.itf-oecd.org/road-safety-annual-report-2020>. Acessed: 09/07/2021.

JOHNSON, G.; COOK, W. A Constitutive Model and Data for Metals Subjected to Large Strains, High Strain Rates, and High Temperatures. **7th International Symposium on Ballistics**, p. 541–547, abr. 1983.

KERRIGAN, J.; CRANDALL, J.; DENG, B. Pedestrian kinematic response to mid-sized vehicle impact. **International Journal of Vehicle Safety**, v. 2, jan. 2007.

KILIÇASLAN, C.; ODACι, İ. K.; TAŞDEMIRCI, A.; GÜDEN, M. Experimental Testing and Full and Homogenized Numerical Models of the Low Velocity and Dynamic Deformation of the Trapezoidal Aluminium Corrugated Core Sandwich. **Strain**, v. 50, n. 3, p. 236–249, 2014. ISSN 1475-1305.

KITAGAWA, Y.; HAGIWARA, I.; TSUDA, M. Development of a collapse modecontrol method for side member in vehicle collisions. **SAE**, 1991.

KO, M.-G.; JANG, D.-Y.; JOO, J.-W.; KIM, K.-D.; KIM, D.-S. Estimating the crash responses of a vehicle from the other size vehicle tested. **International Journal of Crashworthiness**, Taylor & Francis, v. 20, n. 2, p. 165–176, 2015. Available on: <https://doi.org/10.1080/13588265.2014.993115>.

LALWALA, M.; CHAWLA, A.; THOMAS, P.; MUKHERJEE, S. Finite element reconstruction of real-world pedestrian accidents using thums pedestrian model. **International Journal of Crashworthiness**, Taylor & Francis, v. 25, n. 4, p. 360–375, 2020. Available on: <https://doi.org/10.1080/13588265.2019.1594547>.

LARMINIE, J.; LOWRY, J. Electric vehicle technology explained. In: . [S.l.]: John Wiley and Sons, 2012. ISBN 978-1-119-94273-3.

LEEM, D.; BONG, H.-J.; BARLAT, F.; LEE, M.-G.; SONG, J.-H.; KIM, D. Enhancement in the Modeling of Temperature and Strain Rate-Dependent Plastic Hardening Behavior of a Sheet Metal. **steel research international**, v. 86, n. 8, p. 902–914, 2015. ISSN 1869-344X.

LIN, M.-P.; CHANG, C.-M.; TAI, C.-H.; LEE, C.-T. Usage of LSTC_NCAC Hybrid III 50th Dummy in Frontal Occupant Simulation. **13th International LS-DYNA Users Conference**, p. 10, 2014.

LSTC. **LS-Dyna Manual - Vol II**. 1st edition. ed. Livermore, California: LSTC, 2002. I.

LSTC. **LS-PrePost**. 2017. <https://www.lstc.com/products/ls-prepost>. Acessed: 08/07/2021.

LSTC. **Download LST, LLC Barrier, Dummy, and Tire Models for LS-DYNA | Livermore Software Technology Corp.** 2020. <https://www.lstc.com/download/dummy_models>. Acessed: 09/07/2021.

LSTC. **LS-DYNA Livermore Software Technology Corp.** 2020. <https://www.lstc.com/products/ls-dyna>. Acessed: 09/07/2021.

LSTC. **LSTC Models Overview | Livermore Software Technology Corp.** 2020. <https://www.lstc.com/>. Acessed: 12/07/2021.

MARANO, V.; ONORI, S.; GUEZENNEC, Y.; RIZZONI, G.; MADELLA, N. Lithium-ion batteries life estimation for plug-in hybrid electric vehicles. In: **2009 IEEE Vehicle Power and Propulsion Conference**. Dearborn, MI: IEEE, 2009. p. 536–543. ISBN 978-1-4244-2600-3.

MARTIN, J.-L.; LARDY, A.; LAUMON, B. Pedestrian Injury Patterns According to Car and Casualty Characteristics in France. **Annals of Advances in Automotive Medicine / Annual Scientific Conference**, v. 55, p. 137–146, out. 2011. ISSN 1943-2461.

NEWMARK, N. M. A Method of Computation for Structural Dynamics. **Journal of Engineering Mechanics Division**, 1959.

NOH, M.-H.; LEE, S.-Y. Parametric impact performances in a new type crash cushion barrier system using an energy absorption pipe. **International Journal of Crashwothiness**, v. 25, p. 106–119, 2020. ISSN 1358-8265.

O'MALLEY, S.; ZUBY, D.; MOORE, M.; PAINE, M.; PAINE, D. Crashworthiness testing of electric and hybrid vehicles. In: **24th International Technical Conference on the Enhanced Safety of Vehicles (ESV)**. [S.l.: s.n.], 2015.

PENG, Y.; YANG, J.; DECK, C.; WILLINGER, R. Finite element modeling of crash test behavior for windshield laminated glass. **International Journal of Impact Engineering**, v. 57, p. 27–35, 2013. ISSN 0734-743X.

PRF. **Acidentes**. 2020. <https://www.gov.br/prf/pt-br/acesso-a-informacao/dados-abertos/dados-abertos-acidentes>. Acessed: 12/07/2021.

PTAK, M.; RUSIŃSKI, E.; KARLIŃSKI, J.; DRAGAN, S. Evaluation of kinematics of SUV to pedestrian impact—Lower leg impactor and dummy approach. **Archives of Civil and Mechanical Engineering**, v. 12, n. 1, p. 68–73, mar. 2012. ISSN 1644-9665.

RAMONI, M. O.; ZHANG, H.-C. End-of-life (EOL) issues and options for electric vehicle batteries. **Clean Technologies and Environmental Policy**, v. 15, n. 6, p. 881–891, dez. 2013. ISSN 1618-9558.

REID, J. D. Crashworthiness of automotive steel midrails: thickness andmaterial sensitivity. **Thin-Walled Structures**, 1996.

REID, J. D. Towards the understanding of material property influence onautomotive crash structures. **Thin-Walled Structures**, 1996.

ROHLMANN, A.; NELLER, S.; CLAES, L.; BERGMANN, G.; WILKE, H. Influence of a Follower Load on Intradiscal Pressure and Intersegmental Rotation of the Lumbar Spine. **Spine**, v. 26, p. E557–61, jan. 2002.

SINDIPEÇAS. **Relatório Da Frota Circulante**. 2019. <https://www.sindipecas.org.br/area-atuacao/?co=s&a=frota-circulante>. Acessed: 12/07/2021.

SONG, R.-b.; DAI, Q.-f. Dynamic Deformation Behavior of Dual Phase Ferritic-Martensitic Steel at Strain Rates From 10-4 to 2000 s-1. **Journal of Iron and Steel Research International**, v. 20, n. 8, p. 48–53, ago. 2013. ISSN 2210-3988.

STAHLSCHMIDT, S.; HUANG, Y.; SCHIF, A. **PDB LS-DYNA WorldSID 50th – Version 7.1**. [S.l.: s.n.], 2020.

TERESIŃSKI, G.; MADRO, R. Knee joint injuries as a reconstructive factors in car-to-pedestrian accidents. **Forensic Science International**, v. 124, n. 1, p. 74–82, dez. 2001. ISSN 0379-0738.

UMALE, S.; ARUN, M.; HAUSCHILD, H.; HUMM, J.; PINTAR, F.; YOGANANDAN, N. Quantitative Evaluation of THOR, World SID and Hybrid III under Far-Side Impacts: A Finite Element Study. In: **IRCOBI Conference**. [S.l.: s.n.], 2018. p. 22.

UNECE. **1958 Agreement - Transport - UNECE**. 1958. <https://unece.org/trans/main/wp29/wp29regs>. Acessed: 12/07/2021.

UNECE. **Regulation No. 127 - Uniform Provisions Concerning the Approval of Motor Vehicles with Regard to Their Pedestrian Safety Performance**. 2012. <https://unece.org/transport/vehicle-regulations-wp29/standards/addenda-1958-agreement-regulations-121-140>. Acessed: 12/07/2021.

UNECE. **Uniform Provisions Concerning the Approval of Vehicles with Regard to Their Pole Side Impact Performance (PSI)**. 2016. <https://unece.org/transport/vehicle-regulations-wp29/standards/addenda-1958-agreement-regulations-121-140>. Acessed: 12/07/2021.

UNECE. **Consolidated Resolution on the Construction of Vehicles (R.E.3)**. 2017. <https://unece.org/transport/standards/transport/vehicle-regulations-wp29/resolutions>. Acessed: 12/07/2021.

UNECE. **Regulation No. 94 - Uniform Provisions Concerning the Approval of Vehicles with Regard to the Protection of the Occupants in the Event of a Frontal Collision**. 2017. <https://unece.org/transport/vehicle-regulations-wp29/standards/addenda-1958-agreement-regulations-81-100>. Acessed: 12/07/2021.

UNTAROIU, C.; DARVISH, K.; CRANDALL, J.; DENG, B.; WANG, J. Development and Validation of a Finite Element Model of the Lower Limb. In: **Transportation 2004: Transportation and Environment**. [S.l.: s.n.], 2004.

UNTAROIU, C.; PAK, W.; MENG, Y.; SCHAP, J.; KOYA, B.; GAYZIK, F. A Finite Element Model of a Midsize Male for Simulating Pedestrian Accidents. **Journal of biomechanical engineering**, v. 140, set. 2017.

US Government Accountability Office. PEDESTRIAN SAFETY - NHTSA Needs to Decide Whether to Include Pedestrian Safety Tests in Its New Car Assessment Program. p. 70, abr. 2020.

VIANO, D. C. **Biomechanical Responses and Injuries in Blunt Lateral Impact**. Warrendale, PA, 1989.

WANG, J.; XU, Y.; ZHANG, W. Finite element simulation of PMMA aircraft windshield against bird strike by using a rate and temperature dependent nonlinear viscoelastic constitutive model. **Composite Structures**, v. 108, p. 21–30, fev. 2014. ISSN 0263-8223.

WHO. Global Health Estimates: Life expectancy and leading causes of death and disability. 2020.

WOOLF, S. H.; CHAPMAN, D. A.; LEE, J. H. COVID-19 as the Leading Cause of Death in the United States. **JAMA**, dez. 2020. ISSN 0098-7484.

WORLD HEALTH ORGANIZATION. **Global Status Report on Road Safety 2018**. Geneva, Switzerland: [s.n.], 2018.

YAMAGUCHI, S.; KATO, H.; OKAZAKI, T. Efficient energy absorption ofautomobile side rails. In: **10th international technical conference onexperimental safety vehicles**. [S.l.: s.n.], 1985.

YONG, J. Y.; RAMACHANDARAMURTHY, V. K.; TAN, K. M.; MITHULANANTHAN, N. A review on the state-of-the-art technologies of electric vehicle, its impacts and prospects. **Renewable and Sustainable Energy Reviews**, v. 49, p. 365–385, set. 2015. ISSN 1364-0321.

YOUN, Y.; LEE, E.-D.; KIM, D.-u. A comparison study of two side impact dummies based on the probability of injury risk curves. In: **23rd International Technical Conference on the Enhanced Safety of Vehicles (ESV)**. [S.l.: s.n.], 2000. v. 22, p. 7. ISSN 0217-9792.

Appendix

APPENDIX A – ECE R94 CRITERIA

A.1 Head Injury Criterion (HIC)

The head injury criterion $(HIC_{xx})^1$ is considered valid when during the whole simulation no contact between dummy and any other component of the car occurs. If during the test there is no contact between car and dummy, HIC can be calculated according to Equation A.1.1.

$$HPC = max\left\{(t_2 - t_1)\left[\frac{1}{t_2 - t_1}\int_{t_1}^{t_2} adt\right]^{2.5}\right\} \tag{A.1.1}$$

In which the term a is the resultant acceleration of a point in dummy´s head and is calculated in units of gravity, g (1 g = 9.8 m/s^2), t_2 and t_1 shall be an interval of 36 ms and it should be expressed in seconds and calculated during the whole simulation. HPC will be the maximum value calculated.

A.2 Injury criteria for neck

These criteria are determined by the compressive axial force, the axial tensile force and the fore/aft shear forces at the head/neck interface, expressed in kN. Besides that, neck flexion bending moment, expressed in Nm, shall be recorded.

A.3 Thorax compression criterion (THCC) and Viscous Criterion (V*C)

The thorax compression criterion is determined by the absolute value of the thorax deformation, expressed in mm.

The viscous criterion (V*C) is calculated as the instantaneous product of the compression and the rate of deflection of the sternum.

---

[1] xx is the period of time which HIC is calculated. If xx equals 36 ms this means that t2 - t1 = 36 ms. This is the criteria used in ECE R94. But in car to pedestrian collision the period of time is 15 ms so t2 - t1 = 15 ms.

APPENDIX B – FINITE ELEMENT METHOD - EXPLICIT INTEGRATION

Vehicle crashworthiness analysis has evolved considerably in the last 40 years, specially due to the use of finite element method (FEM). The reason of this evolution is that in the last decades computer became much more accessible and its capacity of process data has increased a lot and continue to increase. This allowed more detailed models that are able to predict with acceptable confidence the vehicle response (CHOU et al., 2000).

FEM of structural dynamics solves numerically a set of nonlinear partial differential equations of motion in the space-time domain, coupled with material stress-strain relations along with definition of appropriate initial and boundary conditions. The solution first discretizes the equations in space by formulating the problem in a weak variational form and assuming an admissible displacement field. This yields a set of second order differential equations in time. Then the system of equations is solved by discretization in time domain. The discretization is accomplished by the classical Newark-Beta method (NEWMARK, 1959).

The technique may be called implicit if the selected integration parameters render the equations coupled, and in this case the solution is unconditionally stable. If the integration parameters are selected to decouple the equations then the solution may be called explicit and is conditionally stable.

The explicit FE technique solves a set of hyperbolic wave equations in the zone of influence of the wave front, and accordingly does not require coupling of large number of equations. On the other hand it needs a time step small enough to grantee the stability of the simulation. For crash simulations involving extensive use of contact, multiple material models and a combination of different elements it turned out that explicit solvers are more robust and computationally more efficient than implicit ones.

B.1 Formulation

Equations that govern the dynamic response will require that the work of the external forces be absorbed by the work of internal, inertial and viscous forces for any small kinematically admissible motion (COOK; MALKUS; PLESHA, 2001). For a single element, this work balance can be written as Equation B.1.1.

$$\begin{aligned}\int_{V_e}\{\delta u\}^T\{F\}dV+\int_{S_e}\{\delta u\}^T\{\Phi\}dS+\sum_{i=1}^{n}\{\delta u\}_i^T\{p\}_i\\ =\int_{V_e}\Big(\{\delta\epsilon\}^T\{\sigma\}+\{\delta u\}^T\rho\{\ddot{u}\}\Big)+\{\delta u\}^T K_d\{\dot{u}\}\end{aligned} \tag{B.1.1}$$

Where $\{\delta u\}$ and $\{\delta\epsilon\}$ are respectively small arbitrary displacements and their correspondent strains, $\{F\}$ are body forces, $\{\Phi\}$ are prescribed surface tractions (which typically are non zero over only a portion of surface S_e), $\{p\}_i$ are concentrated loads that act at a nodal of n points on the element, $\{\delta u\}_i^T$ is the displacement of the point at which load $\{p\}_i$ is applied, ρ is the mass density of the material, k_d is a material-damping parameter and volume integration is carried out over the element volume V_e.

We can use the interpolation functions to calculate the displacements and its derivatives at any point of the element using Equation B.1.2.

$$\{u\} = [N]\,\{d\} \qquad \{\dot{u}\} = [N]\{\dot{d}\} \qquad \{\ddot{u}\} = [N]\{\ddot{d}\} \tag{B.1.2}$$

Where $[N]$ are the shape functions, that are dependent of space only while $\{d\}$ is dependent of time only.

From solid mechanics we have the following relations

$$\{u\} = [K]^{-1}\{F\} \qquad \{\varepsilon\} = [B]\{u\} \qquad \sigma = [D]\{\varepsilon\} \tag{B.1.3}$$

where $[K]$ is the stiffness matrix, $\{B\}$ is the spatial derivative of the shape functions and $[D]$ is the flexural rigidity matrix.

Combining of Equation B.1.1, Equation B.1.2 and Equation B.1.3 yields

$$\begin{aligned}\{\delta d\}^T \Bigg[\int_{V_e} [B]^T\{\sigma\}dV + \int_{V_e} \rho[N]^t[N]dV\{\ddot{d}\} + \int_{V_e} k_d[N]^t[N]dV\{\dot{d}\} \\ - \int_{V_e} [N]^T\{F\}dV - \int_{S_e} [N]^T\{\Phi\}dS - \sum_{i=1}^{n}\{p\}_i\Bigg] = 0\end{aligned} \tag{B.1.4}$$

in which it has been assumed that the locations of concentrated loads $\{p\}_i$ are coincident with node point locations. Since $\{\delta d\}$ is arbitrary, Equation B.1.4 can be written as

$$[m]\{\ddot{d}\} + [c]\{\dot{d}\} + \{r^{int}\} = \{r^{ext}\} \tag{B.1.5}$$

where the element mass and damping matrices are defined as

$$[m] = \int_{V_e} \rho[N]^t[N]dV \tag{B.1.6}$$

$$[c] = \int_{V_e} k_d [N]^t [N] dV \tag{B.1.7}$$

and the element internal and external forces are defined as

$$\{r^{int}\} = \int_{V_e} [B]^T \{\sigma\} dV \tag{B.1.8}$$

$$\{r^{ext}\} = \int_{V_e} [N]^T \{F\} dV + \int_{S_e} [N]^T \{\Phi\} dS + \sum_{i=1}^{n} \{p\}_i \tag{B.1.9}$$

As can be seen in Equation B.1.5 the system is still coupled, second order and ordinary differential equation in time and it is called a finite element semidiscretization. In this case, displacements $\{d\}$ are discrete functions of space but they are still continuous functions of time. And to solve this equation, one of the methods that can be utilized and is the method that was used in this dissertation software is the explicit integration.

For linear elastic material behavior, $\{\sigma\} = [E][B]\{d\}$ where $[E]$ is the constitutive matrix and Equation B.1.8 becomes

$$\{r^{int}\} = [k]\{d\} \tag{B.1.10}$$

where the stiffness matrix $[k]$ can be defined as

$$[k] = \int_{V_e} [B]^T [E][B] dV \tag{B.1.11}$$

Substituting Equation B.1.11 in Equation B.1.5 gives

$$[m]\{\ddot{d}\} + [c]\{\dot{d}\} + [k]\{d\} = \{r^{ext}\} \tag{B.1.12}$$

which is equivalent to say that external loads are equilibrated by a combination of inertial, damping and elastic forces.

When Equation B.1.5 is used in the whole model and not in an element anymore we can write

$$[M]\{\ddot{D}\} + [C]\{\dot{D}\} + [K]\{D\} = \{R^{ext}\} \tag{B.1.13}$$

or, if the condition of linearity is not used

$$[M]\{\ddot{D}\} + [C]\{\dot{D}\} + \{R^{int}\} = \{R^{ext}\} \tag{B.1.14}$$

B.2 Direct integration method - Explicit integration

In direct integration, a finite element approximation is used to replace the time derivatives by differences of displacement at various instants of time. So we can write Equation B.1.14 at a specific instant of time,

$$[M]\{\ddot{D}\}_n + [C]\{\dot{D}\}_n + \{R^{int}\}_n = \{R^{ext}\}_n \tag{B.2.15}$$

in which the subscript n denotes time $n\Delta t$ in which Δt indicates the increment of time in each step.

In explicit integration method D_n is considered to be dependent only of the history of the simulation, i.e.

$$\{D\}_{n+1} = f(\{D\}_n, \{\dot{D}\}_n, \{\ddot{D}\}_n, \{D\}_{n-1}, \dots) \tag{B.2.16}$$

Utilizing the central-difference method it is possible to approximate velocity and acceleration by

$$\{\dot{D}\}_{n-1/2} = \frac{1}{\Delta t}(\{D\}_n - \{D\}_{n-1}) \tag{B.2.17}$$

$$\{\dot{D}\}_{n+1/2} = \frac{1}{\Delta t}(\{D\}_{n+1} - \{D\}_n) \tag{B.2.18}$$

$$\begin{aligned} \{\ddot{D}_n\} &= \frac{1}{\Delta t}(\{\dot{D}\}_{n+1/2} - \{\dot{D}\}_{n-1/2}) \\ &= \frac{1}{\Delta t}(\{D\}_{n+1} - 2\{D\}_n + \{D\}_{n-1}) \end{aligned} \tag{B.2.19}$$

Equation B.1.13 is modified by lagging the velocity by half time step:

$$[M]\{\ddot{D}\}_n + [C]\{\dot{D}\}_{n-1/2} + [K]\{D\}_n = \{R^{ext}\}_n \tag{B.2.20}$$

The combination of B.2.18 and B.2.20 yields the solution of the problem:

$$\begin{aligned} &\frac{1}{\Delta t^2}[M]\{D\}_{n+1} = \\ &\qquad \{R^{ext}\}_n - [K]\{D\}_n + \frac{1}{\Delta t^2}[M](\{D\} + \Delta t\{\dot{D}\}_{n-1/2} - [C]\{\dot{D}\}_{n-1/2} \end{aligned} \tag{B.2.21}$$

If $[M]$ is lumped, then the computation of $\{D\}_{n+1}$ does not require the solution of simultaneous equations. The method requires $\{\dot{D}\}_{-1/2}$ which can be achieved using an initial negative time step, that is

$$\{\dot{D}\}_{-1/2} = \{\dot{D}\}_0 - \frac{\Delta t}{2}\{\ddot{D}\}_0 \tag{B.2.22}$$

Where $\{\ddot{D}\}_0$ can be obtained from

$$\{\ddot{D}\}_0 = [M]^{-1}(\{R^{ext}\}_0 - [K]\{D\}_0 - [C]\{\dot{D}\}_0) \tag{B.2.23}$$

APPENDIX C – KINEMATICS - THE MATHEMATICS OF DEFORMATION

According to Brennon (2008) kinematics is the mathematical representation of motion. By motion we mean velocity, acceleration, rotation, etc. Kinematics does not deal with physical principles like force or torque. These are mechanical concepts. Physics deals with the relation between loads and motion, e.g. the famous equation $F = ma$ is a physical expression that relates the force applied to a body and its accelerations with mass being a proportionality factor.

C.1 Deformation

Consider a pseudo 2D deformable body in its initial configuration Ω_0, as presented in Figure 76. $\underset{\sim}{X}$ represents the initial position of a point in the body, the colored squares represents small parts of body and L_0 represents its the initial thickness. Disregarding fracture, each point in the body can have a unique initial (pre deformation) location and Let´s call the "particle $\underset{\sim}{X}$" the particle that was initially in the $\underset{\sim}{X}$ position. Let Ω denote the body after the deformation. In this chapter it is intended to define the standards methods used to quantify relationship between Ω_0 and Ω.

Figure 76 – First AUS results.

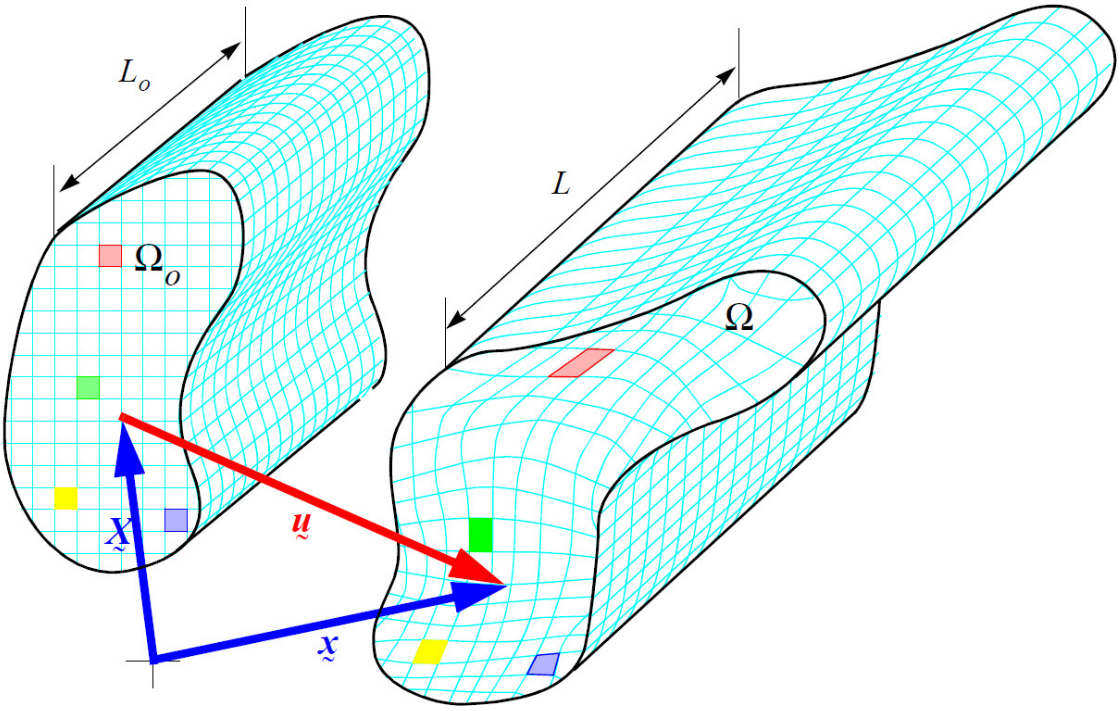

Source: Brennon (2008).

As seen in Figure 76 after the deformation the particle $\underset{\sim}{X}$ moves to a new location

$\underset{\sim}{x}$ and because two particles are not allowed to occupy the same place, the key relationship between Ω_0 and Ω is the **mapping function**, $\underset{\sim}{x} = \chi(\underset{\sim}{X})$ that relates the undeformed and deformed position vectors.

In the representation of Figure 76 shape deformation happened only in two dimensions, as can be seen in the colored squares, although its thickness changed and for this reason it is called pseudo 2D deformation. In the figure it is possible to see that the initial thickness L_0 was also deformed assuming the value L visibly bigger than the initial one. So this deformation has occurred actually in three dimensions (with one dimension being the out of plane). In this annex motion will be illustrated in the context of pseudo 2D deformations, but they can be applied to general deformations.

The elements of the body cannot be "inverted". This constraint is called "local admissibility" of the deformation and it is ensured if the matrix $[\partial x/\partial X]$ has a positive determinant. However, local admissibility does not guarantee "global admissibility", which requires the mapping function to be invertible and for this reason prohibits inter-penetration. Local admissibility may be controlled in finite element method with the use of hourglass control while global admissibility needs the use of contact algorithms

C.2 Displacement

The displacement of a particle is the vector extending from a particle´s initial position to its deformed location:

$$\underset{\sim}{u} = \underset{\sim}{x} - \underset{\sim}{X} \tag{C.2.1}$$

$\underset{\sim}{X}$ and $\underset{\sim}{x}$ are the initial and final position vectors of the particle. They are dependent of the chosen system origin so choosing different system origin would result in different vector.

$$\underset{\sim}{u}$$

on the other hand is independent of the origin. So independently of system origin the vector is always the same.

C.3 Deformation gradient - graphical introduction

The deformation gradient is a tensor that quantifies the shape change as well as overall material rotation. The deformation gradient is more comprehensive than strain measurements to calculate the material deformation. With the deformation gradient it is possible to calculate strain, the conversion is not true. In this section it will be described how to graphically approximate the deformation gradient tensor by simply looking at the deformation.

A cube can be characterized by three orthonormal vectors that form its edges. In the same way a parallelepiped may be characterized by three vectors forming its edges. The deformation gradient tensor $\underset{\approx}{F}$ quantifies the changes in the edge vectors assembling the three deformed edge vectors into columns of a $3X3$ matrix of components. If the coordinate system is Cartesian, the columns of the deformation gradient are the vectors defining the parallelepiped edge vectors, expressed relative to the undeformed edge vectors that defined the initial cube's edge directions. Considering that the initial particle of the body is a unit cube with the edges coincident with the orthonormal lab basis, $\{\underset{\sim}{e}_1, \underset{\sim}{e}_2, \underset{\sim}{e}_3\}$, when deformed the vectors that form the edges of the parallelepiped may be represented by a new set $\{\underset{\sim}{g}_1, \underset{\sim}{g}_2, \underset{\sim}{g}_3\}$. If we find the i^{th} deformed edge vectors in relation with the initial basis and assemble them in the i^{th} column of the matrix $\underset{\approx}{F}$, then the result will be the deformation gradient matrix $\underset{\approx}{F}$ with respect to the $\{\underset{\sim}{e}_1, \underset{\sim}{e}_2, \underset{\sim}{e}_3\}$. Mathematically, this may be expressed by

$$\underset{\sim}{g}_k = \underset{\approx}{F} \cdot \underset{\sim}{e}_k \tag{C.3.2}$$

or, equivalently,

$$\underset{\sim}{g}_k = F_{jk} \underset{\sim}{e}_j . \tag{C.3.3}$$

The deformed $\underset{\sim}{g}_k$ edge vector are not (generally) of unit length or orthogonal. They are called "material vectors" because they "travel along" with the same set of material points. In general, if $\underset{\sim}{M}$ is a material vector in the initial configuration (not necessarily of unit length), then it will flow with the material to became a new (stretched and rotated) vector $\underset{\sim}{m}$ in the deformed configuration, given by

$$\underset{\sim}{m} = \underset{\approx}{F} \cdot \underset{\sim}{M}, \text{ and the “fiber stretch” is defined by } \lambda = ||\underset{\sim}{m}||/||\underset{\sim}{M}||. \tag{C.3.4}$$

The mapping function $\underset{\sim}{x} = \chi(\underset{\sim}{X})$ is not usually linear but its derivative at a point is linear with respect to small changes in position. A function $y = f(x)$ might be not linear, but it is always possible to construct a straight line tangent to the curve at any point and the slope of the curve is given by dy/dx. The deformation gradient tensor, $\underset{\approx}{F} = \partial x/\partial X$, plays a role in three dimensions that is analogous to the slope dy/dx in two dimensions, although it is a little bit more difficult of being visualized.

C.4 Sequentially applied deformations

Suppose that some total deformation is obtained after two separate deformations, the first one being defined by the deformation gradient tensor $\underset{\approx}{F}^{(1)}$ and the second defined by $\underset{\approx}{F}^{(2)}$. After the first deformation of the material vector $\underset{\sim}{M}$ we would have

$$\underset{\sim}{m}^{intermediate} = \underset{\approx}{F}^{(1)} \cdot \underset{\sim}{M}. \tag{C.4.5}$$

After the second deformation we would have

$$\underset{\sim}{m} = \underset{\approx}{F}^{(2)} \cdot \underset{\sim}{m}^{intermediate} = \underset{\approx}{F}^{(2)} \cdot \underset{\approx}{F}^{(1)} \cdot \underset{\sim}{M}. \tag{C.4.6}$$

Thus, the overall final deformation gradient tensor is

$$\underset{\approx}{F} = \underset{\approx}{F}^{(2)} \cdot \underset{\approx}{F}^{(1)}. \tag{C.4.7}$$

It is important to notice that the tensors are multiplied in the inverse order of application. Changing the order will result in different material deformation, as can be seen in

Figure 77 – Two deformations in different order of application.

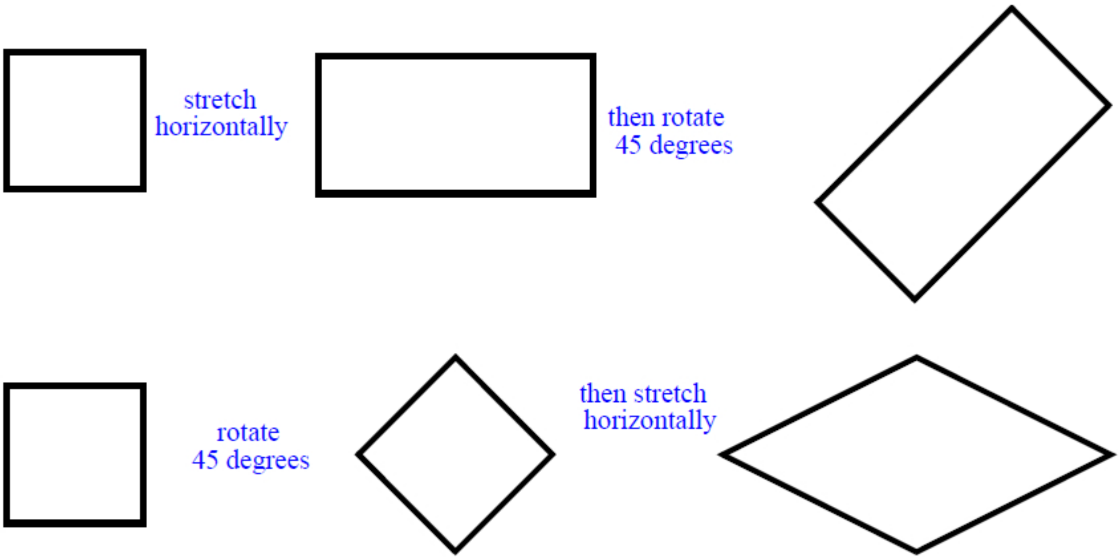

Source: Brennon (2008).

C.5 Tracking volume changes

We can calculate the volume of a undeformed element by its three infinitesimal material edge vectors, $\{\underset{\sim}{M}_1, \underset{\sim}{M}_2, \underset{\sim}{M}_3\}$. The undeformed element volume is given by the triple scalar product

$$V_0 = [\underset{\sim}{M}_1, \underset{\sim}{M}_2, \underset{\sim}{M}_3]. \tag{C.5.8}$$

The initial material vectors after the deformation will have been stretched and rotated and the new shape of the element will be represented by the deformed vectors $\{\underset{\sim}{m}_1, \underset{\sim}{m}_2, \underset{\sim}{m}_3\}$ that define the volume of the deformed element. Its new volume can be calculated by

$$V = [\underset{\sim}{m}_1, \underset{\sim}{m}_2, \underset{\sim}{m}_3]. \tag{C.5.9}$$

But noting that $\underset{\sim}{m}_k = \underset{\approx}{F} \cdot \underset{\sim}{M}_k$,

$$V = [\underset{\approx}{F} \cdot \underset{\sim}{M}_1, \underset{\approx}{F} \cdot \underset{\sim}{M}_2, \underset{\approx}{F} \cdot \underset{\sim}{M}_3]. \tag{C.5.10}$$

Expanding it out and using the definition of a determinant reveals that

$$V = (\det \underset{\approx}{F})[\underset{\sim}{M}_1, \underset{\sim}{M}_2, \underset{\sim}{M}_3] = \det \underset{\approx}{F}[V_0], \tag{C.5.11}$$

or

$$\frac{V}{V_0} = \det \underset{\approx}{F} \tag{C.5.12}$$

where J is called the "**Jacobian**" of the deformation, defined by

$$J \equiv \det \underset{\approx}{F} \tag{C.5.13}$$

In other words, the determinant of the deformation gradient is the reason of the volumes of the deformed and undeformed element. As in real life both volumes have to be positive, we may assert that

$$J > 0. \tag{C.5.14}$$

As consequence the deformation gradient tensor must be invertible. This guarantee local admissibility as discussed previously.

C.6 Precise mathematical definition of the deformation gradient

Until this point it was described a *graphical* method of approximation of the deformation gradient. Now it will be provided a quantitative definition of the deformation gradient. The deformation gradient is defined such that an infinitesimal material line segment $d\underset{\sim}{X}$ deforms into a new infinitesimal line segment $d\underset{\sim}{x}$ so that

$$\mathrm{d}\underset{\sim}{x} = \underset{\approx}{F} \cdot \mathrm{d}\underset{\sim}{X} \tag{C.6.15}$$

or, by the chain rule,

$$\underset{\approx}{F} = \frac{\mathrm{d}\underset{\sim}{x}}{\mathrm{d}\underset{\sim}{X}}. \tag{C.6.16}$$

In rectangular Cartesian coordinate system, the components of the deformation gradient tensor are

$$F_{ij} = \frac{\partial x_i}{\partial X_j}. \tag{C.6.17}$$

In matrix form,

$$\big[F\big] = \begin{bmatrix} \frac{\partial x_1}{\partial X_1} & \frac{\partial x_1}{\partial X_2} & \frac{\partial x_1}{\partial X_3} \\ \frac{\partial x_2}{\partial X_1} & \frac{\partial x_2}{\partial X_2} & \frac{\partial x_2}{\partial X_3} \\ \frac{\partial x_3}{\partial X_1} & \frac{\partial x_3}{\partial X_2} & \frac{\partial x_3}{\partial X_3} \end{bmatrix}. \tag{C.6.18}$$

C.7 Homogeneous deformation

Figure 76 represents an *inhomogeneous* deformation, in which each infinitesimal part of the body has a different deformation, consequently, a slight move in the body alters the deformation gradient.

A homogeneous deformation (Figure 78) is a very special case in which the deformation gradient has the same value in everywhere in the body. In this case Equation C.6.16 may be integrated easily resulting in the following mapping function:

$$\underset{\sim}{x} = \underset{\approx}{F} \cdot \underset{\sim}{X} + \underset{\sim}{c}, \tag{C.7.19}$$

where $\underset{\sim}{c}$ is a constant of integration representing material translation.

C.8 Strain

The deformation gradient is really interesting because it provides information about both stretch and material rotation. For one-dimensional homogeneous uniaxial deformations, the axial strain is often defined as

$$\varepsilon = \frac{L - L_0}{L} = \lambda - 1, \text{ where } \lambda = \frac{L}{L_0} \tag{C.8.20}$$

Figure 78 – Homogeneous and inhomogeneous deformation.

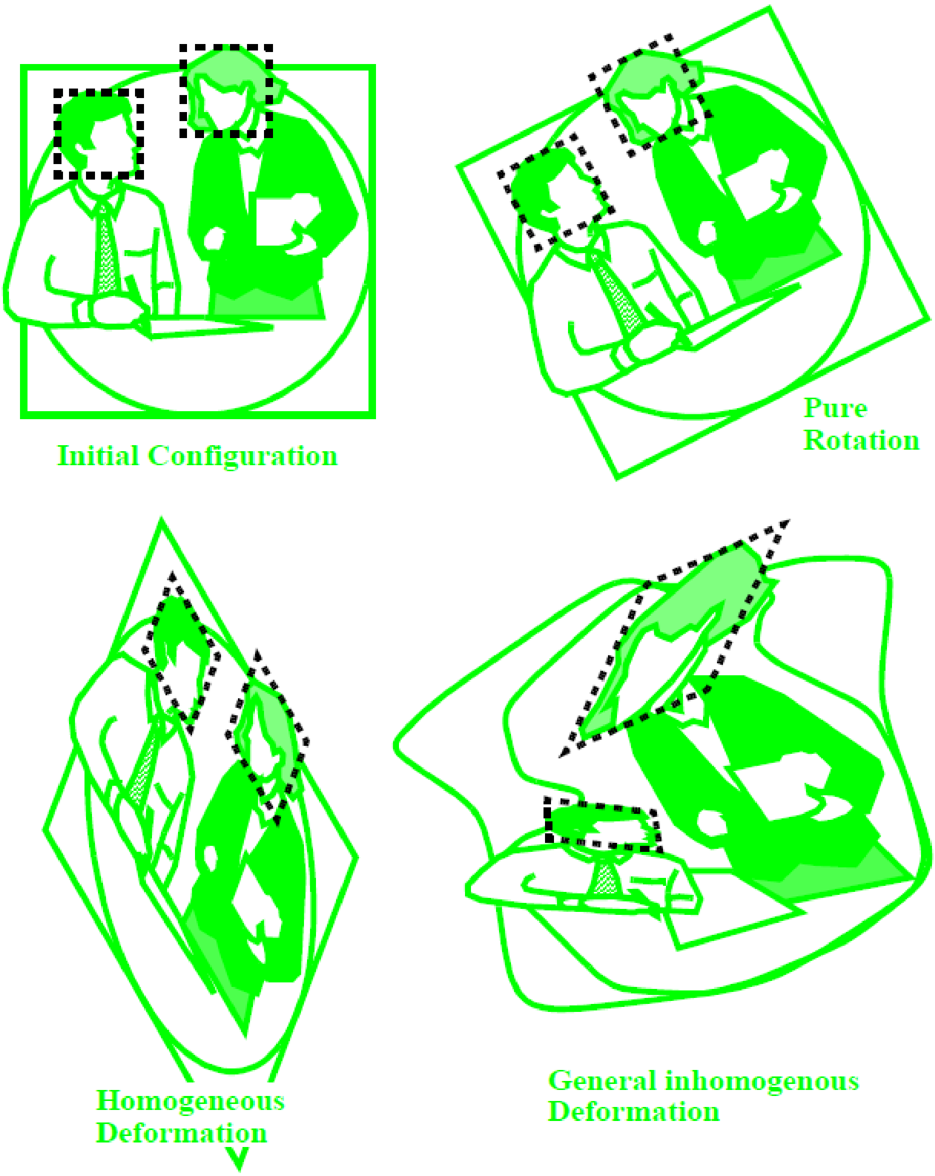

Source: Brennon (2008).

The parameter λ is called the "axial stretch". If the deformations are large it is used to measure them the following equation

$$\varepsilon = \ln(\lambda) \tag{C.8.21}$$

The only necessary parameter to describe the amount of deformation is the stretch λ. All of these strain definitions are of the general "Seth-Hill" form

$$\varepsilon = \frac{1}{k}\left[\lambda^k - 1\right] \tag{C.8.22}$$

where k is the strain definition.

When axial stretch is close to 1 , using the two-term Taylor series it is possible to notice that $\varepsilon \approx \lambda - 1$, regardless of the value of k. When $k \to 0$, $\varepsilon = \ln(\lambda)$, as can be observed in

Figure 79 – Seth-Hill family of strain measures..

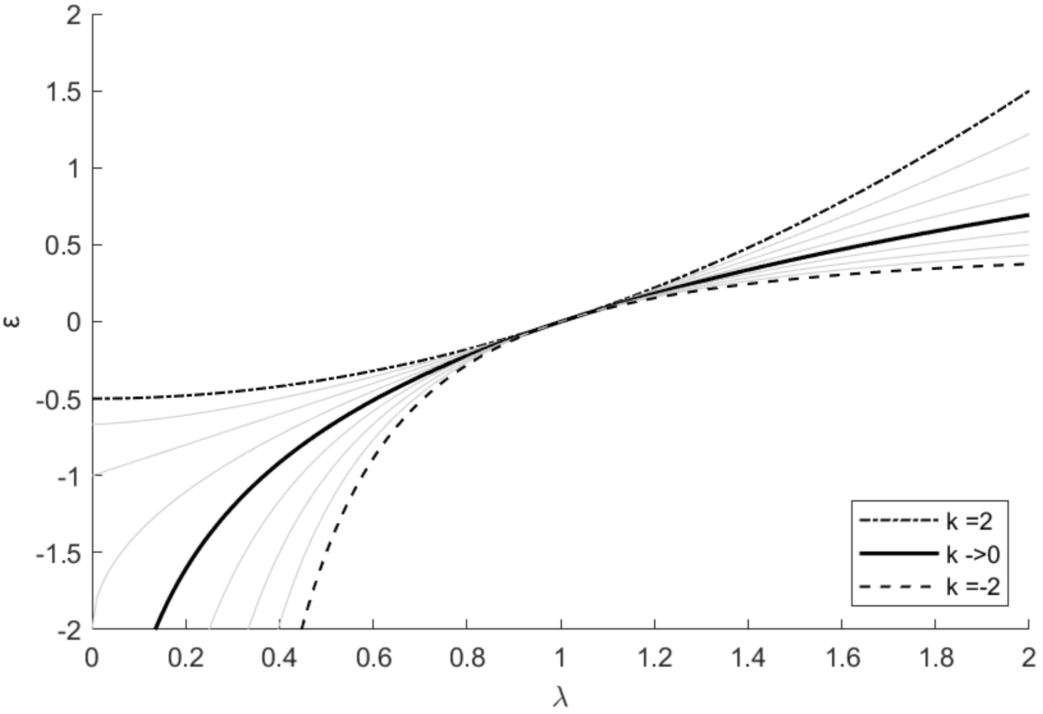

Source: from author.

Figure 79 presents different Seth-Hill parameterk. All the strain measures are negative in compression ($\lambda < 1$) and positive in tension ($\lambda > 1$). If a positive value of k is assumed, for extreme compression toward the limit as ($\lambda \to 0$) results in a finite value of strain. Physically it is expected that an infinite load is necessary to compress the material down to nothing. Consequently, if we use $k > 0$ in a linear stress-strain relationship, $\sigma = E\varepsilon$, this would imply that complete compression, which is physically impossible, would be attained with finite compression load. This is a nonphysical result and therefore a nonlinear constitutive model should be used in large deformations when using $k > 0$. The opposite occurs when we chose a negative value for the Seth-Hill parameter ($k < 0$). The logarithmic strain ($k = 0$) is the only strain choice that avoids both of these fails. But this does not mean that a material with logarithmic strain will have a linear relation stress-strain.

C.9 Strain tensors

The strain tensor may be obtained from the deformation gradient, which is a most powerful tool when we want to analyse strain and stretch. Strain tensors lose information about rotation and can always be obtained from the deformation gradient. The inverse cannot be done.

The strain tensor is symmetric and positive definite. Consequently, it is diagonal in its principal basis and all of the eigenvalues are positive. If there is no rotation (i.e., if $\underset{\approx}{R} = \underset{\approx}{I}$) any material fiber oriented in one of the i^{th} principal stretch directions will change length by a factor equal to the eigenvalue λ_i, but will not change its orientation. When there is material rotation (i.e., if $\underset{\approx}{R} \neq \underset{\approx}{I}$) then two strain definitions are possible, one that uses the reference stretch $\underset{\approx}{U}$ and one that uses the spatial stretch $\underset{\approx}{V}$ so it is possible to define a 3D generalized strain tensor upgraded from the Seth-Hill strain measure to either reference strain:

$$\underset{\approx}{\bar{\varepsilon}} = \frac{1}{k}\Big[\underset{\approx}{U}^k - \underset{\approx}{I}\Big] \tag{C.9.23}$$

or a spatial strain,

$$\underset{\approx}{\varepsilon} = \frac{1}{k}\Big[\underset{\approx}{V}^k - \underset{\approx}{I}\Big] \tag{C.9.24}$$

If $k = 0$ is used, these expressions become, in the limit,

$$\underset{\approx}{\bar{\varepsilon}} = \ln\Big[\underset{\approx}{U}\Big] \qquad \text{and} \qquad \underset{\approx}{\varepsilon} = \ln\Big[\underset{\approx}{V}\Big] \tag{C.9.25}$$

In general, for non-even powers of k, computing $\underset{\approx}{U}^k$ (or $\ln \underset{\approx}{U}$) requires the tensor $\underset{\approx}{U}$ to be expressed in its principal basis and then transforming back to the lab basis. If $[U]$ is the matrix of lab components of lab components of $\underset{\approx}{U}$ and if a matrix [Q] is constructed to contain the lab components of the orthonormalized eigenvectors of $\underset{\approx}{U}$, then

$$[U] = [Q]^T[\Lambda][Q] \tag{C.9.26}$$

where $[\Lambda]$ is the diagonal matrix containing the principal stretches associated with the principal basis. The lab components of the general Seth-Hill strain are found by

$$[\bar{\varepsilon}] = \frac{1}{k}\Big([Q]\big[\Lambda^k\big][Q]^T - [I]\Big) \tag{C.9.27}$$

If the logarithmic strain is used with respect to the lab basis we can use

$$[\bar{\varepsilon}] = [Q][\ln \Lambda][Q]^T \tag{C.9.28}$$

where $[\ln \Lambda]$ is the diagonal matrix containing the natural logs of the principal stretches.

For the logarithmic strain, the trace of matrix provides the volume strain ε_ν

$$\operatorname{tr} \bar{\underset{\approx}{\varepsilon}} = \ln(\lambda_1) + \ln(\lambda_2) + \ln(\lambda_3) = \ln(\lambda_1 \lambda_2 \lambda_3) = \ln J = \varepsilon_\nu \tag{C.9.29}$$

For large deformations this is only true for the logarithmic strain.

For pure stretch deformations, there is no difference between $\bar{\underset{\approx}{\varepsilon}}$ and $\underset{\approx}{\varepsilon}$. However, whenever there is material rotation, the spatial deformation reference strains will differ from each other by

$$\boldsymbol{\underset{\approx}{\varepsilon}} = \boldsymbol{\underset{\approx}{R}} \cdot \bar{\underset{\approx}{\varepsilon}} \cdot \boldsymbol{\underset{\approx}{R}^T} \tag{C.9.30}$$

where $\underset{\approx}{R}$ is the rotation matrix.

This distinction is of fundamental importation when working with anisotropic material constitutive laws. For these materials constitutive law considers the specifications of material orientation.

If we say that $\underset{\approx}{U} = \left(\underset{\approx}{F}^T \cdot \underset{\approx}{F}\right)^{1/2}$, Equation C.9.23 may be written as

$$\bar{\underset{\approx}{\varepsilon}} = \frac{1}{k}\left[\left(\underset{\approx}{F}^T \cdot \underset{\approx}{F}\right)^{k/2} - \underset{\approx}{I}\right] \tag{C.9.31}$$

This will always be a problem if k is not an even integer. By other side even values for the parameter k are computationally attractive because there is no need to compute the square root of a tensor. In particular, the choice $k = 2$ corresponds to the what is called the “Lagrangean strain” tensor. With this choice, the “square root” in Equation C.9.31 goes away, resulting in

$$\bar{\underset{\approx}{E}} = \frac{1}{2}\left[\underset{\approx}{F}^T \cdot \underset{\approx}{F} - \underset{\approx}{I}\right] \tag{C.9.32}$$

The Lagrange strain is a reference strain, so it may be regarded as a strain that results from the pure reference stretch prior to the rotation part of deformation. Superimpose more rotation will have no effect on Lagrange strain.

Lagrange strain can be readily computed from the deformation gradient tensor and its rate is also easily found by

$$\dot{\underset{\approx}{E}} = \frac{1}{2}\Big[\dot{\underset{\approx}{F}}^T \cdot \underset{\approx}{F} + \underset{\approx}{F}^T \cdot \dot{\underset{\approx}{F}}\Big] \tag{C.9.33}$$

Continuum mechanics states that the rate of deformation gradient is related to the material's spatial velocity gradient, $\underset{\approx}{L} \equiv \partial \underset{\sim}{v} / \partial \underset{\sim}{x}$ by

$$\dot{\underset{\approx}{F}} = \underset{\approx}{L} \cdot \underset{\approx}{F} \tag{C.9.34}$$

Therefore Equation C.9.33 may be written by

$$\dot{\underset{\approx}{E}} = \underset{\approx}{F}^T \cdot D \cdot \underset{\approx}{F}, \qquad \text{where} \qquad \underset{\approx}{D} \equiv \frac{1}{2}\Big[\underset{\approx}{L} + \underset{\approx}{L}^T\Big] \tag{C.9.35}$$

The tensor $\underset{\approx}{D}$ is often called the "rate of deformation," which is an unfortunate and misleading name because, despite having some rate-like properties, it is not the proper rate of any tensor. By this, we mean that it is possible to construct closed deformation paths for which the time integral of $\underset{\approx}{D}$ is not zero. Frequently in mechanics, it is useful to introduce a general "unrotation" operation, denoted by an overbar, and defined for any spatial second-order tensor $\underset{\approx}{Y}$ by

$$\bar{\underset{\approx}{Y}} = \underset{\approx}{R}^T \cdot D \cdot \underset{\approx}{R} \tag{C.9.36}$$

Using the overbar notation we can write

$$\dot{\underset{\approx}{E}} = \bar{\underset{\approx}{V}} \cdot \bar{\underset{\approx}{D}} \cdot \bar{\underset{\approx}{V}} \tag{C.9.37}$$

where

$$\bar{\underset{\approx}{D}} = \underset{\approx}{R}^T \cdot \underset{\approx}{D}\underset{\approx}{R} \tag{C.9.38}$$

and

$$\bar{\underset{\approx}{V}} = \underset{\approx}{F}^T \cdot \underset{\approx}{R} = \underset{\approx}{R}^T \cdot \underset{\approx}{V} \cdot \underset{\approx}{R} = \underset{\approx}{U} \tag{C.9.39}$$

C.10 Finite element stretching

In finite element method the mapping is made transforming a quadrilateral element into a square with two logical coordinates in space defined by two parameters η_1 and η_2. Both parameters vary from -1 to 1 or from 0 to 1, depending on the problem. The four vertices of the quadrilateral in physical space must be known.

Figure 80 – Quadrilateral mapping.

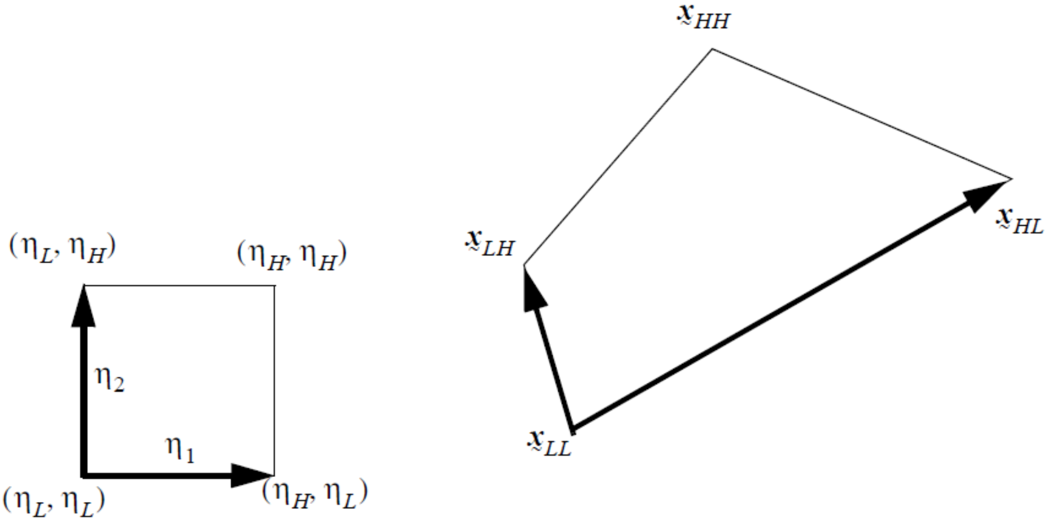

Source: Brennon (2008).

As an example let's denote the four vertices in their physical position by $\{\underset{\sim}{x}_{LL}, \underset{\sim}{x}_{HH}, \underset{\sim}{x}_{LH}, \underset{\sim}{x}_{HL}\}$, with the subscripts H and L meaning "high" an "low", respectively. We would have the following situation to be mapped as presented in Figure 80.

To find any point in the interior of the isoparametric element in function of $qty(\eta_1, \eta_2)$, we can use

$$\begin{aligned}\underset{\sim}{x}(\eta_1,\eta_2) =& \left(\frac{\eta_H-\eta_1}{\eta_H-\eta_L}\right)\left(\frac{\eta_H-\eta_2}{\eta_H-\eta_L}\right)\underset{\sim}{x}_{LL} + \left(\frac{\eta_H-\eta_1}{\eta_H-\eta_L}\right)\left(\frac{\eta_L-\eta_2}{\eta_L-\eta_H}\right)\underset{\sim}{x}_{LH} + \\ & \left(\frac{\eta_L-\eta_1}{\eta_L-\eta_H}\right)\left(\frac{\eta_H-\eta_2}{\eta_H-\eta_L}\right)\underset{\sim}{x}_{HL} + \left(\frac{\eta_L-\eta_1}{\eta_L-\eta_H}\right)\left(\frac{\eta_L-\eta_2}{\eta_L-\eta_H}\right)\underset{\sim}{x}_{HH}\end{aligned} \tag{C.10.40}$$

Considering an example where η ranges from $\eta_L = 0$ to $\eta_H = 1$, this becomes

$$\begin{aligned}\underset{\sim}{x}(\eta_1,\eta_2) =& (1-\eta_1)(1-\eta_2)\underset{\sim}{x}_{LL} + (1-\eta_1)(\eta_2)\underset{\sim}{x}_{LH} \\ & + (\eta_1)(1-\eta_2)\underset{\sim}{x}_{HL} + (\eta_1)(\eta_2)\underset{\sim}{x}_{HH}\end{aligned} \tag{C.10.41}$$

In this case, we may define

$$\underset{\sim}{g}_1 = \frac{\partial \underset{\sim}{x}}{\partial \eta_1} = (\underset{\sim}{x}_{HL} - \underset{\sim}{x}_{LL})(1-\eta_2) + (\underset{\sim}{x}_{HH} - \underset{\sim}{x}_{LH})\eta_2 \tag{C.10.42}$$

$$\underset{\sim}{g}_2 = \frac{\partial \underset{\sim}{x}}{\partial \eta_2} = (\underset{\sim}{x}_{LH} - \underset{\sim}{x}_{LL})(1-\eta_1) + (\underset{\sim}{x}_{HH} - \underset{\sim}{x}_{HL})\eta_1 \tag{C.10.43}$$

and the deformation gradient associated with the mapping may be expressed by

$$\frac{\mathrm{d}\underset{\sim}{x}}{\mathrm{d}\underset{\sim}{\eta}} = \frac{\partial \underset{\sim}{x}}{\partial \eta_1}\frac{\partial \eta_1}{\partial \underset{\sim}{\eta}} + \frac{\partial \underset{\sim}{x}}{\partial \eta_2}\frac{\partial \eta_2}{\partial \underset{\sim}{\eta}} = \underset{\sim}{g}_1\underset{\sim}{e}_1 + \underset{\sim}{g}_2\underset{\sim}{e}_2 \tag{C.10.44}$$

The mapping above may be used to describe either the spatial or reference configuration for an actual deformation. In that case, the actual reference configuration has vectors $\underset{\sim}{G}_1$ and $\underset{\sim}{G}_2$, defined similarly to the g-vectors above. Then the actual deformation gradient may be expressed by

$$\underset{\approx}{F} = \underset{\sim}{g}_1\underset{\sim}{G}^1 + \underset{\sim}{g}_2\underset{\sim}{G}^2 \tag{C.10.45}$$

For practical reasons it is usually present by

$$\left[\underset{\approx}{F}\right] = [g][G]^{-1}, \tag{C.10.46}$$

where the matrix $[g]$ contains $\underset{\sim}{g}_1$ and $\underset{\sim}{g}_2$ in its columns and $[G]$ contains $\underset{\sim}{G}_1$ and $\underset{\sim}{G}_2$ in its columns.

APPENDIX D – CALCULATED HONEYCOMB PARAMETERS

The calculated values of the honeycomb are presented below[1]:

RO: 2.9e-9
E=70
PR=0.33
SIGY=1e-4
VF=0.0
MU=0.05
EAAU=EBBU=0.07
ECCU=0.001
GABU=GBCU=GCAU=0.04

For the LCA it was used the following curve (in LS-Dyna pattern):

Curveplot
20200609 - Pedestrian safety
Abscissa
Ordinate
Define Curve
Curve 10000032 # pts=42
* Minval= 0.0000000000e+00 at time= 0.0000000000
* Maxval= 1.0000000000e+01 at time= 1.0000000000
0.0000000000e+00 0.0000000000e+00
2.2345799953e-02 2.2559700301e-04
4.4580999762e-02 1.4494700008e-04
6.6927403212e-02 1.2244899699e-04
8.9273698628e-02 1.4289100363e-04
1.1162009835e-01 1.3105699327e-04
1.3396650553e-01 1.2547700317e-04
1.5631289780e-01 1.3231100456e-04
1.7866480350e-01 1.2295300257e-04
2.0101119578e-01 1.2148699898e-04
2.2335749865e-01 1.2306000281e-04
2.4570390582e-01 1.2682500528e-04
2.6805031300e-01 1.2385100126e-04
2.9039669037e-01 1.2882000010e-04
3.1274300814e-01 1.3878999744e-04

---

[1] All dimensions are based on the basis millimeter, kilogram and milliseconds

```
3.3508938551e-01 1.3864299399e-04
3.5743579268e-01 1.3253699581e-04
3.7978211045e-01 1.3941200450e-04
4.0223461390e-01 1.4167299378e-04
4.2457538843e-01 1.3605700224e-04
4.4692179561e-01 1.3025199587e-04
4.6926259995e-01 1.3263699657e-04
4.9160331488e-01 1.3973600289e-04
5.1394981146e-01 1.3732700609e-04
5.3629052639e-01 1.3175199274e-04
5.5863130093e-01 1.2687699927e-04
5.8094972372e-01 1.1944099970e-04
6.0329610109e-01 1.0792700050e-04
6.2564247847e-01 1.1303499923e-04
6.4798879623e-01 1.2814599904e-04
6.7033517361e-01 1.3411199325e-04
6.9268161058e-01 1.3978600327e-04
7.1502792835e-01 1.5095599520e-04
7.3737430573e-01 1.6944699746e-04
7.5972068310e-01 2.1336700593e-04
7.8206700087e-01 2.8629601002e-04
8.0441337824e-01 3.5818299511e-04
8.2675981522e-01 4.4851898565e-04
8.4916198254e-01 5.7331001153e-04
8.7150841951e-01 7.9302699305e-04
8.9385467768e-01 1.1741999770e-03
1.0000000000e+00 1.0000000000e+01
endcurve
```

For the LCB and LCC it was used the following curve (in LS-Dyna pattern):

```
Curveplot
20200609 - Pedestrian safety
Abscissa
Ordinate
Define Curve
Curve 10000033 pts=42
* Minval= 0.0000000000e+00 at
time= 0.0000000000
* Maxval= 5.0000000000e-01 at
```

```
time= 1.0000000000
0.0000000000e+00 0.0000000000e+00
2.2345799953e-02 1.1279850696e-05
4.4580999762e-02 7.2473499131e-06
6.6927403212e-02 6.1224500314e-06
8.9273698628e-02 7.1445501817e-06
1.1162009835e-01 6.5528497544e-06
1.3396650553e-01 6.2738504312e-06
1.5631289780e-01 6.6155503191e-06
1.7866480350e-01 6.1476503106e-06
2.0101119578e-01 6.0743500399e-06
2.2335749865e-01 6.1530004132e-06
2.4570390582e-01 6.3412503550e-06
2.6805031300e-01 6.1925502450e-06
2.9039669037e-01 6.4410000959e-06
3.1274300814e-01 6.9395000537e-06
3.3508938551e-01 6.9321499723e-06
3.5743579268e-01 6.6268498813e-06
3.7978211045e-01 6.9706002250e-06
4.0223461390e-01 7.0836499617e-06
4.2457538843e-01 6.8028502938e-06
4.4692179561e-01 6.5126000663e-06
4.6926259995e-01 6.6318498284e-06
4.9160331488e-01 6.9868001447e-06
5.1394981146e-01 6.8663503043e-06
5.3629052639e-01 6.5875997279e-06
5.5863130093e-01 6.3438501456e-06
5.8094972372e-01 5.9720500758e-06
6.0329610109e-01 5.3963499340e-06
6.2564247847e-01 5.6517501434e-06
6.4798879623e-01 6.4073001340e-06
6.7033517361e-01 6.7055998443e-06
6.9268161058e-01 6.9893003456e-06
7.1502792835e-01 7.5477996688e-06
7.3737430573e-01 8.4723496911e-06
7.5972068310e-01 1.0668350114e-05
7.8206700087e-01 1.4314800865e-05
8.0441337824e-01 1.7909149392e-05
8.2675981522e-01 2.2425949282e-05
```

```
8.4916198254e-01 2.8665501304e-05
8.7150841951e-01 3.9651349653e-05
8.9385467768e-01 5.8710000303e-05
1.0000000000e+00 5.0000000000e-01
endcurve
```

APPENDIX E – LS-DYNA USED MATERIALS

```
$# LS-DYNA Keyword file created by LS-PrePost(R) V4.6.22 - 12Nov2019
$# Created on May-19-2021 (10:20:48)
KEYWORD
MAT_ELASTIC
$HMNAME MATERIALS 10000000steel
$# mid ro e pr da db not used
100000007.90000E-6 210.0 0.3 0.0 0.0 0.0
MAT_JOHNSON_COOK_TITLE
Steel JC DP1000
$# mid ro g e pr dtf vp rateop
100000047.80000E-6 79.3 210.0 0.3 0.0 0.0 0.0
$# a b n c m tm tr epso
0.6736 1.303 0.4217 0.0168 -9999.0 1370.0 273.0 0.001
$# cp pc spall it d1 d2 d3 d4
120.0 0.0 2.0 0.0 0.0 0.0 0.0 0.0
$# d5 c2/p erod efmin numint
0.0 0.0 01.00000E-6 0.0
MAT_JOHNSON_COOK_TITLE
Steel JC DP1000.1
$# mid ro g e pr dtf vp rateop
100000057.80000E-6 79.3 210.0 0.3 0.0 0.0 0.0
$# a b n c m tm tr epso
0.6736 1.303 0.4217 0.0168 -9999.0 1370.0 273.0 0.001
$# cp pc spall it d1 d2 d3 d4
120.0 0.0 2.0 0.0 0.0 0.0 0.0 0.0
$# d5 c2/p erod efmin numint
0.0 0.0 01.00000E-6 0.0
```

```
MAT_JOHNSON_COOK_TITLE
Aluminium JC
$# mid ro g e pr dtf vp rateop
100000062.70000E-6 24.0 71.0 0.33 0.0 0.0 0.0
$# a b n c m tm tr epso
0.021131 0.133 0.169 0.0305 1.393 1000.0 273.0 0.001
$# cp pc spall it d1 d2 d3 d4
120.0 -0.3 2.0 0.0 0.0 0.0 0.0 0.0
$# d5 c2/p erod efmin numint
0.0 0.0 01.00000E-6 0.0
MAT_JOHNSON_COOK
$HMNAME MATERIALS 10000007aluminium
$# mid ro g e pr dtf vp rateop
100000072.73000E-6 0.0 0.0 0.0 0.0 0.0 0.0
$# a b n c m tm tr epso
0.0 0.0 0.0 0.0 0.0 0.0 0.0 0.0
$# cp pc spall it d1 d2 d3 d4
0.0 0.0 2.0 0.0 0.0 0.0 0.0 0.0
$# d5 c2/p erod efmin numint
0.0 0.0 01.00000E-6 0.0
MAT_RIGID_TITLE
mat_rigid
$# mid ro e pr n couple m alias
100000081.00000E-6 210.0 0.3 0.0 0.0 0.0
$# cmo con1 con2
0.0 0 0
$#lco or a1 a2 a3 v1 v2 v3
0.0 0.0 0.0 0.0 0.0 0.0
MAT_PIECEWISE_LINEAR_PLASTICITY_TITLE
window_polymer
```

```
$# mid ro e pr sigy etan fail tdel
100000161.00000E-6 0.25 0.35 0.01 0.001 2.5 0.0
$# c p lcss lcsr vp
0.0 0.0 0 0 0.0
$# eps1 eps2 eps3 eps4 eps5 eps6 eps7 eps8
0.0 0.0 0.0 0.0 0.0 0.0 0.0 0.0
$# es1 es2 es3 es4 es5 es6 es7 es8
0.0 0.0 0.0 0.0 0.0 0.0 0.0 0.0
MAT_LOW_DENSITY_FOAM
$HMNAME MATERIALS 10000019MATL57_60064101
$# mid ro e lcid tc hu beta damp
100000196.41000E-8 0.00199 10000027 0.0 0.01 0.0 0.0
$# shape fail bvflag ed beta1 kcon ref
3.0 0.0 0.0 0.0 0.0 0.0 0.0
MAT_LOW_DENSITY_FOAM
$HMNAME MATERIALS 10000020MATL57_60026101
$# mid ro e lcid tc hu beta damp
100000202.56000E-8 0.01144 10000026 0.0 0.01 0.0 0.0
$# shape fail bvflag ed beta1 kcon ref
3.0 0.0 0.0 0.0 0.0 0.0 0.0
MAT_SIMPLIFIED_JOHNSON_COOK_TITLE
steel simplified JC
$# mid ro e pr vp
100000237.90000E-5 210.0 0.3 0.0
$# a b n c psfail sigmax sigsat epso
0.6736 1.303 0.4217 0.01681.00000E171.00000E281.00000E28 0.001
MAT_SPOTWELD
$HMNAME MATERIALS 10000024weld
$# mid ro e pr sigy eh dt tfail
100000247.80000E-6 210.0 0.3 0.5 210000.0 0.0 0.0
```

```
$# efail nrr nrs nrt mrr mss mtt nf
0.0 0.0 0.0 0.0 0.0 0.0 0.0 0.0
MAT_MODIFIED_PIECEWISE_LINEAR_PLASTICITY_TITLE
window
$# mid ro e pr sigy etan fail tdel
100000262.50000E-6 70.0 0.22 0.03 1.0 0.1 0.0
$# c p lcss lcsr vp epsthin epsmaj numint
0.0 0.0 0 0 0.0 0.0 0.0 1.0
$# eps1 eps2 eps3 eps4 eps5 eps6 eps7 eps8
0.0 0.0 0.0 0.0 0.0 0.0 0.0 0.0
$# es1 es2 es3 es4 es5 es6 es7 es8
0.0 0.0 0.0 0.0 0.0 0.0 0.0 0.0
MAT_SPRING_ELASTIC
$HMNAME MATERIALS 10000027MATSD1_30000012
$# mid k
10000027 0.001
MAT_SEATBELT_TITLE
seat belt 1D
$# mid mpul llcid ulcid lmin cse damp e
100000295.97000E-4 10000016 10000017 2.0 0.0 0.0 0.0
MAT_MODIFIED_HONEYCOMB
$HMNAME MATERIALS 10000030honeycomb
$# mid ro e pr sigy vf mu bulk
100000302.90000E-8 70.0 0.331.00000E-4 0.0 0.05 0.0
$# lca lcb lcc lcs lcab lcbc lcca lcsr
10000032 10000033 10000033 10000034 10000034 10000034 10000034 0
$# eaau ebbu eccu gabu gbcu gcau aopt macf
0.14 0.14 0.0 0.0 0.0 0.0 0.0 1
$# xp yp zp a1 a2 a3
0.0 0.0 0.0 0.0 0.0 0.0
```

```
$# d1 d2 d3 tsef ssef vref tref shdflg
0.0 0.0 0.0 0.0 0.0 0.0 0.0 0.0
MAT_HONEYCOMB_TITLE
material1
$# mid ro e pr sigy vf mu bulk
100000312.90000E-8 70.0 0.331.00000E-4 0.0 0.05 0.0
$# lca lcb lcc lcs lcab lcbc lcca lcsr
10000032 10000033 10000033 10000035 0 0 10000036 0
$# eaau ebbu eccu gabu gbcu gcau aopt macf
0.07 0.07 0.001 0.04 0.04 0.04 0.0 1
$# xp yp zp a1 a2 a3
0.0 0.0 0.0 0.0 0.0 0.0
$# d1 d2 d3 tsef ssef v1 v2 v3
0.0 0.0 0.0 0.0 0.0 0.0 0.0 0.0
END
```

APPENDIX F – CAD DRAWINGS

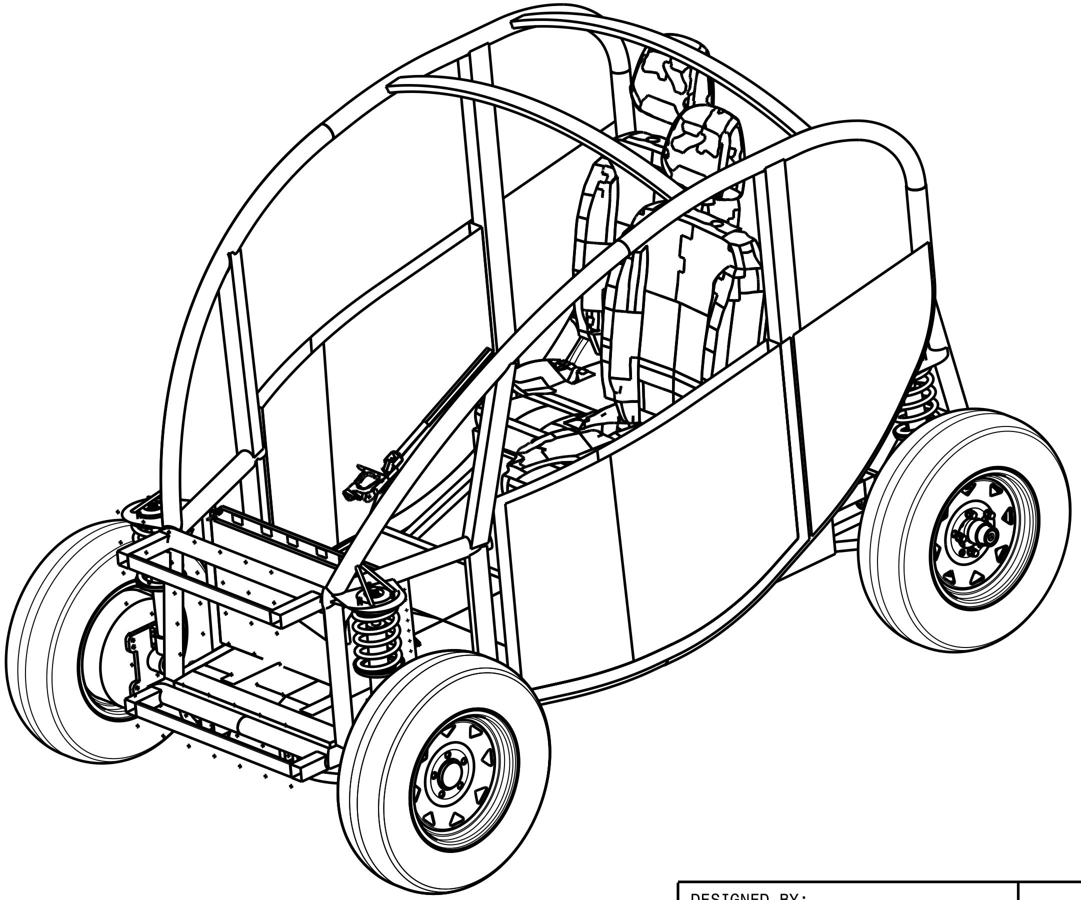

DESIGNED BY:
MRG Duarte
DATE: 3/16/2021

SUPERVISOR
M ALVES

AUS - AUTOMOVEL URBANO SEGURO

SIZE
A4

ISOMETRIC VIEW

SCALE
1:10

DRAWING NUMBER
01

SHEET
1/22

Number	Quantity	Thickness
1	2	1.00
2	2	1.00
3	2	0.25

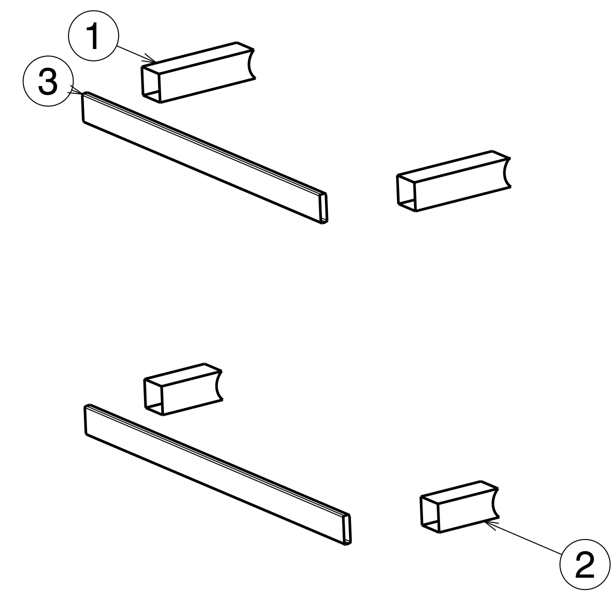

ISO SCALE 1:10

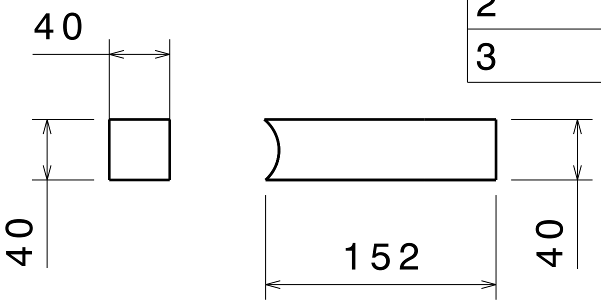

Piece 1

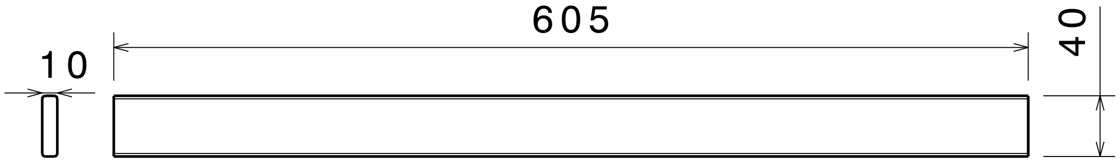

Piece 3

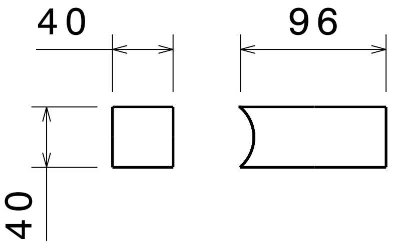

Piece 2

DESIGNED BY:
MRG DUARTE
DATE:
3/16/2021
ADVISOR:
M ALVES

AUS - AUTOMOVEL URBANO SEGURO

BUMPER

SIZE
A4

SCALE
1:5

WEIGHT (kg)
1.90

DRAWING NUMBER
02

SHEET
2/22

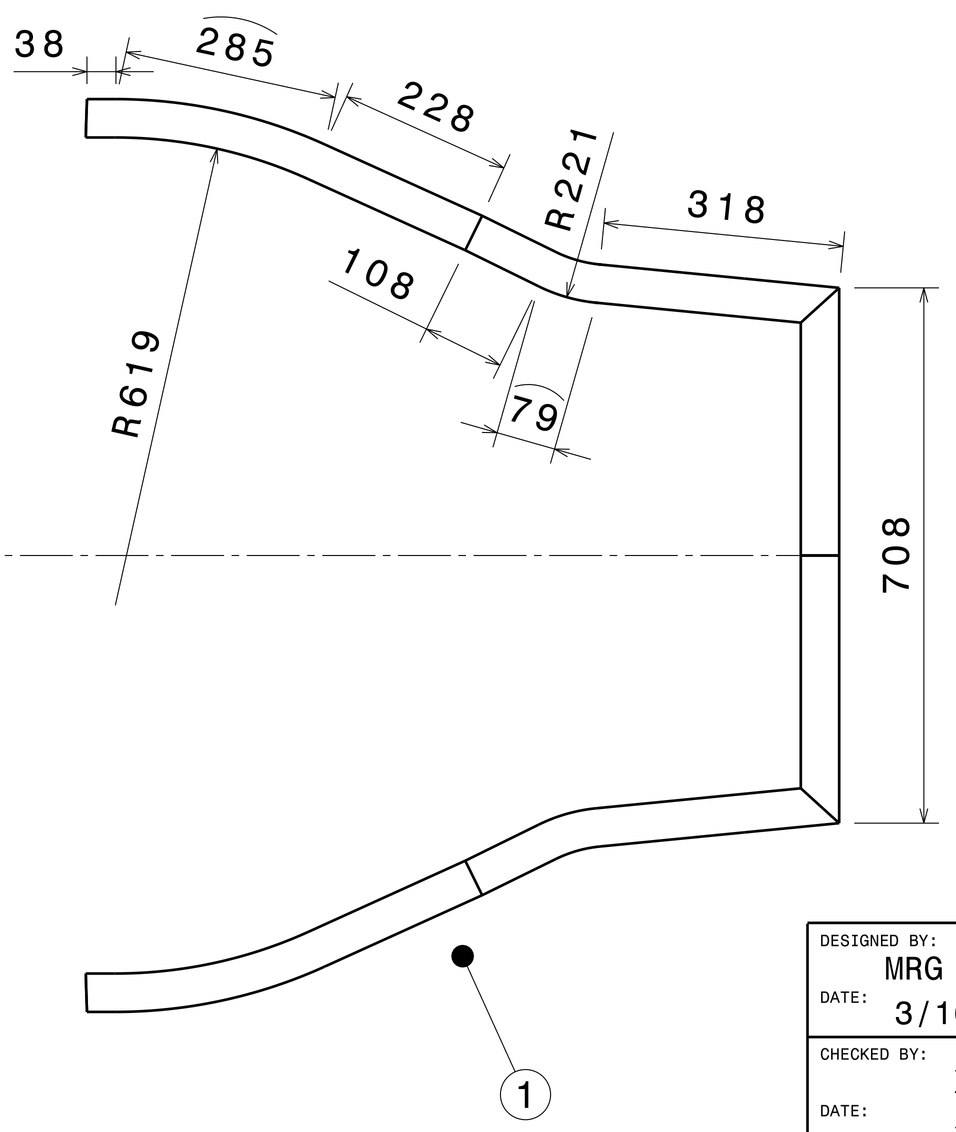

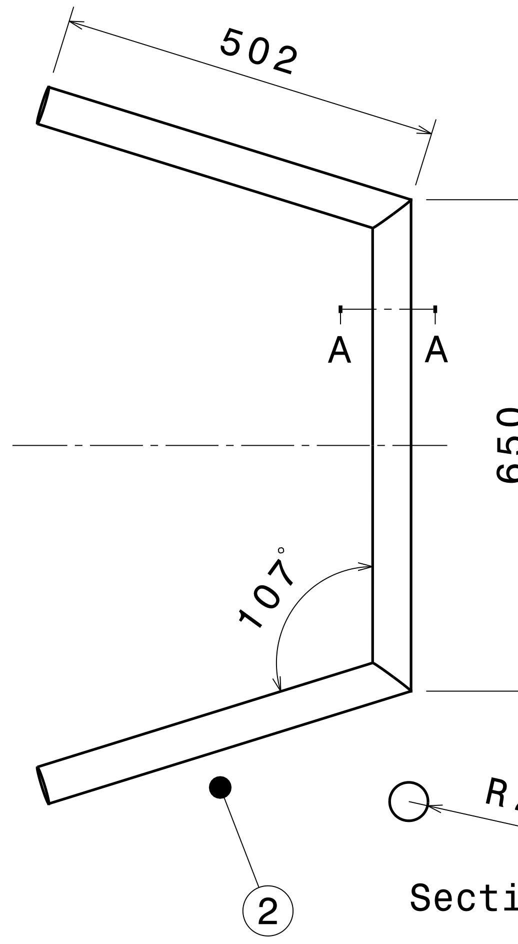

NUMBER	DIAMETER	THICKNESS
1	2 IN	1.4
2	2 IN	1.4

DESIGNED BY: MRG Duarte
DATE: 3/16/2021
CHECKED BY: XXX
DATE: XXX

AUS - AUTOMOVEL URBANO SEGURO

FRONT STRUCTURES

SIZE: A4
SCALE: 1:10
DRAWING NUMBER: 03
SHEET: 3/22

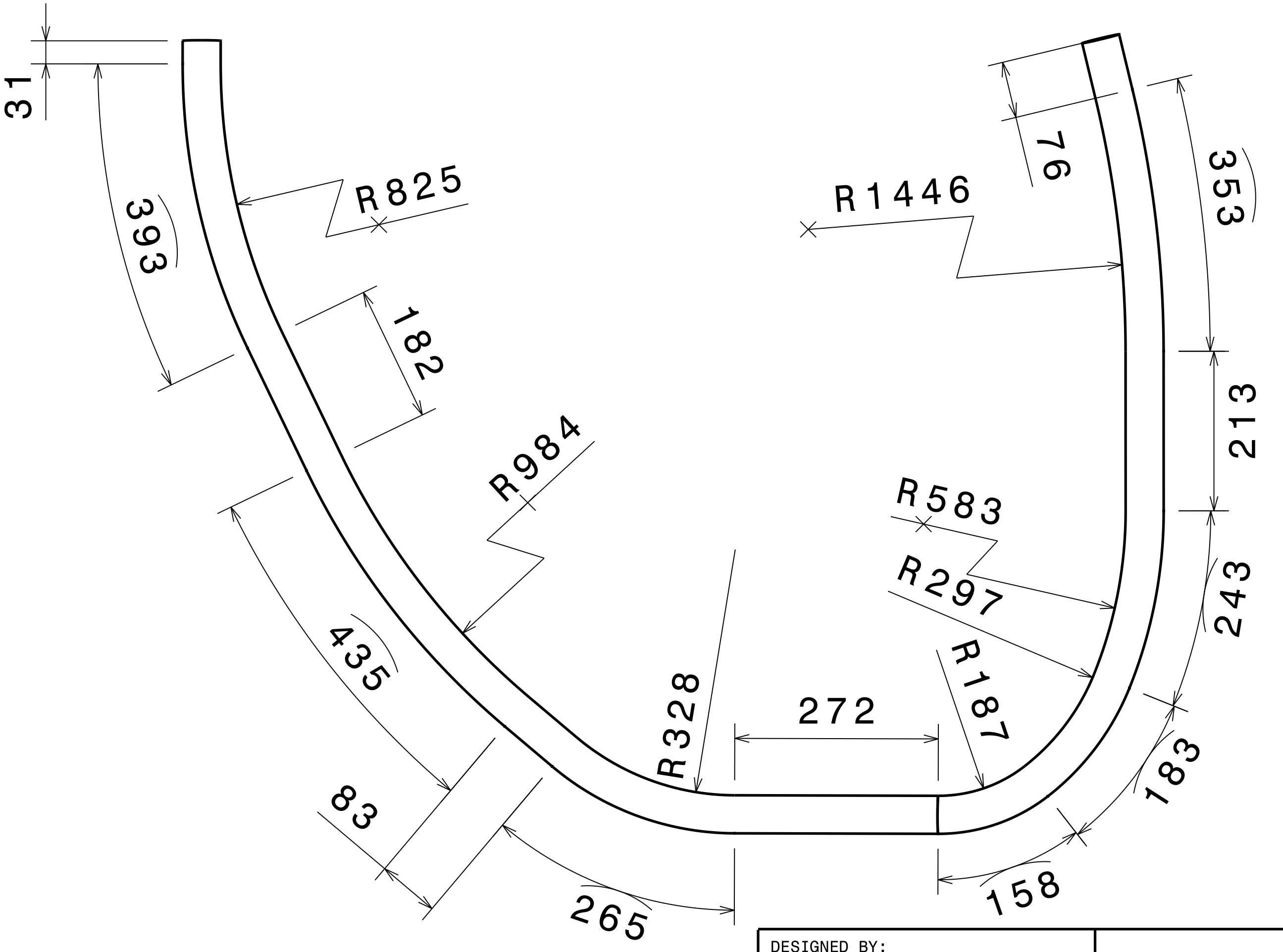

BILL OF MATERIALS		
QUANTITY	DIAMETER	THICKNESS
2	2 in	1.2

DESIGNED BY:
MRG Duarte
DATE: 3/16/2021

SUPERVISOR
M ALVES

AUS - AUTOMOVEL URBANO SEGURO

SIZE
A4

VEHICLE SIDE (LEFT/RIGHT)

SCALE
1:10

DRAWING NUMBER
04

SHEET
4/22

BILL OF MATERIALS		
QUANTITY	DIAMETER	THICKNESS
2	2 in	1.2

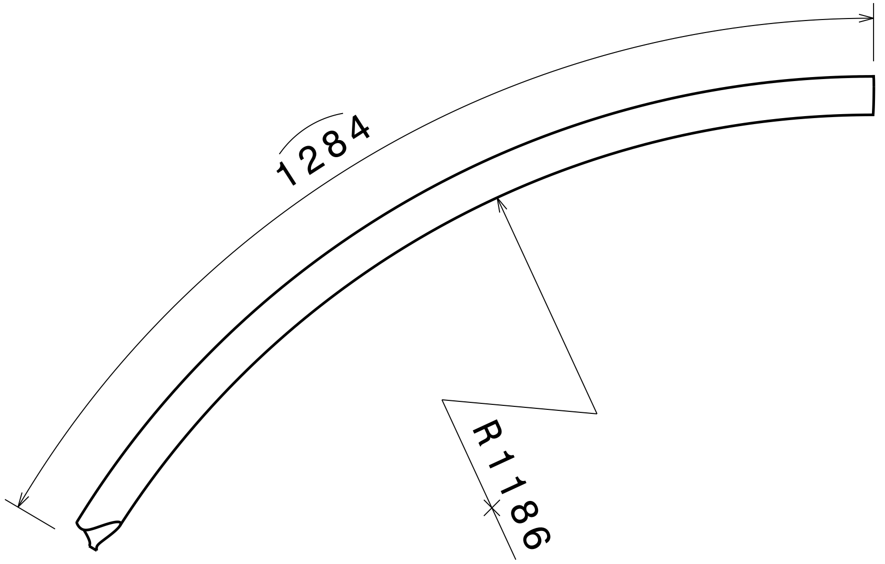

DESIGNED BY:
MRG Duarte
DATE: 3/16/2021

SUPERVISOR
M ALVES

AUS - AUTOMOVEL URBANO SEGURO

SIZE
A4

VEHICLE SIDE (LEFT/RIGHT)

SCALE
1:10

DRAWING NUMBER
01

SHEET
5/22

BILL OF MATERIALS			
ITEM	QUANTITY	DIAMETER	THICKNESS
1	2	2 in	1.0
2	2	2 in	1.0

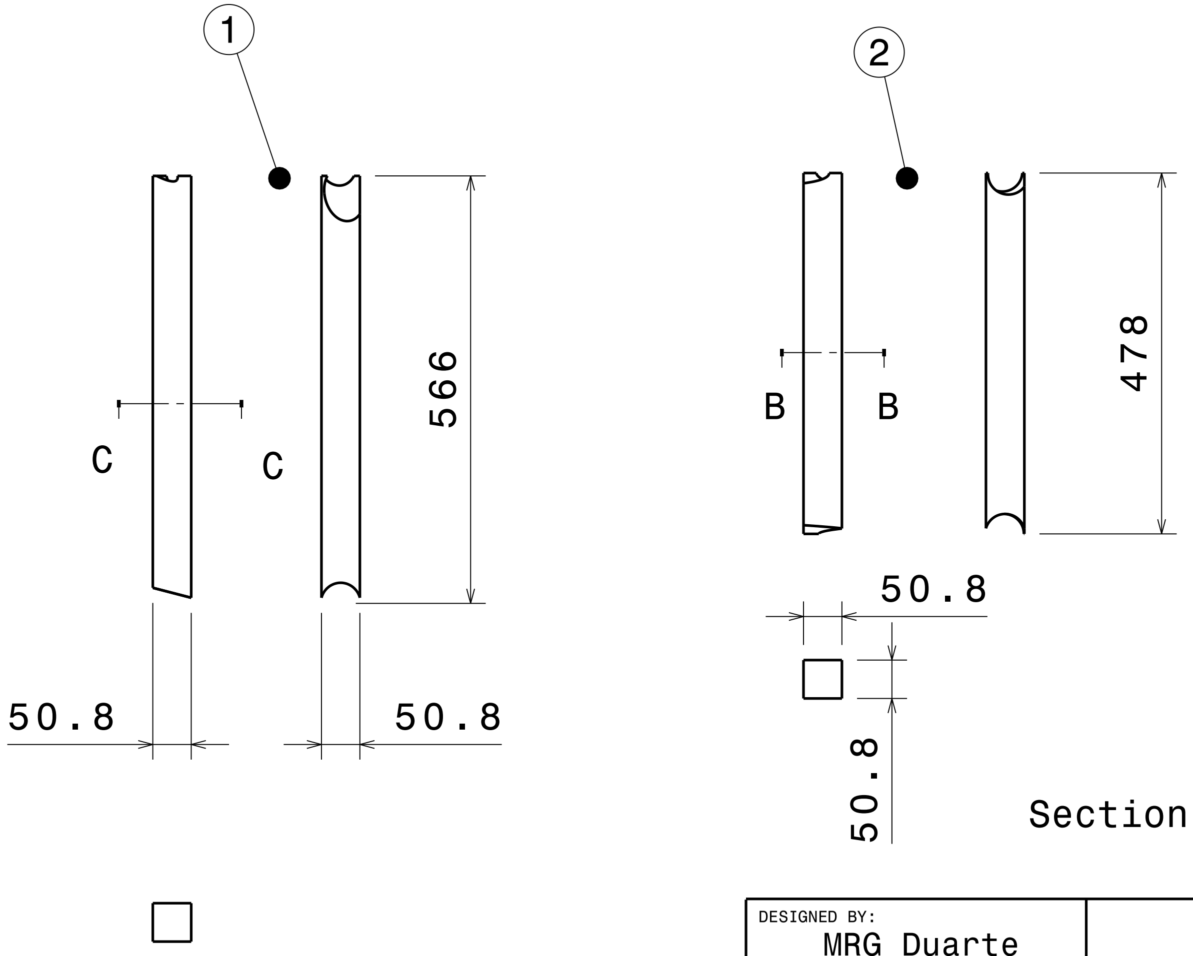

Section cut C-C

DESIGNED BY:
MRG Duarte
DATE: 3/16/2021

SUPERVISOR
M ALVES

AUS - AUTOMOVEL URBANO SEGURO

SIZE
A4

COLUMN A (LEFT/RIGHT)

SCALE
1:10

DRAWING NUMBER
ColunaA3

SHEET
6/22

BILL OF MATERIALS			
ITEM	QUANTITY	DIAMETER	THICKNESS
1	2	2 in	1.2
2	2	2 in	1.2

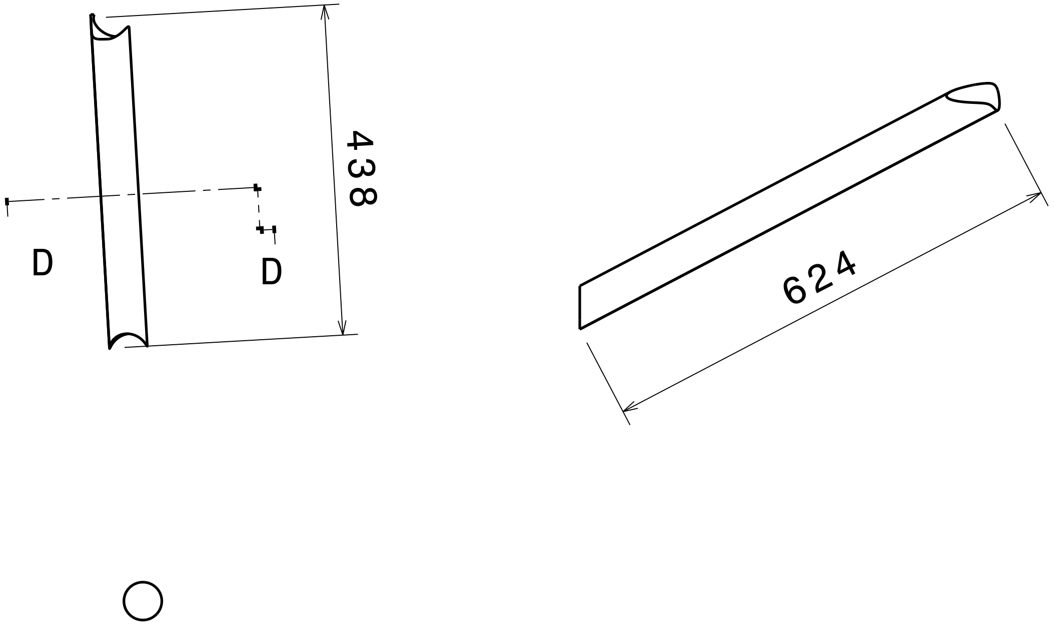

Section cut D-D
Scale: 1:10

DESIGNED BY: MRG Duarte
DATE: 3/16/2021
SUPERVISOR M ALVES
SIZE A4
SCALE 1:10

AUS - AUTOMOVEL URBANO SEGURO

FRONT AND BACK BEAMS

DRAWING NUMBER 01
SHEET 7/22

BILL OF MATERIALS		
ITEM	QUANTITY	THICKNESS
1	2	1.2

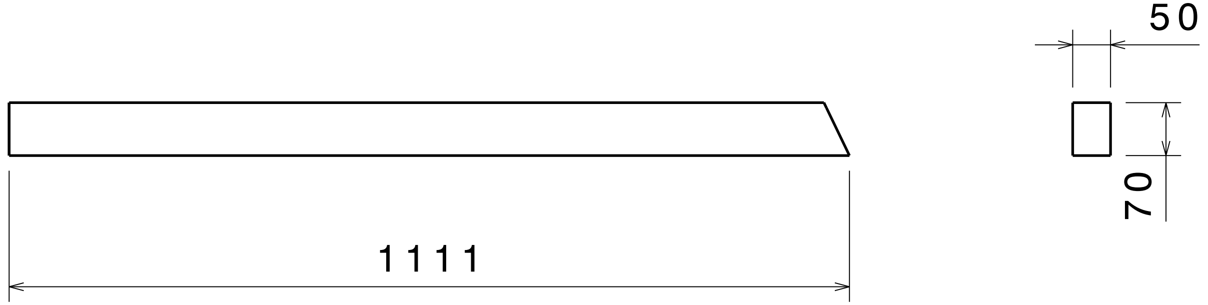

Front view
Scale: 1:10

DESIGNED BY: MRG Duarte
DATE: 3/16/2021
SUPERVISOR M ALVES

AUS - AUTOMOVEL URBANO SEGURO

COLUMN B (RIGHT ND LEFT)

SIZE A4
SCALE 1:10
DRAWING NUMBER 01
SHEET 8/22

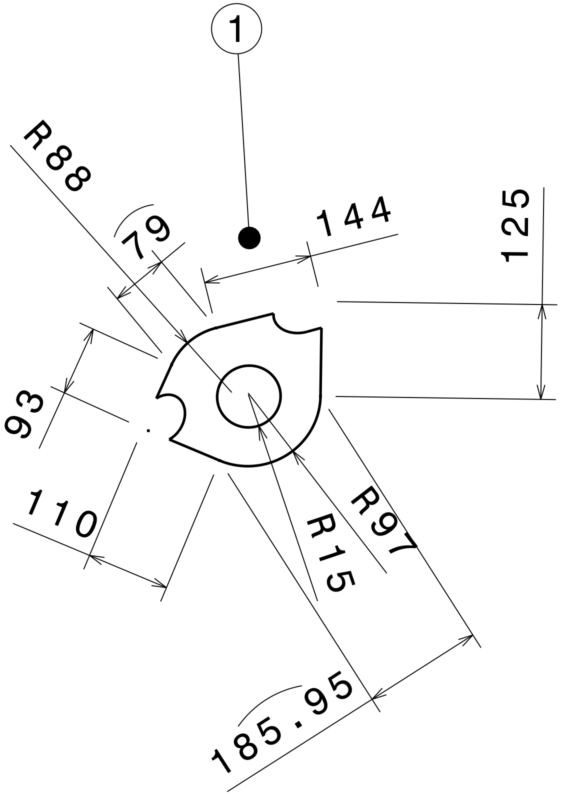

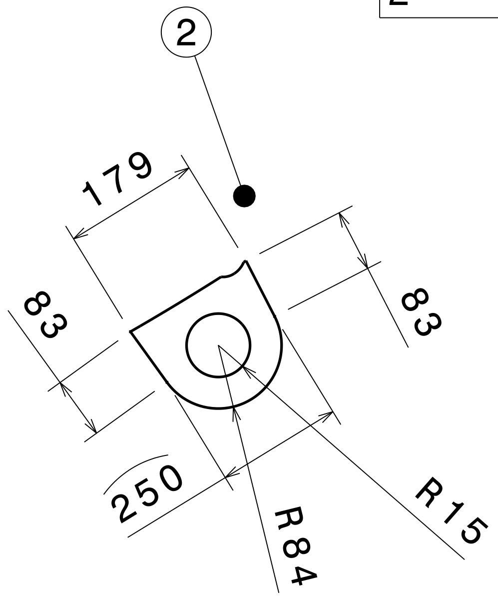

BILL OF MATERIALS		
ITEM	QUANTITY	THICKNESS
1	2	2.0
2	2	2.0

DESIGNED BY:
MRG Duarte
DATE: 3/16/2021

SUPERVISOR
M ALVES

AUS - AUTOMOVEL URBANO SEGURO

SIZE
A4

SHOCK ABSORBER PLATES

SCALE
1:10

DRAWING NUMBER
01

SHEET
9/22

BILL OF MATERIALS		
ITEM	QUANTITY	THICKNESS
1	2	1.2

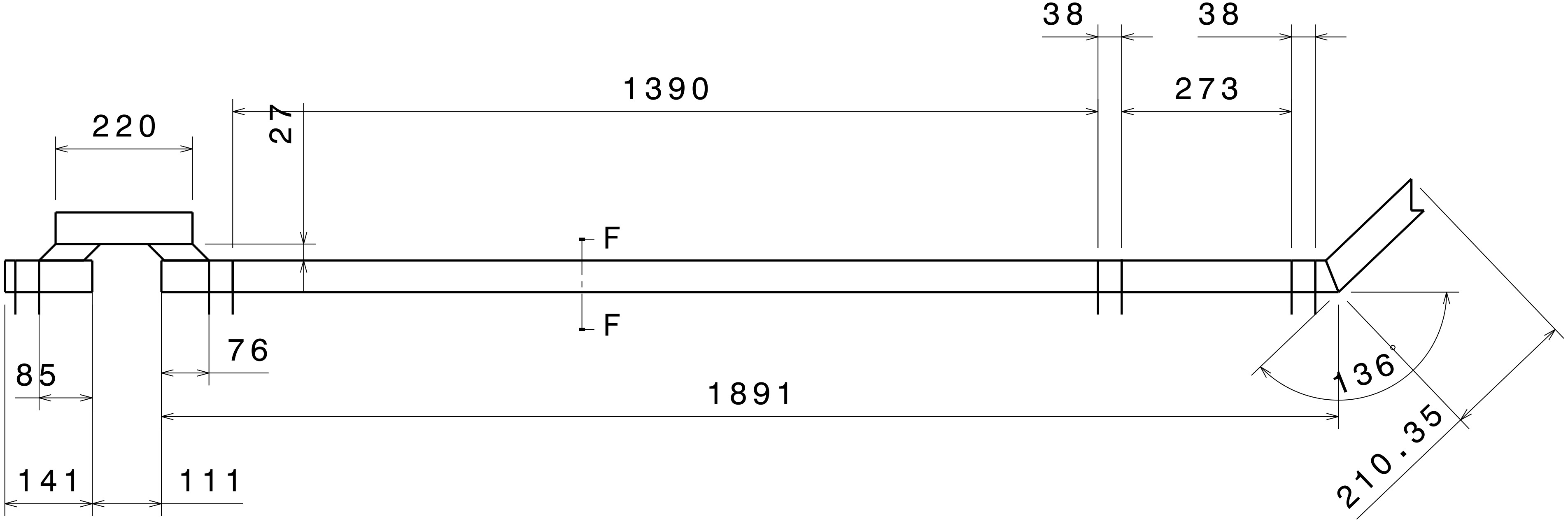

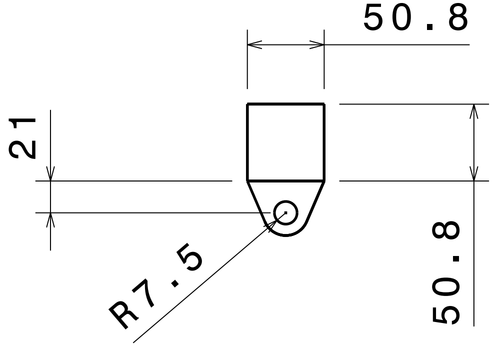

Section view F-F
Scale: 1:5

DESIGNED BY:
MRG Duarte
DATE: 3/16/2021
SUPERVISOR
M ALVES

AUS - AUTOMOVEL URBANO SEGURO

SIZE
A4

ISOMETRIC VIEW

SCALE
1:10

DRAWING NUMBER
01

SHEET
10/22

BILL OF MATERIALS			
ITEM	QUANTITY	DIAMETER	THICKNESS
1	1	2 in	0.5
2	1	2 in	0.5

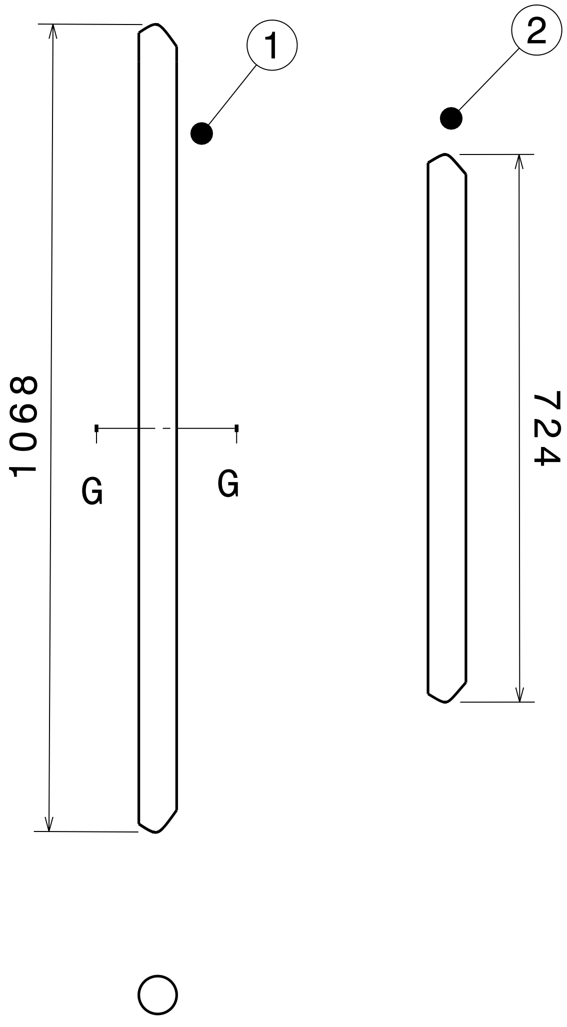

Section cut G-G
Scale: 1:10

DESIGNED BY:
MRG Duarte
DATE: 3/16/2021

SUPERVISOR
M ALVES

AUS - AUTOMOVEL URBANO SEGURO

SIZE
A4

INFERIOR BEAMS

SCALE
1:10

DRAWING NUMBER
01

SHEET
11/22

BILL OF MATERIALS	
QUANTITY	THICKNESS
1	0.8

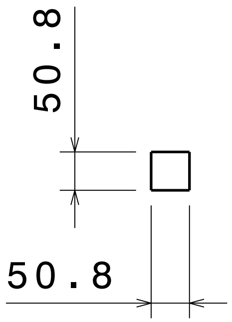

Front view
Scale: 1:10

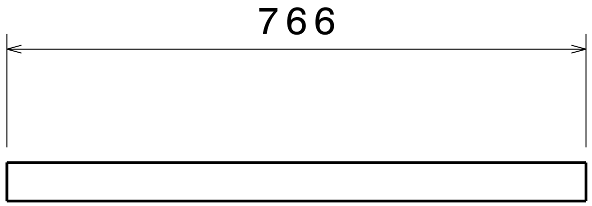

Right view
Scale: 1:10

DESIGNED BY: MRG Duarte
DATE: 3/16/2021
SUPERVISOR M ALVES

AUS - AUTOMOVEL URBANO SEGURO

SIZE A4

REAR BEAM

SCALE 1:10
DRAWING NUMBER 01
SHEET 12/22

BILL OF MATERIALS	
QUANTITY	THICKNESS
1	0.8

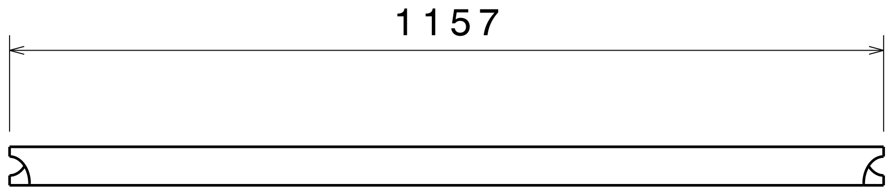

Front view
Scale: 1:10

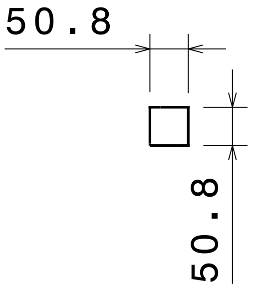

Right view
Scale: 1:10

DESIGNED BY: MRG Duarte
DATE: 3/16/2021
SUPERVISOR M ALVES

AUS - AUTOMOVEL URBANO SEGURO

BACK BEAM

SIZE A4
SCALE 1:10
DRAWING NUMBER 01
SHEET 13/22

BILL OF MATERIALS	
QUANTITY	THICKNESS
2	0.8

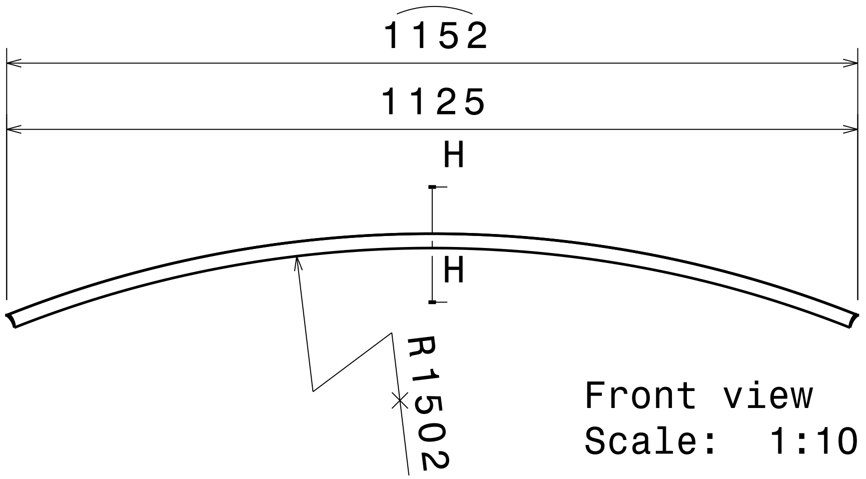

Front view
Scale: 1:10

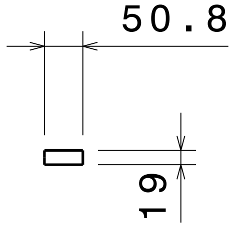

Section cut H-H
Scale: 1:10

Bottom view
Scale: 1:10

DESIGNED BY:
MRG Duarte
DATE: 3/16/2021

SUPERVISOR
M ALVES

AUS - AUTOMOVEL URBANO SEGURO

SIZE
A4

ROOF BEAM

SCALE
1:10

DRAWING NUMBER
01

SHEET
14/22

BILL OF MATERIALS	
ITEM	THICKNESS
ALL	0.5

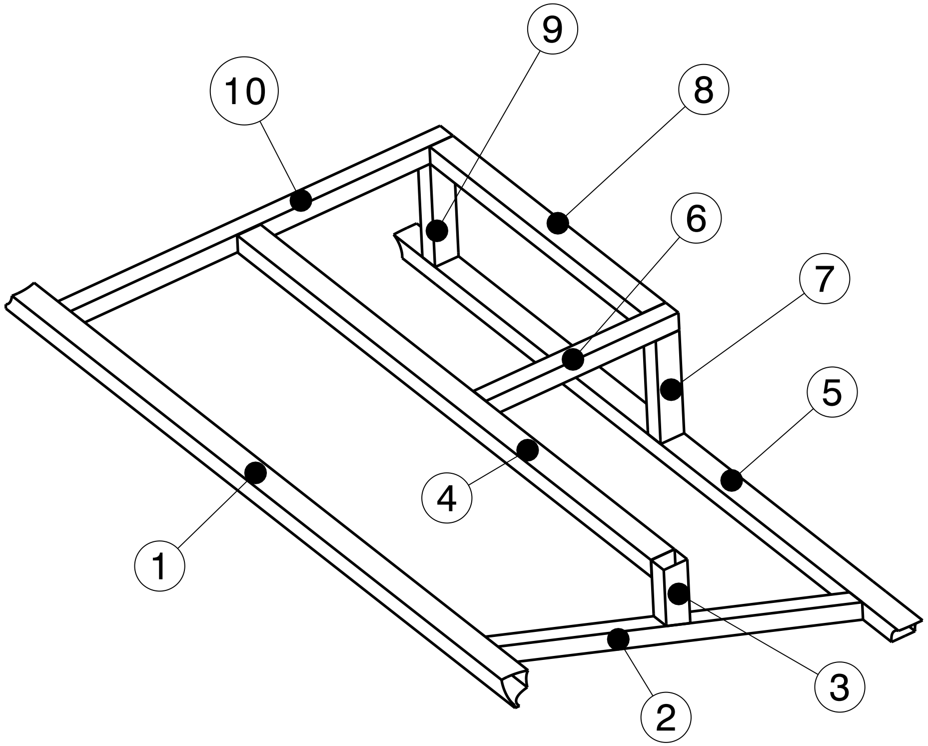

Isometric view
Scale: 1:10

DESIGNED BY:
MRG Duarte
DATE: 3/16/2021

SUPERVISOR
M ALVES

AUS - AUTOMOVEL URBANO SEGURO

FLOOR

SIZE
A4

SCALE
1:10

DRAWING NUMBER
02.Floor

SHEET
15/22

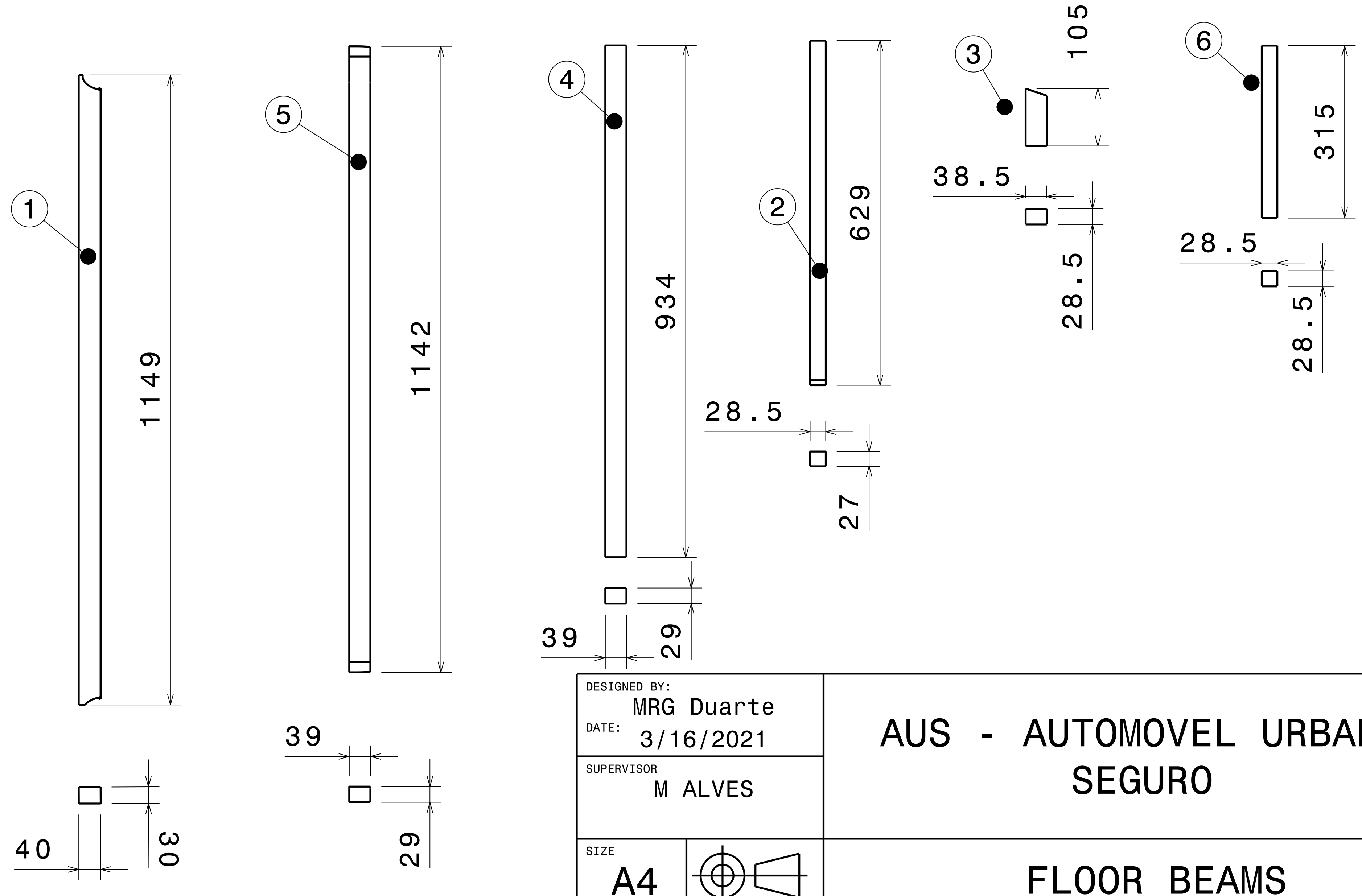

DESIGNED BY:
MRG Duarte
DATE: 3/16/2021

SUPERVISOR
M ALVES

AUS - AUTOMOVEL URBANO SEGURO

SIZE
A4

FLOOR BEAMS

SCALE
1:10

DRAWING NUMBER
01

SHEET
16/22

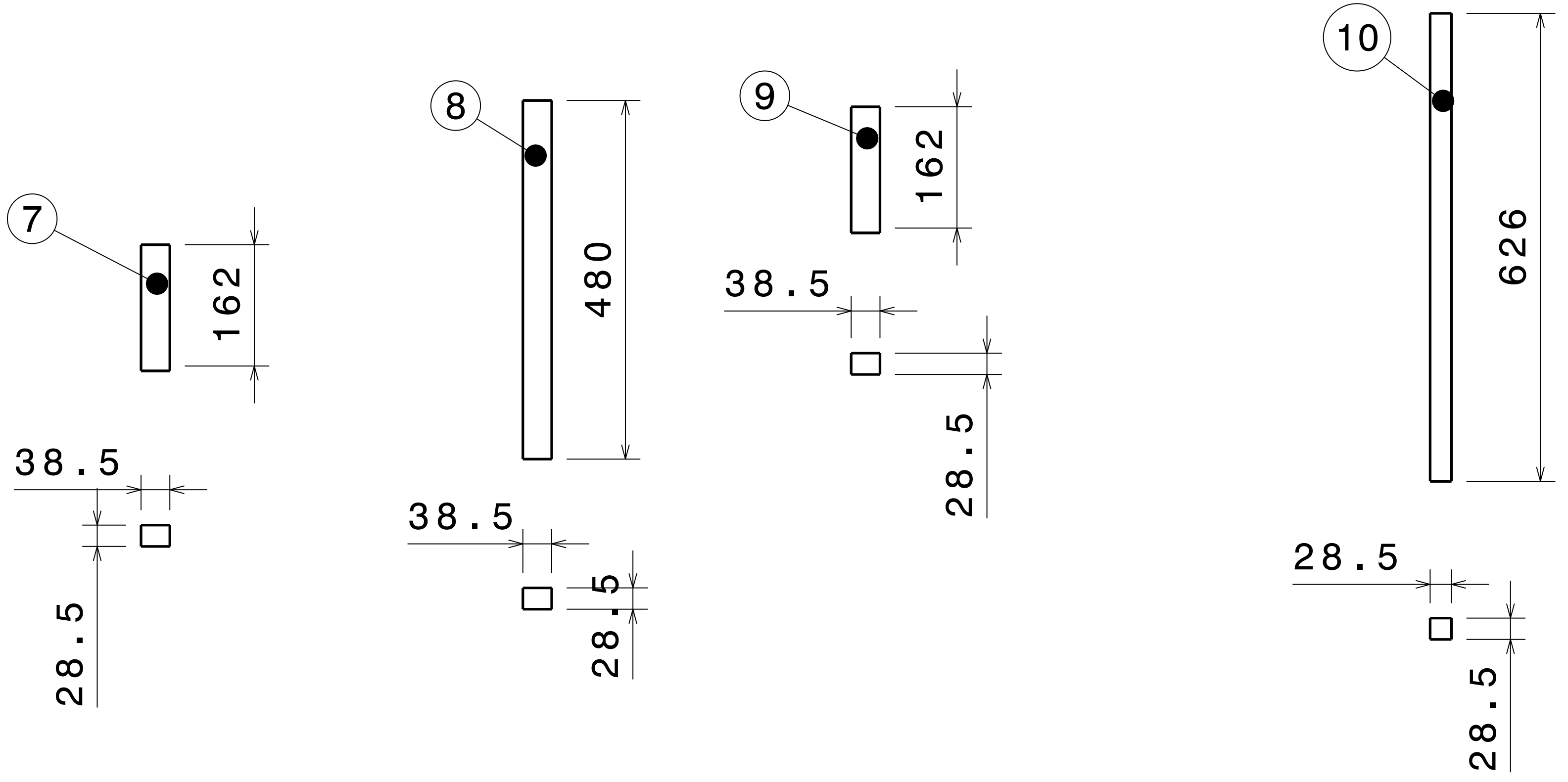

DESIGNED BY: MRG Duarte
DATE: 3/16/2021
SUPERVISOR M ALVES

AUS - AUTOMOVEL URBANO SEGURO

FLOOR BEAMS

SIZE A4
SCALE 1:10
DRAWING NUMBER 02.Floor_AllCATPart
SHEET 17/22

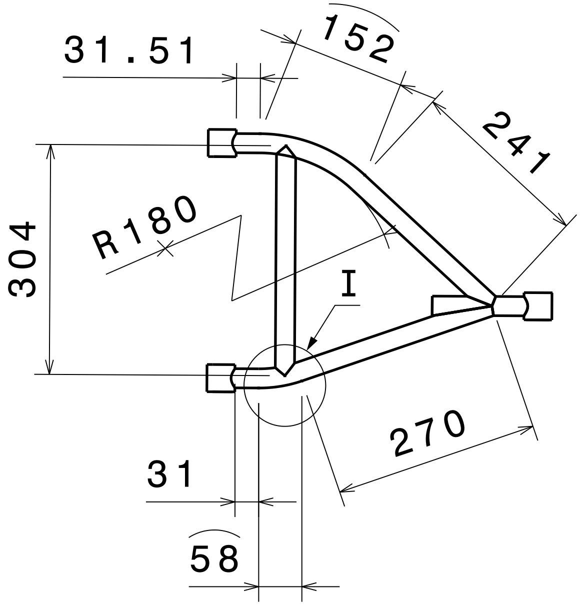

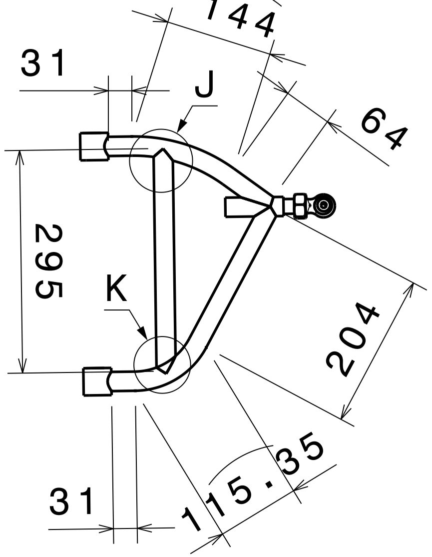

BILL OF MATERIALS			
ITEM	QUANTITY	DIAMETER	THICKNESS
1	2	1 in	1
2	2	1 in	1

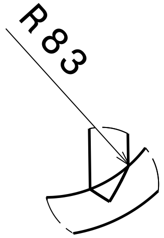

Detail K
Scale: 1:5

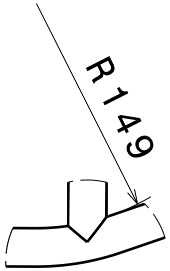

Detail I
Scale: 1:5

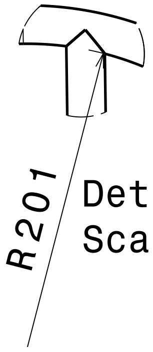

Detail J
Scale: 1:5

DESIGNED BY:
MRG Duarte
DATE: 3/16/2021
SUPERVISOR
M ALVES

AUS - AUTOMOVEL URBANO SEGURO

ISOMETRIC VIEW

SIZE
A4
SCALE
1:10
DRAWING NUMBER
01
SHEET
18/22

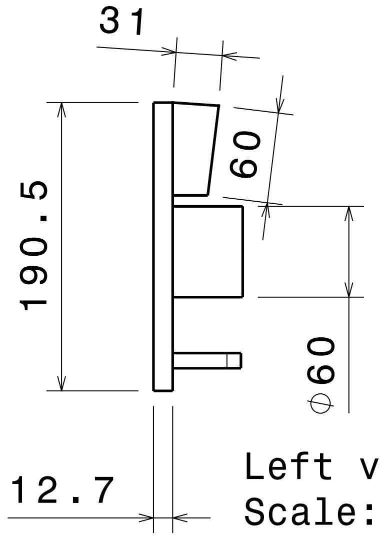

Left view
Scale: 1:5

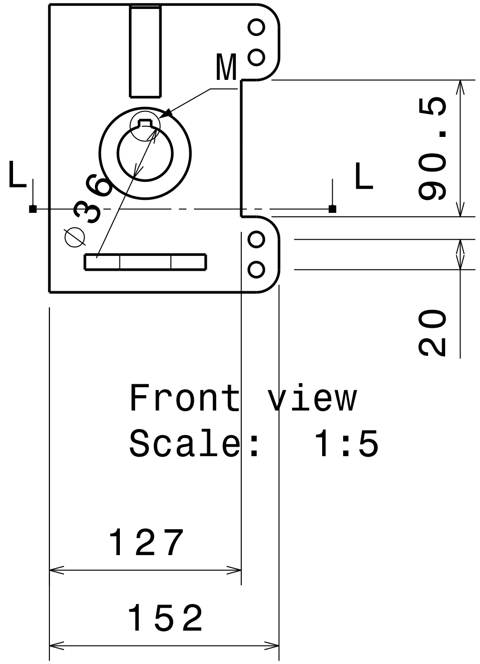

Front view
Scale: 1:5

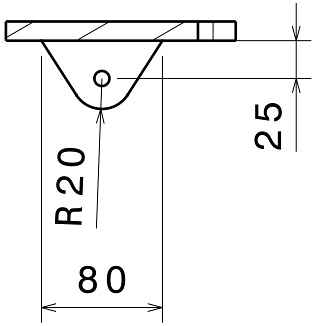

Section view L-L
Scale: 1:5

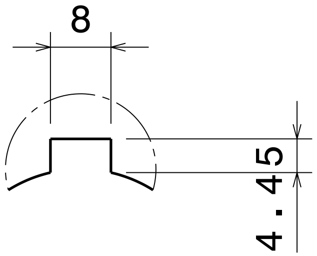

Detail M
Scale: 1:1

DESIGNED BY: MRG Duarte DATE: 3/16/2021	AUS - AUTOMOVEL URBANO SEGURO
SUPERVISOR M ALVES	
SIZE A4	STEERING KNUCKLE FRONT LEFT
SCALE 1:10	DRAWING NUMBER 01 / SHEET 19/22

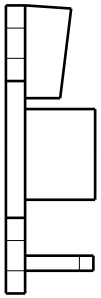

Left view
Scale: 1:5

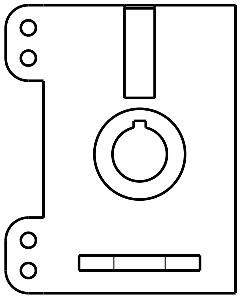

Front view
Scale: 1:5

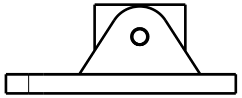

Bottom view
Scale: 1:5

DESIGNED BY:
MRG Duarte
DATE: 3/16/2021

SUPERVISOR
M ALVES

AUS - AUTOMOVEL URBANO SEGURO

SIZE
A4

STEERING KNUCKLE FRONT RIGHT

SCALE
1:10

DRAWING NUMBER
01

SHEET
20/22

BILL OF MATERIALS		
ITEM	QUANTITY	THICKNESS
1	1	0.5
2	1	1.0

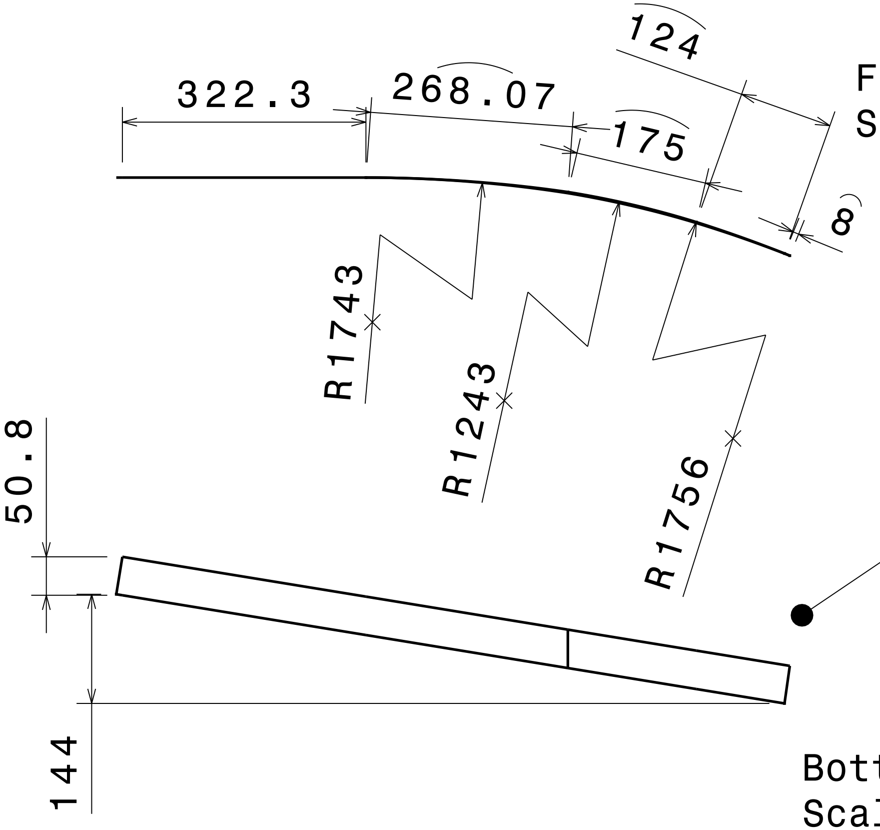

Front view
Scale: 1:10

Bottom view
Scale: 1:10

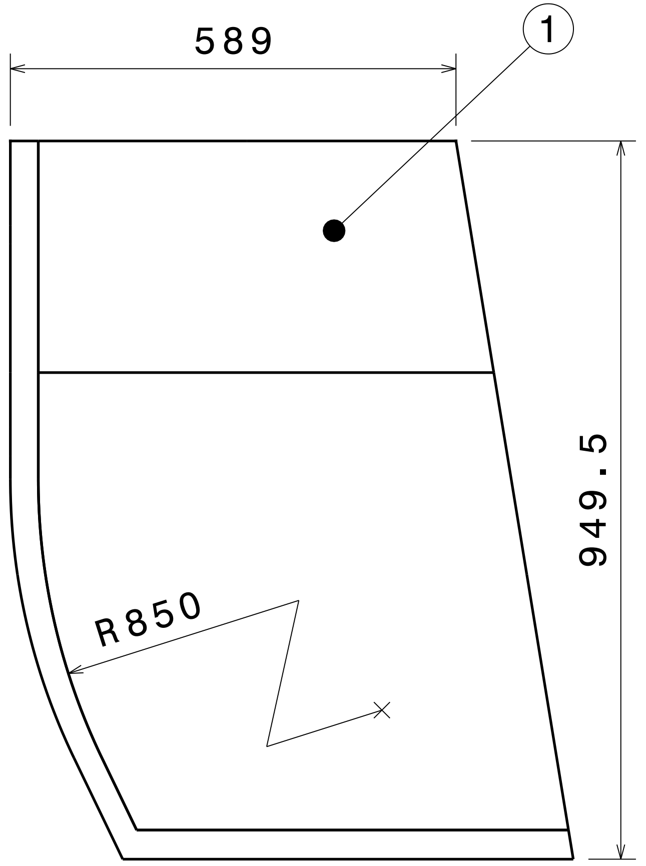

Front view
Scale: 1:10

DESIGNED BY:
MRG Duarte
DATE: 3/16/2021
SUPERVISOR
M ALVES

AUS - AUTOMOVEL URBANO
SEGURO

SIZE
A4

DOOR AND REINFORCEMENT

SCALE
1:10

DRAWING NUMBER
01

SHEET
21/22

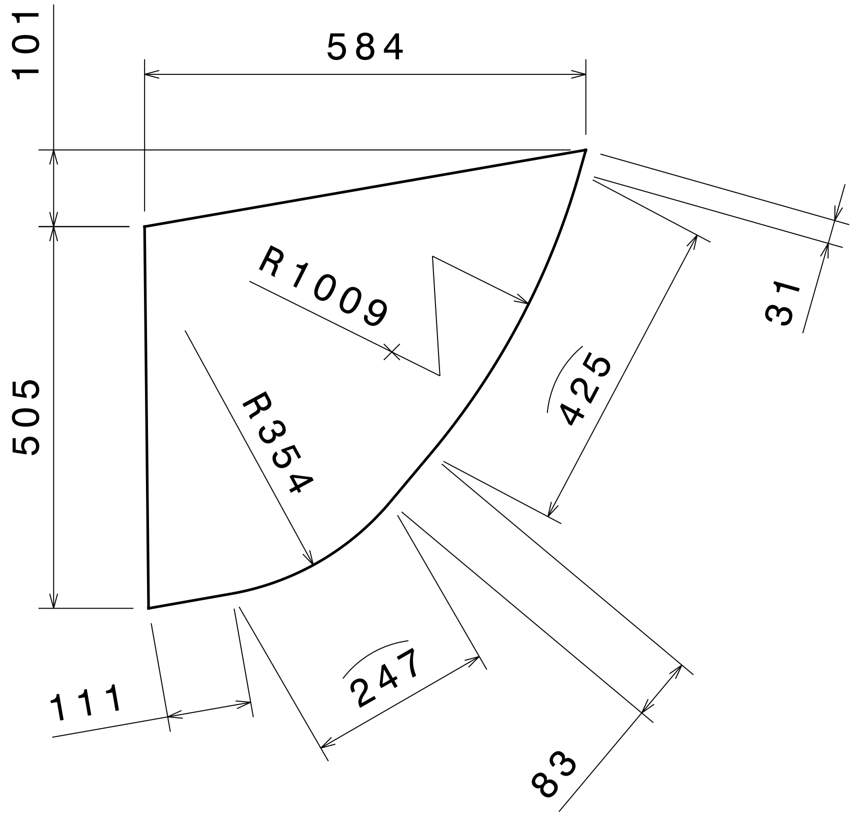

DESIGNED BY:
MRG Duarte
DATE: 3/16/2021

SUPERVISOR
M ALVES

AUS - AUTOMOVEL URBANO SEGURO

SIZE
A4

REAR DOOR

SCALE
1:10

DRAWING NUMBER
Portinhola1

SHEET
22/22